

NATIONAL TECHNICAL UNIVERSITY OF ATHENS SCHOOL OF ELECTRICAL AND COMPUTER ENGINEERING SCHOOL OF MECHANICAL ENGINEERING

INTERDISCIPLINARY POSTGRADUATE PROGRAMME "Translational Engineering in Health and Medicine"

Comparative CFD Study of Bubble Trap Inlet Geometry for Ex-Vivo Heart Perfusion Systems

Postgraduate Diploma Thesis

Manou Nikoletta

Supervisor: Professor Spitas Vasilios, National Technical University of Athens



NATIONAL TECHNICAL UNIVERSITY OF ATHENS SCHOOL OF ELECTRICAL AND COMPUTER ENGINEERING SCHOOL OF MECHANICAL ENGINEERING

INTERDISCIPLINARY POSTGRADUATE PROGRAMME "Translational Engineering in Health and Medicine"

Comparative CFD Study of Bubble Trap Inlet Geometry for Ex-Vivo Heart Perfusion Systems

Postgraduate Diploma Thesis Manou Nikoletta

Supervisor: Professor Spitas Vasilios, National Technical University of Athens

The postgraduate diploma thesis has been approved by the examination committee on 23 October 2025

1st member	2nd member	3rd member
Anganostakis Marios	Mananaulas Christas	Spitas Vasilios
Anagnostakis Marios	Manopoulos Christos	Spitas Vasilios
Professor	Associate Professor	Professor
National Technical	National Technical	National Technical
University of Athens	University of Athens	University of Athens

Athens, October 2025

Manou Nikoletta

Graduate of the Interdisciplinary Postgraduate Programme, "Translational Engineering in Health and Medicine", Master of Science, School of Electrical and Computer Engineering, National Technical University of Athens

Copyright © - Manou Nikoletta 2025 All rights reserved.

You may not copy, reproduce, distribute, publish, display, modify, create derivative works, transmit, or in any way exploit this thesis or part of it for commercial purposes. You may reproduce, store or distribute this thesis for non-profit educational or research purposes, provided that the source is cited, and the present copyright notice is retained. Inquiries for commercial use should be addressed to the original author.

The ideas and conclusions presented in this paper are the author's and do not necessarily reflect the official views of the National Technical University of Athens.

Abstract

This study focuses on the computational fluid dynamics (CFD) analysis and optimization of inlet geometry of a bubble trap designed for ex-vivo heart perfusion systems. The main objective was to examine how variations in inlet height and angulation affect bubble trapping efficiency and flow characteristics within the chamber. For that reason, different device configurations were designed in SolidWorks and analyzed using CFD simulations in ANSYS Fluent, employing an Eulerian–Lagrangian framework, where the continuous perfusate phase was modeled with the Navier–Stokes equations and the dispersed air bubbles were tracked using the Discrete Phase Model (DPM) under two-way coupling to account for phase interaction.

A total injection of 1,500 spherical air bubbles consisting of six size groups of 250 bubbles within a size range of 50– $500\mu m$, was introduced at the inlet of the bubble trap to represent entrained air entering the system and six geometrical configurations were tested by varying the inlet height and angulation, while maintaining constant chamber volume and flow conditions. Contours of pressure, temperature, and turbulent kinetic energy, together with inlet and outlet data on pressure, velocity, and temperature, as well as velocity streamlines, were examined to characterize the hydrodynamic behavior within the chamber. The results demonstrated that inlet configuration had an influence on flow circulation and bubble trapping efficiency, as it was observed that the higher inlet position enhanced recirculation and delayed bubble escape, while inlet angulation redirected the flow toward the chamber walls, further improving bubble entrapment and reducing the likelihood of direct bubble transport to the outlet.

Among all tested geometries, the 45° angled high inlet configuration achieved the highest bubble trapping efficiency, while the low inlet configuration without angulation exhibited the lowest efficiency. Furthermore, in all simulations it was showed that bubble size significantly affected escape behavior, as smaller bubbles (50–100 μ m) were more likely to escape across all geometries, while larger bubbles (\geq 400 μ m) were effectively trapped. Additionally, pressure and temperature analyses showed small variations across all cases, with a pressure drop ranging between 1.25 and 1.28mmHg and temperature loss of approximately 0.007–0.009 °C, across the different geometries.

Keywords: Perfusion Systems, Bubble Trap, Inlet Geometry, CFD, DPM, Langendorff Heart Perfusion Systems, T3

Acknowledgements

The completion of a master's thesis is a creative journey that requires both time and dedication. As I reach the end of my studies and complete this final chapter, I would like to express my heartfelt gratitude to those who have been a source of help, strength, and support throughout this process.

First and foremost, I would like to sincerely thank my supervisor, Professor Vasileios Spitas, for the trust he placed in me throughout this work. His guidance and mentorship, combined with his kind and encouraging presence, greatly contributed to an excellent collaboration. I would also like to express my deep appreciation to PhD candidate Vasilis Gakos for his selfless assistance, invaluable contribution and his willingness to share his knowledge, which were essential to the successful completion of this endeavor.

Finally, I owe my deepest thanks to my parents for their unwavering love and support throughout these years, as well as to my sisters, who have been a constant source of strength, motivation, and joy in every step of my journey. A special thank you goes to Giorgos, and to my friends and fellow students, who have accompanied and supported me through all these years.

Table of Contents

TABLE OF C	CONTENTS	9
ACRONYM:	S	12
TABLE OF F	FIGURES	13
TABLE OF T	ABLES	15
1 Introduction	on	17
1.1 Backg	round	17
1.2 Bubbl	es in perfusion systems.	18
1.3 Object	tives	18
2 Literature	Review	20
	ed Perfused Heart	
2.2 Mamn	nalian heart-lung preparation	21
	ndorff Perfusion System	
2.3.1	· · · · · · · · · · · · · · · · · · ·	
2.3.2		
2.3.3	The importance of Langendorff's Model	
2.4 Bubbl	e Formation and Trapping Mechanism in Heart Perfusion Systems	
	utational Fluid Dynamics (CFD) in Biomedical Engineering	
	of T3 Hormone in Cardiac Function	
2.7 Organ	Care Systems Heart, OCS Systems	28
_		
	ıl Background	
	an vs. Lagrangian frameworks in CFD.	
	Dynamics of Bubbles in liquid	
3.2.1	The Navier–Stokes and Continuity Equations	
3.2.2	Motion of Bubbles in Liquids	
-	utational Modeling	
3.3.1	Discrete Phase Model (DPM)	
3.3.2		
3.3.3	Turbulence Interactions with Particles	
3.4 Bubbl	e Trap Efficiency	39
4 Methodolo	ogy	40
	ptual design	
4.1.1	Design of the Bubble Trap	
4.1.2	Technical Specifications	
4.2 Simula	ation Setup in ANSYS CFD	
4.2.1	Meshing	
4.2.2	General Settings	
4.3 Discre	ete Phase Model Setup	
4.3.1	General DPM Set up	
4.3.2	Injections	51
4.4 Bound	lary Conditions	54
4.4.1	Inlet	54
4.4.2	Outlet	55
443	Walls	55

4.5 Simulat	ion Procedure	55
5 Results and	Discussion	58
	cy	
5.1.1		
5.1.2	Inlet Height Variation	
_	Inlet Angle Variation	
5.1.3	Bubbles escaping over time	
	2	
	<i>T</i>	
5.4 Temper	ature	75
5.5 Turbule	nce Kinetic Energy	80
6 Conclusion		82
	ion	
	nendations for Future Research	
-		-
7 References		85
7 References	•••••••••••••••••••••••••••••••••••••••	
8 Appendix		92
	ix A: Escaped Bubbles per Size through time	
	ix B: Plots of Pressure Area-Weighted Average	
	ix C: Plots of Pressure Drop	
	ix D: Velocity Magnitude Area-weighted Average Plots	
	ix E: Bubble Size vs Number of Escaped Bubbles over Time	
8.3 Append	ix E. Duodie Size vs Number of Escaped Buddles over Time	9/

Acronyms

CFD	Computational Fluid Dynamics
CPB	Cardiopulmonary Bypass
DPM	Discrete Phase Model
ECMO	Extracorporeal Membrane Oxygenation
OCS	Organ Care System
RA	Right Atrium
SP	Systolic Pressure
<i>T3</i>	L-triiodothyronine
TKE	Turbulence Kinetic Energy

Table of Figures

Figure 2.1 The isolated perfused frog heart produced by E. Cyon. [11]	21
Figure 2.2: H.N. Martin Mammalian heart-lung experimental setup[15]	22
Figure 2.3: Langenlorff's Isolataed mamalian heart system[1]	
Figure 2.4 Depiction of the Langendorff System. The water jacket holds the perfusate fluid, which is	
heated by the thermocirculator and oxygenated via the oxygenator bubbler. The perfusate is propelled	
by a peristaltic pump, subsequently traversing a filter to the bubble trap, where it is coupled to a	
thermocirculator to ensure a consistent temperature, before perfusing the heart through the aortic	
cannula [18]	27
Figure 2.5: Schematic Representation of Organ Care Systems (OCS TM) by TranMedics [46]	28
Figure 3.1 Comparison of Eulerian, Lagrangian, and Combined Frameworks for Particle–Fluid	
Interactions [53]	30
Figure 3.2 Balancing forces on a bubble [59]	36
Figure 3.3 Turbulent flows eddy particle interaction [51]	
Figure 4.1 SolidWorkds 3D Model of the r30.0×53.0 geometry	
Figure 4.2 Geometrical Design of the Bubble Trap r30.0×53.0 Configuration	
Figure 4.3 SolidWorks design of the geometry (a)-(b) r30.0x53.0 inlet13.25 (c)-(d)	
r30.0x53.0 inlet39.75	43
Figure 4.4 Geometrical Design of the Bubble Trap with inlet angulation (a)	
r30.0x53.0_inlet39.75_15deg, (b) r30.0x53.0_inlet39.75_30deg, (c) r30.0x53.0_inlet39.75_45deg	44
Figure 4.5 3D Model of the Bubble Trap of the Geometry r30.0×53.0	
Figure 4.6 Generated Mesh of the Bubble Trap Geometry (r30.0×53.0)	
Figure 4.7 Inflation Layers Applied Near the Wall of Mesh.	
Figure 4.8: Boundary named selections: A) outlet bubbles, B) outlet perfusate, and C) inlet	
Figure 4.9 Group of bubbles injections at the inlet within a stagger radius of 1mm (front view)	
Figure 4.10 Group of bubbles injections at the inlet within a stagger radius of 1mm (right view)	
Figure 4.11 Boundary Conditions Setup. The blue arrows represent the inlet, where the perfusate ent	
the chamber, and the red arrows indicate the outlet, where the flow exits the system	55
Figure 5.1 Number of Escaped Bubbles by Bubble Size	59
Figure 5.2 Inlet Height vs. Bubble Trapping Efficiency	60
Figure 5.3 Spatial Distribution of Bubbles with Different Size in the Geometries of Different Inlet	
Height (a) $r30.0x53.0$ (b) $r30.0x53.0$ inlet13.25 (c) $r30.0x53.0$ inlet39.75, after the 4s simulation	61
Figure 5.4 Inlet Angulations vs. Bubble Trapping Efficiency	62
Figure 5.5 Spatial Distribution of Bubbles with Different Size in the Geometries of Different Inlet	
Angulation (a) r30.0x53.0_inlet39.75_15deg (b) r30.0x53.0_inlet39.75_30deg (c)	
r30.0x53.0_inlet39.75_45deg , after the 4s simulation	63
Figure 5.6 Plots of Escaped Bubbles over Time (a) r30.0x53.0 (b) r30.0x53.0_inlet13.25 (c)	
r30.0x53.0_inlet39.75 (d) r30.0x53.0_inlet39.75_15deg (e) r30.0x53.0_inlet39.75_30deg (f)	
r30.0x53.0_inlet39.75_45deg	
Figure 5.7 Time Evolution of Bubble Escape for the Different Inlet Configurations.	
Figure 5.8 Number of Escaped Bubbles over time across the different geometries	
Figure 5.9 Static Pressure distribution of the inlet across geometries	
Figure 5.10 Bar plot of Mean Pressure Drop across geometries	67
Figure 5.11 Contours of Static Pressure of the different configurations (a) r30.0x53.0 (b)	
r30.0x53.0_inlet13.25 (c) r30.0x53.0_inlet39.75 (d)-(e) r30.0x53.0_inlet39.75_15deg , (f)-(g)	
r30.0x53.0_inlet39.75_30deg , (h)-(i) r30.0x53.0_inlet39.75_45deg	
Figure 5.12 Cross Sectional Contours of Static Pressure (top view) on the inlet plane of the different	<u>.</u>
configurations (a) r30.0x53.0 (b) r30.0x53.0_inlet13.25 (c) r30.0x53.0_inlet39.75 (d)	
r30.0x53.0_inlet39.75_15deg (e) r30.0x53.0_inlet39.75_30deg (f) r30.0x53.0_inlet39.75_45deg	
Figure 5.13 Velocity magnitude streamline plots for the different geometries (a)-(b) $r30.0x53.0$, (c)-	<i>(d)</i>
r30.0x53.0_inlet13.25 (e)-(f) r30.0x53.0_inlet39.75, (g)-(h) r30.0x53.0_inlet39.75_15deg, (i)-(j)	
r30.0x53.0_inlet39.75_30deg, (k)-(l) r30.0x53.0_inlet39.75_45deg	74
Figure 5.14 Bubbles distribution across the velocity streamlines of the geometry	
r30.0x53.0_inlet39.75_45deg	
Figure 5.15 Outlet Temperature Distribution for all geometries	76

Figure 5.16 Plots of Average Weighted Temperature vs Time (a) r30.0x53.0 (b) r30.0x53.0_inlet13.25
(c) r30.0x53.0_inlet39.75 (d) r30.0x53.0_inlet39.75_15deg (e) r30.0x53.0_inlet39.75_30deg (f)
r30.0x53.0_inlet39.75_45deg77
Figure 5.17 Contours of Temperature (a) r30.0x53.0 (b) r30.0x53.0 inlet13.25 (c)
r30.0x53.0_inlet39.75 (d)-(e) r30.0x53.0_inlet39.75_15deg, (f)-(g) r30.0x53.0_inlet39.75_30deg, (h)-
(i) r30.0x53.0_inlet39.75_45deg79
Figure 5.18 Volume Rendering Contours of Turbulence Kinetic Energy (a) r30.0x53.0 (b)
r30.0x53.0 inlet13.25 (c) r30.0x53.0 inlet39.75 (d) r30.0x53.0 inlet39.75 15deg (e)
r30.0x53.0 inlet39.75 30deg (f) r30.0x53.0 inlet39.75 45deg81
Figure 8.1 Plots of Pressure Area-weighted Average (a) r30.0x53.0 (b) r30.0x53.0 inlet13.25 (c)
r30.0x53.0_inlet39.75 (d) r30.0x53.0_inlet39.75_15deg (e) r30.0x53.0_inlet39.75_30deg (f)
r30.0x53.0_inlet39.75_45deg94
Figure 8.2 Plots of Pressure Drop Across Different Geometries (a) r30.0x53.0 (b)
r30.0x53.0 inlet13.25 (c) r30.0x53.0 inlet39.75 (d) r30.0x53.0 inlet39.75 15deg (e)
r30.0x53.0 inlet39.75 30deg (f) r30.0x53.0 inlet39.75 45deg95
Figure 8.3 Velocity Magnitude Area-Weighted Average Plots (a) r30.0x53.0 (b) r30.0x53.0 inlet13.25
(c) r30.0x53.0 inlet39.75 (d) r30.0x53.0 inlet39.75 15deg (e) r30.0x53.0 inlet39.75 30deg (f)
r30.0x53.0 inlet39.75 45deg96
Figure 8.4 Correlation of Bubble' Size with the Number of Escaped Bubbles over Time (a) r30.0x53.0
(b) r30.0x53.0 inlet13.25 (c) r30.0x53.0 inlet39.75 (d) r30.0x53.0 inlet39.75 15deg (e)
r30.0x53.0_inlet39.75_30deg (f) r30.0x53.0_inlet39.75_45deg97

Table of Tables

Table 4:1 Geometrical Parameters of the Bubble Trap	44
Table 4:2 Design Specifications of the Bubble Trap	
Table 4:3 Perfusate Properties at 37°C	46
Table 4:4 Calculated Y ⁺ Values for the Bubble Trap Geometries	49
Table 4:5 Summary of Mesh Quality Parameters and Element Statistics for each Geometry	49
Table 4:6 Injected Bubble Characteristics for the Discrete Phase Model (DPM) Simulation	53
Table 4:7 Total Injected Bubble Mass and Volume in the DPM Simulation	53
Table 4:8 Summary of Solver Coupling and Discretization Schemes	56
Table 4:9 CFD Model Settings	
Table 4:10 Mass Flow Rate Flux Difference Between Inlet and Outlet for Each Geometry	57
Table 5:1 Summary of Injected and Escaped Air Mass, Bubble Count, and Bubble Trapping Efficie	ency
for Each Bubble Trap Geometry	58
Table 5:2 Escaped Bubbles by Bubble's Diameter and Corresponding Bubble Trapping Efficiency	for
Inlet Height and Angulation	59
Table 5:3 Number of Escaped Bubbles over time for all geometries, along with the corresponding	
Bubble Trapping Efficiency.	64
Table 5:4 Mean Inlet Static Pressure and Pressure Drop in the different geometries	
Table 5:5 Mean values of outlet Temperatureare for all geometries	
Table 8:1 Number of Escaped Bubbles by Size and Time for the Geometry r30.0x53.0	92
Table 8:2 Number of Escaped Bubbles by Size and Time for the Geometry r30.0x53.0_inlet13.25	92
Table 8:3 Number of Escaped Bubbles by Size and Time for the Geometry r30.0x53.0_inlet39.75	92
Table 8:4 Number of Escaped Bubbles by Size and Time for the Geometry	
r30.0x53.0_inlet39.75_15deg	92
Table 8:5 Number of Escaped Bubbles by Size and Time for the Geometry	
r30.0x53.0_inlet39.75_30deg	93
Table 8:6 Number of Escaped Bubbles by Size and Time for the Geometry	
r30.0x53.0_inlet39.75_45deg	93

$m{1}$ Introduction

1.1 Background

Ex vivo heart perfusion systems constitute critical tools in both experimental cardiology and clinical transplantation as they allow the heart to be maintained and studied outside the body, by perfusing it with a nutrient-rich, oxygenated solution. One of the most well-established models is the Langendorff system, developed in 1895 by Oscar Langendorff, which enables the isolated perfusion of the heart through retrograde flow via the aorta. [1]. The Langendorff model has been widely used in physiological and pharmacological research due to its ability to preserve coronary circulation and contractile function without requiring neural or hormonal input.

Over the years, the need for heart preservation has led to the revolution of heart perfusion systems. [2]. The fundamental principles of ex vivo perfusion have been adapted for clinical applications, particularly in organ transplantation, such as the Organ Care System (OCS), that now support normothermic, beating-heart perfusion during transport [3]. The need for the extended preservation time, reduction of ischemic injury and the improvement of post-transplant outcomes have been met on these devices. Heart transplantation remains the optimal treatment for specific individuals with severe heart failure, notwithstanding the progress made in medical treatment. Nevertheless, as the frequency of heart failure continues to rise globally, the disparity between the number of available donor hearts and the number of patients awaiting a transplant is growing [4].

One of the key challenges in heart perfusion systems remains the presence of air bubbles in the perfusate, which can cause different incidents such as air embolism, block coronary vessels, and lead to myocardial damage. For that reason, heart perfusion systems have bubble traps that are integrated into perfusion circuits to remove entrained air before it reaches the heart. Even though commercial systems incorporate such components, there is limited literature analyzing their efficiency using computational methods, especially in the context of human heart perfusion systems.

Computational Fluid Dynamics (CFD) is a powerful tool in order to investigate flow patterns, bubble trajectories, and the trapping efficiency of devices such as bubbles traps and combined with the Discrete Phase Model (DPM), can be a robust framework for simulating multiphase flow behavior and investigating bubble dynamics in biomedical devices. In this thesis, DPM is used to simulate and track air bubbles within a perfusate flow and to analyze how inlet configuration parameters specifically the distance between the inlet and the outlet, as well as the inlet angle influence bubble trapping efficiency in a conceptual bubble trap designed for a Langendorff-based heart perfusion system. To ensure physiological relevance, key boundary conditions such as flow rate, pressure, and temperature were selected based on specifications from commercial ex vivo perfusion systems, particularly the Organ Care System (OCS) developed by TransMedics. Although the model is not intended to replicate the OCS geometry, the use of clinically relevant parameters ensures that the simulation results remain applicable to biomedical applications.

1.2 Bubbles in perfusion systems

The presence of air bubbles in heart perfusion systems presents a critical risk that can affect the myocardial viability and the reliability of experimental outcomes. When air bubbles enter the circuit, if their size is sufficiently small to avoid directly obstructing an artery, it will be carried by the perfusate and adhere to the standard circulatory pathway.

One of the primary consequences is the vascular obstruction, where air bubbles can block the capillaries and arterioles, leading to impaired myocardial perfusion and local ischemia [5], meaning that air bubbles could be lethal to the heart or adversely impact its function [6]. Even small bubbles can disrupt coronary circulation, creating areas of hypoxia and metabolic imbalance that directly can affect the physiological stability of the heart [7]. Embolization in the coronary arteries results also in electrocardiographic alterations which include dysrhythmias, cardiac failure, myocardial suppression and cardiac arrest [8].

Beyond obstruction, air bubbles can also cause mechanical and biochemical injury to the endothelium, as when they are travelling through the vasculature, they exert shear stress and can collapse or fragment under flow conditions, damaging endothelial surfaces [7]. From that disruption, inflammatory cascades can be activated, including complement activation and leukocyte adhesion, that further exacerbating vascular injury [7]. Furthermore, air bubbles can also contribute to thrombus formation within the perfusion system and coronary vasculature [9], which not only further obstruct coronary perfusion but may also embolize downstream, compounding ischemic damage in myocardial tissue.

Lastly, air bubbles interference with hemodynamic monitoring, leading to artifacts which reduce the accuracy of key measurements, such as coronary perfusion pressure or left ventricular pressure, and therefore undermine the reliability of the data. This can be explained from the fact that air bubbles compress and expand differently from liquid perfusate, which can distort pressure waveforms and generate spurious readings from pressure transducers and flow sensors [10].

1.3 Objectives

The main objective of this study is to investigate how variations in inlet configuration, specifically inlet height and angulation affect the introduction, movement, and escape of air bubbles in a bubble trap designed for ex-vivo heart perfusion systems. Since the presence of air bubbles can impair perfusion safety, understanding how the inlet geometric and flow parameters influence bubble-trapping efficiency is essential for improving device performance. The geometry of the bubble trap was designed in SolidWorks®, and simulations were performed in ANSYS Fluent using an Eulerian—Lagrangian framework, the Discrete Phase Model (DPM), to describe the interaction between the continuous perfusate and the dispersed air bubbles.

To achieve this aim, the specific objectives of the study are:

- Examine how inlet height and inlet angulation influence bubble trapping efficiency, by analyzing six geometrical configurations with constant internal volume and under the same flow conditions.
- To investigate how bubble size (50–500μm) affects escape behavior, identifying which bubbles are more likely to remain trapped or escape through the outlet.
- To analyze velocity streamlines to observe how the inlet configuration affects the flow direction, circulation zones, and bubble transport pathways.
- To evaluate contours of pressure, temperature, and turbulent kinetic energy to identify areas of high and low pressure, as well as cooler or warmer regions within the chamber and to locate zones of high/low turbulence kinetic energy.
- To determine in which geometries bubbles escaped faster and relate this behavior to inlet design and flow structure.
- To assess the hydrodynamic and thermal performance of the system, such as pressure drop and temperature loss.

The findings of this study are intended to guide the future development and experimental validation of the bubble trap prototype in lab environment, which will ultimately operate with a perfusate containing triiodothyronine (T3) to simulate physiological conditions in cardiac perfusion systems.

2 Literature Review

The evolution of heart perfusion systems has played a significant role in both experimental cardiology and clinical transplantation. From the early isolated heart preparations of Ludwig, Cyon, and Martin, to the development of the Langendorff model and modern portable systems like the Organ Care System (OCS), significant advances have been made in maintaining the viability and functionality of the heart ex vivo.

2.1 Isolated Perfused Heart

Carl Ludwig and Elias Cyon in 1866 created the first isolated perfused model for frog heart preparation [11]. The concept of investigating the functioning of the isolated perfused heart was conceived and implemented as early as 1846, as documented in a brief report by Wald, a Carl Ludwig student in Marburg. Ludwig created the kymograph, the first recorder to track physiological processes over time, in that same year [11]. In order to create an isolated heart preparation, Wild and Ludwig joined the carotid artery of a live donor animal to the aorta of a dead animal, preserving the recipient animal's coronary arteries' perfusion [12]. This was a heart preparation from an animal with a beating heart, but not ejecting. Prolonged and continuous thumping might be sustained if the process of blood coagulation was inhibited. This cardiac preparation could likewise be activated, and various segments of it could be removed without causing any detriment to the general function of the heart. The sole issue was the impossibility of halting cardiac pulsation and then reviving cardiac activity [12].

Subsequently, the following procedure involved surgically removing a heart and maintaining it in a state of total isolation for an extended duration. The frog is considered a suitable animal because of its heart's spongy shape that lacks coronary arteries, and the exchange of breathing gases and metabolites happens exclusively through diffusion mechanisms. Elias Cyon, while working at Carl Ludwig's Leipzig Physiological Institute, pioneered the technique of the heart preparation[6], [11], [13].

The initial contribution centered on the experiment using the heart in isolation. A frog's heart was surgically removed, and the aorta and vena cava were inserted with cannulas and filled with serum derived from rabbit blood [14]. The blood was pumped from the aorta through the glass tube to the vena cava (see Figure 2.1). Pressure measurement involved the manipulation of a stopcock at (I) (see Figure 2.1), through which a rubber tube (f) was introduced. This tube was then connected to a mercury manometer on the right.

The serum's temperature in the system can be determined by using a thermometer put into the oblique glass tube. The circulatory system was encased in a glass cylinder filled with fluid, which could be calibrated to any preferred temperature. Only three data were documented from the isolated perfused frog heart: heart rate, circulatory pressure, and the temperature of the circulating serum [13]. Through this experimental design, it was shown that a specific quantity of serum is necessary to fill the heart in order to generate

diastolic filling pressure, enabling the ventricle to expel fluid. In addition, the heart rate rose as the temperature increases, eventually reaching a unique maximum value for each individual heart. Once the temperature surpassed its upper limit, the heart rate saw a rapid and significant decrease [11].

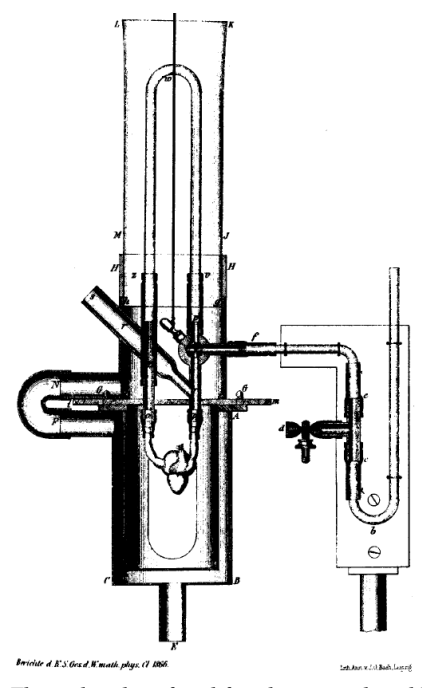


Figure 2.1 The isolated perfused frog heart produced by E. Cyon. [11]

It was additionally determined that each individual heart has a specific optimum temperature for maximal pumping efficiency. Several set ups at Carl Ludwig's Leipzig Physiological Institute modified the isolated frog heart preparation. From these experiments several discoveries were found like the treppe phenomenon by Henry Pickering Bowditch.

Despite their usefulness, frog hearts have limitations, such as differences in physiology compared to mammalian hearts, which made it challenging to directly extrapolate findings to humans. The heart comprises three chambers (two atria and one ventricle) and lacks a coronary vascular system; consequently, the exchange of metabolites and gases between blood and cardiac muscle tissue occurs via diffusion [13]. In continuous, N.Martin, Carl Ludwig, Oscar Langendorff, and Ernest Henry Starling utilized rabbit, dog and cat hearts.

2.2 Mammalian heart-lung preparation

H.N.Martin focused his experimental endeavors on the advancement of the first isolated perfused mammalian heart in 1880. Anesthetized and curarized cats or dogs underwent artificial ventilation while systemic circulation was excluded, except for a cannula in the left subclavian artery attached to a manometer. All blood expelled by the left ventricle was sent to the coronary arteries. The coronary circulation drained into the right atrium, traversed the right ventricle, was propelled down the pulmonary artery to

one lung for oxygenation, and returned to the left heart, leading to the coronary circulation as the base of the systemic circulation.

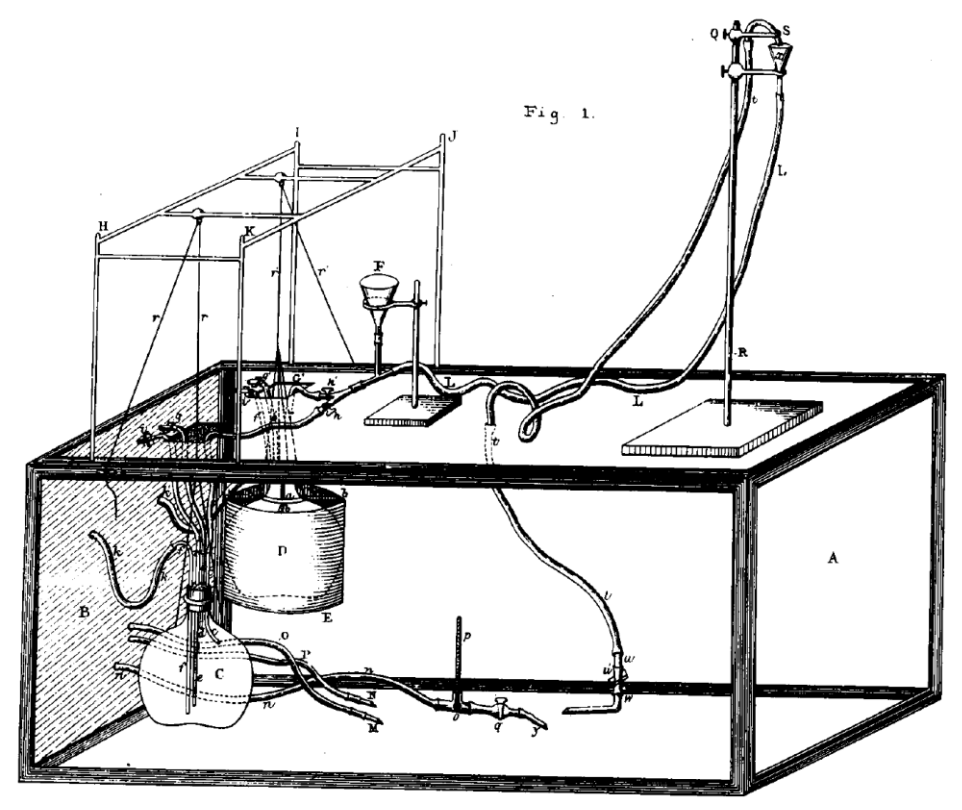


Figure 2.2: H.N. Martin Mammalian heart-lung experimental setup[15].

The Mariotte flasks C and D (see Figure 2.2) were administered by the jugular vein into the RA and ventricle of a dog undergoing artificial respiration, which was situated in a warm, humid environment. Blood subsequently traversed the lungs, entered the left heart, and was expelled into the aorta, where tube t was positioned, discharging into funnel X (see Figure 2.2). Aortic pressure was adjusted by moving the support Q, (see Figure 2.2) which holds tube t, up or down the vertical rod R. The blood from funnel X traversed tube L to flask D for the filling of the right heart via tube N, which terminated in tube y injected into the superior vena cava. The flasks C and D were suspended by cords R and R' and may be elevated or lowered to achieve the required venous pressure. An artificial circulation was sustained in this heart-lung preparation, allowing for independent modulation of pre- and afterload. Cannula M was inserted into the right carotid artery, whereas cannula N was inserted into the left carotid artery. The tubes O and P were linked to the wooden left side of the chamber, connecting to manometers for the measurement of pressure and pulse rate on a big kymograph[11], [15].

2.3 Langendorff Perfusion System

The isolated perfused mammalian heart preparation was developed by Oscar Langendorff in 1895. The technique was formulated based on the isolated perfused frog heart pioneered by Elias Cyon at the Carl Ludwig Institute of Physiology in Leipzig,

Germany, in 1866 [13]. Langendorff proceeded to extract a mammalian heart, perfuse it, and sustain its viability for several hours[1], [11].

Langendorff's investigations were predominantly conducted on felines, with additional trials on rabbits and canines [1], [13]. Langendorff's initial and unexpected observation was that the excised, evidently deceased or dying heart might be revived with perfusion. The heart regained automaticity and sustained it for several hours. This was seen as evidence that the perfusion of the coronary arteries with blood, serving as a nourisment, is adequate to elicit the normal heartbeat, an intrinsic characteristic of this organ. Langendorff deduced that the absence of blood in the ventricular cavities of his preparation indicated that blood within these cavities does not influence excitability in the mammalian heart. Experiments conducted on this isolated perfused heart revealed that brief vagal stimulation and the administration of potassium chloride led to instantaneous cardiac arrest [1]. Muscarine elicited a negative chronotropic and inotropic response, culminating in diastolic arrest, akin to vagal stimulation. Atropine exerted an antagonistic effect. Elevated temperature resulted in tachycardia, while decreased temperature caused bradycardia. Solitary electrical stimulation elicited postextrasystolic potentiation of contraction, while stimuli of increased frequency and intensity resulted in fibrillation. Coronary artery closure caused contractile failure and cardiac arrest, which was rectified by the restoration of coronary blood flow.

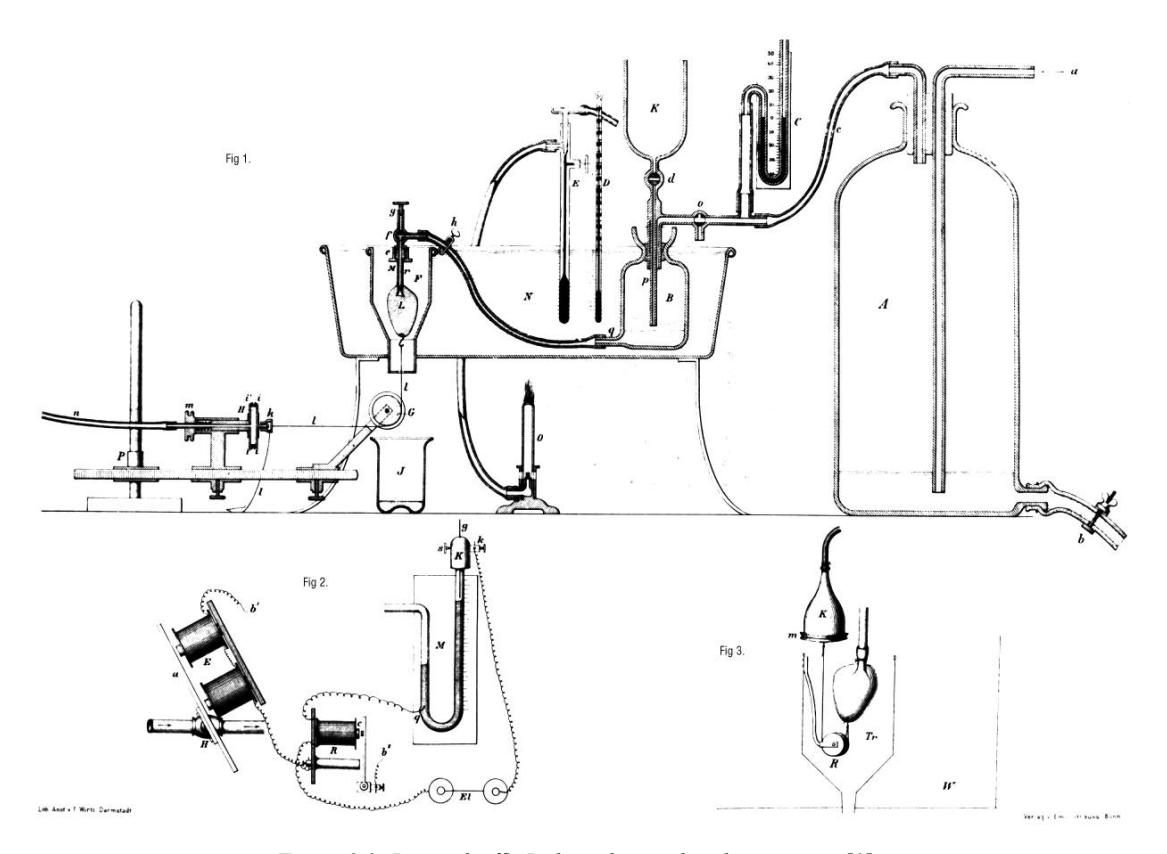


Figure 2.3: Langenlorff's Isolataed mamalian heart system[1].

Defibrinated blood from the corresponding species was utilized for the perfusion. The critical component is the injection cannula M (see Figure 2.3), which is injected into the aorta of the heart situated within a tiny container F (Figure 2.3). The cannula M is

linked through a tube to the blood bottle B (see Figure 2.3), which can be replenished from the reservoir K. The diminutive container and the blood vial are submerged in the water bath N, which can be heated by the Bunsen burner O(see Figure 2.3). The ejection from the heart drops into beaker J. The perfusion pressure is governed by manometer C which is automatically managed by an advanced device linked through valve H to the pressure air cylinder A. The contraction of the isolated heart is documented by connecting a string from the apex of the heart via a wheel to the membrane of a Marey capsule. The membrane's displacement is conveyed to a lever and documented on a kymograph. A more advanced double-membrane technology was employed for recording.

2.3.1 Perfusion Mechanism

The method's fundamental premise was administering blood into the heart via a cannula placed and secured in the ascending aorta. The retrograde flow in the aorta caused the aortic valve leaflets to close, preventing the perfusion fluid from entering the left ventricle. Consequently, the complete perfusate flowed into the coronary arteries through the ostia at the aortic root. Upon traversing the coronary circulation, the perfusate was emptied into the right atrium through the coronary sinus. The perfusion pressure throughout the experiment was maintained consistently by employing a constant hydrostatic pressure of the perfusate. The assessment of coronary flow was conducted by quantifying timed volumes of perfusate exiting the right atrium [1]. The measurement of coronary flow using the volumetric assessment of right atrial outflow across time, exhibited certain shortcomings. This occurred due to aortic valve incompetence, allowing outflow from the heart without the perfusate traversing the coronary circulation. Measurements were not instantaneous either. In 1939, Katz altered the constant pressure technique initially developed by Langendorff, implementing perfusion at a constant flow rate instead. Coronary perfusion pressure variations were readily observed and utilized as an indicator of coronary vascular resistance [16]. The system typically operated under normothermic conditions (~37 °C) to preserve the heart's physiological function and metabolic activity, as in that way ensures that enzymatic reactions, coronary flow, and electrical activity closely mimic in vivo conditions [17].

2.3.2 Contractility

Consistent heart rate maintenance is crucial for acquiring accurate contractility measures in Langendorff-perfused heart studies, as evidenced by Soliman's research. The study demonstrated that hearts without pacing displayed a gradual reduction in heart rate, resulting in variability in left ventricular end-diastolic pressure and peak systolic pressure. This reduction may result in inconsistent contractility assessments owing to modified calcium cycling and myocardial relaxation. Paced hearts exhibited a constant heart rate of 300 beats per minute, hence ensuring more consistent contractile activity [18].

2.3.3 The importance of Langendorff's Model

The mammalian isolated heart preparation, established by Langendorff in 1895 for measuring the amplitude and frequency of cardiac contractions, entails perfusing the coronary circulation through the severed aortic stump. The model is a widely used ex vivo heart perfusion technique that allows for the isolated study of cardiac function, metabolism, and pharmacological responses under controlled conditions. Furthermore, allows researchers to evaluate intrinsic cardiac features by keeping the heart functional outside the body, hence eliminating systemic factors like neurological or hormonal regulation.

The technique was subsequently modified by Porter [19] for further analysis of the coronary circulation. The initial investigations focused on the physiology of the isolated heart, however, the methodology was subsequently utilized to investigate the pharmacological responses of the coronary vasculature with drugs like adrenaline [20]. A constant perfusion pressure was employed, and the coronary vascular responses were assessed by measuring alterations in outflow. By perfusing the isolated heart with a specific solution, researchers may accurately evaluate the effects of different pharmacological drugs on cardiac contractility, heart rate, coronary flow, and electrophysiological characteristics. Numerous research also, focused on evaluating antiarrhythmic medicines, inotropes, vasodilators, and cardioprotective medications, as this facilitates real-time observation of myocardial responses. Pharmacological agents have been investigated on coronary arteries isolated from the heart, however, the reactions of these veins may not accurately reflect the behavior of the entire coronary vascular bed [21], [22], [23].

Currently, numerous cardiovascular researchers employ this essential technology in diverse manners to examine the heart, ranging from analyzing the impact of a singular gene modification on cardiac physiology to exploring innovative therapeutic approaches to safeguard the heart against ischemia and other adversities [24], [25], [26], [27].

2.4 Bubble Formation and Trapping Mechanism in Heart Perfusion Systems

Bubble formation typically occurs through three primary mechanisms: gas supersaturation, pressure drops, and turbulence-induced entrainment. Gas supersaturation arises when the partial pressure of dissolved gases in the perfusate exceeds equilibrium solubility, leading to nucleation of gas bubbles and this process is described by Henry's Law [28]:

Equation 2.1

$$p = k_H C$$

where C is the gas concentration, k_H is Henry's constant, and $P_{\rm ga}$ is the gas partial pressure.

In particular, when the local system pressure decreases or temperature increases, the gas solubility falls, resulting in gas release from solution. Pressure drops, particularly in regions of sudden expansion, or constricted flow, can further induce bubble formation through cavitation, or when the perfusate is pumped from a pressurized reservoir, typically maintained slightly above atmospheric pressure, through the tubing and into the lower-pressure environment near the heart, the static pressure within the fluid decreases [29], [30]. More specifically according to Henry's law the equilibrium solubility of a gas in a liquid is directly proportional to the partial pressure of that gas, therefore as the local pressure falls, the equilibrium solubility decreases, and any excess dissolved gas becomes supersaturated [28]. This supersaturation leads to the nucleation of microbubbles or visible gas bubbles within the perfusate, which is undesirable, as it can obstruct flow and leading to microemboli in the coronary circulation [28]. Moreover, Henry's constant k_H increases with temperature, meaning that gas solubility decreases as the perfusate is warmed, so when the perfusate is heated from room temperature to physiological temperature before entering the heart, the equilibrium concentrations of dissolved oxygen and carbon dioxide decrease [28]. Additionally, air may enter the perfusion circuit through loose or leaking connections and also, turbulence and shear forces at high Reynolds numbers enhance gas-liquid interface area, promoting bubble entrainment from open reservoirs or leaks in the circuit [31].

The removal of bubbles in perfusion systems is achieved through a combination of gravitational separation, centrifugal effects, and filtration. Gravity-based separation relies on density differences between the gas and liquid phases, as bubbles rise, low-velocity chambers are used to increase residence time, allowing gas accumulation at the upper section of the trap [32]. Filtration mechanisms further improve bubble capture by using porous membranes or meshes. Filters with pore sizes smaller than the bubble diameter promote bubble adhesion and coalescence, often aided by surface tension effects and hydrophobic—hydrophilic surface interactions [33], [34].

For example, Md.N. Inamadar et al. [35] in their research used a passive air bubble trapping device to avert air embolism during cardiac perfusion. A water-jacketed coil was integrated into the system, linked to a stopper including a latex injection port situated between the stopper and the outlet. An upper limb was incorporated into the outflow channel as a passive bubble trap to prevent air bubbles from reaching the heart, thereby capturing any added air prior to perfusion.

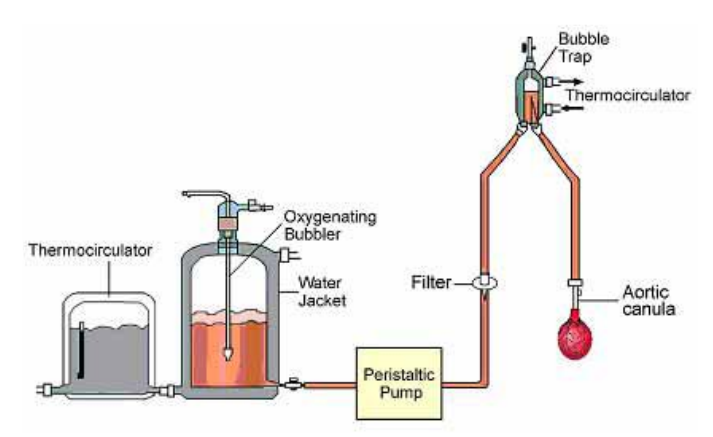


Figure 2.4 Depiction of the Langendorff System. The water jacket holds the perfusate fluid, which is heated by the thermocirculator and oxygenated via the oxygenator bubbler. The perfusate is propelled by a peristaltic pump, subsequently traversing a filter to the bubble trap, where it is coupled to a thermocirculator to ensure a consistent temperature, before perfusing the heart through the aortic cannula [18].

2.5 Computational Fluid Dynamics (CFD) in Biomedical Engineering

Computational Fluid Dynamics (CFD) constitutes a fundamental methodology in the biomedical engineering field, which can offer a rigorous framework, by analyzing quantitative of complex biological fluid flows that are often difficult to direct through experimental measurements [36]. From the implementation of numerical solutions of the Navier–Stokes equations, CFD can enable the characterization of hemodynamic and aerodynamic parameters such as velocity fields, pressure distributions, and wall shear stresses, which are critical in understanding the pathophysiological mechanisms underlying cardiovascular and respiratory diseases [37]. For instance, Santiago et al. (2018) developed a fully coupled fluid–electro–mechanical model of the human heart using the Alya Multiphysics solver, where the blood flow in the cardiac cavities was described by the incompressible Navier–Stokes equations solved with an Arbitrary Lagrangian–Eulerian (ALE) CFD scheme [38].

Furthermore, CFD can give the possibility of the investigation of blood flow through cardiac valves, ventricles, and arterial networks, the evaluation of medical implants such as stents and prosthetic valves, as well as the study of airflow in the nasal cavity and pulmonary system for drug delivery optimization and surgical planning [37]. In addition, the integration of CFD with advanced imaging modalities, such as CT and MRI, has led to the development of patient specific computational models, which can be used to promote more precise diagnostic assessments and individualized therapeutic interventions [37].

2.6 Role of T3 Hormone in Cardiac Function

In current clinical practice, most perfusion systems have cell-based perfusates, typically composed of leukocyte-depleted, packed red blood cells supplemented with anticoagulants, vasodilators, and metabolic additives. Such blood based solutions provide physiological oxygen carrying capacity, but their use is often unsuitable for prolonged perfusion due to hemolysis, increased viscosity, and pro-inflammatory effects over time [39]. In recent studies have been showed that cell free perfusates, such

as Ringer's lactate or Steen solution which are enriched with nutrients and metabolic substrates, can sustain normothermic perfusion more effectively for an extended period of time [40]. In addition, recent experimental work has shown that supplementing Krebs-Henseleit (K-H) buffer with high concentrations of L-triiodothyronine (T3) preserves ex vivo rat hearts during normothermic perfusion and, importantly, activates intracellular repair and survival signaling pathways [39], [40].

The use of L-triiodothyronine (T3) as a metabolic support agent during heart perfusion has been shown to prevent tissue hypoxia, mitochondrial dysfunction, and post-ischemic myocardial depression. For example, in resent studies it was observed that the early administration of T3 in rats reduced the cardiac and hepatic hypoxia, decreased the lactate accumulation, and improved mitochondrial respiratory efficiency, leading to a direct cytoprotective effect on cardiomyocytes under hypoxic stress [39]. Also, Lourbopoulos et al. have shown that the T3 enhances mitochondrial biogenesis, upregulates oxidative phosphorylation enzymes, and stabilizes endothelial function, leading to improved microvascular perfusion and oxygen utilization [41], [42].

2.7 Organ Care Systems Heart, OCS Systems

Organ Care Systems (OCS) are portable ex vivo perfusion platforms that are developed to maintain donor organs in a metabolically active state between retrieval and transplantation, which allows to transport the organs for longer distances [43]. The OCS Heart systems preserve the organ under normothermic, oxygenated conditions using an autologous, red blood cell based perfusate, that continuously circulates through the coronary vasculature [3]. Functionally, this perfusion configuration is based on the classical Langendorff principle, where modern OCS devices operate initially in this Langendorff mode (resting mode) before optionally switching to a "working-heart" configuration that introduces physiological preload and afterload to assess cardiac performance [44]. Heart transplantation has conventionally relied on hearts sourced from donors after brain death, enabling in situ evaluation of cardiac function and the donor allograft's potential for transplantation prior to surgical procurement [45].

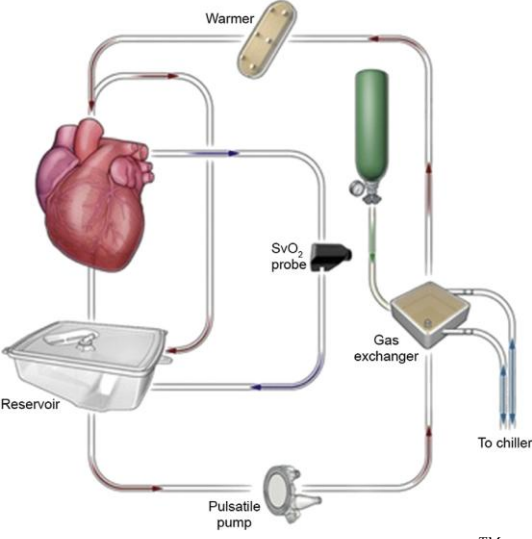


Figure 2.5: Schematic Representation of Organ Care Systems (OCSTM) by TranMedics [46].

Over 60 million people worldwide suffer from heart failure, and its incidence is anticipated to rise significantly due to aging populations[3], [47]. In 2010, the median age of heart allograft donors was 31 years, and this age has remained largely steady at non-European transplant hospitals for more than a decade [48]. Conversely, European facilities have already experienced an increase, with the median donor age attaining 42 years for heart recipients across all age groups. Since that time, the age of donors has consistently risen on a global scale as in 2025, the median age of offered donor hearts in Europe is 55 years, although accepted hearts average 45 years, underscoring a persistent need on older donors relative to non-European regions [4]. Long-term morbidity and mortality rates continue to be elevated and many patients evolve to severe heart failure and have consistently debilitating symptoms even though the advancements [4]. Thus, given the rising prevalence of heart failure, improving donor heart preservation through systems like the OCS is essential to meet the growing clinical demand for transplantation.

$oldsymbol{3}$ Theoretical Background

3.1 Eulerian vs. Lagrangian frameworks in CFD.

The calcification of numerical models of particle-fluid flows is based on how the particle, and the fluid interact and differ in how the dispersed phase is represented. Those methods are known as Eulerian and Lagrangian [49]. In the Eulerian framework, each phase is treated as an interpenetrating continuum and formulate separate conservation equations for mass, momentum, and energy on a fixed control volume [50], [51], [52]. The Eulerian framework is mostly used to flows where both phases occupy significant volume fractions and there are strong phase interactions which must be resolved. However, its continuum assumption can be limited in dilute systems, as it does not resolve particle history or discrete dispersion effects [51].

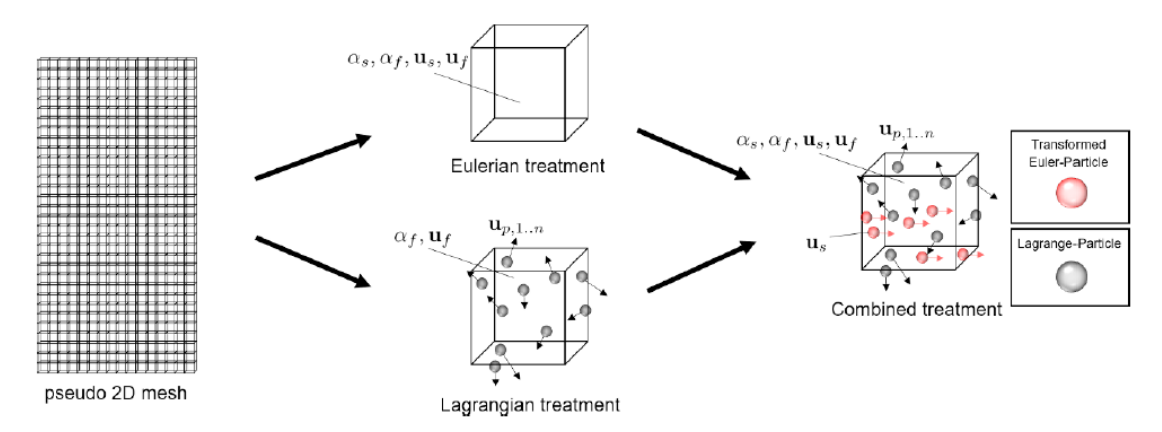


Figure 3.1 Comparison of Eulerian, Lagrangian, and Combined Frameworks for Particle–Fluid Interactions [53].

In the Lagrangian framework, the dispersed phase is represented as a collection of discrete elements whose trajectories are calculated by solving force balance equations along their paths through the continuous carrier phase. The Lagrangian framework, provides in that way a more detailed information on particle-scale dynamics and allows the direct incorporation of additional forces such as drag, buoyancy, and lift, but its computational expense increases significantly with the number of discrete elements tracked [53], [54].

In practice, hybrid methods have been developed that combine the Eulerian and Lagrangian methods, such as Eulerian-Lagrangian, Eulerian-Eulerian and Lagrangian-Lagrangian models, in order to balance computational efficiency with the physical accuracy. The combination of those models can treat the dispersed phases as Lagrangian elements while simultaneously maintaining Eulerian field descriptions of the continuum, making the application of CFD into a broader range of multiphase flow conditions [49], [52], [53].

3.2 Fluid Dynamics of Bubbles in liquid

The essential physical laws regulating the motion of bubbles in a liquid and energy transfer to bubbles are Newton's second law, the principle of mass conservation, and the first law of thermodynamics. The application of these principles to a small control volume around a bubble, results in governing fluid equations of the Navier-Stokes, continuity, and energy [55].

3.2.1 The Navier-Stokes and Continuity Equations

The motion of a fluid element is governed by Newton's second law, which states that the rate of change of momentum equals the sum of all external forces acting on it. When Newton's second law is applied to an infinitesimal element of fluid, it can describe the motion of a fluid. For an incompressible Newtonian fluid with density ρ and constant viscosity μ and considering gravity as the only body force, the resulting momentum balance for an incompressible fluid leads to the Navier–Stokes equation of motion [55]:

Equation 3.1

$$\rho \frac{D\boldsymbol{u}}{Dt} = \rho \boldsymbol{g} - \nabla p + \mu \nabla^2 \boldsymbol{u}$$

where \mathbf{u} is the velocity vector, \mathbf{p} the pressure, and \mathbf{g} the gravitational acceleration vector. The left-hand side represents the rate of change of momentum per unit volume, which can be expressed through the substantial derivative and includes two contributions, the local derivative:

Equation 3.2

$$\frac{D}{Dt} = \frac{\partial}{\partial t} + \boldsymbol{u} \cdot \boldsymbol{\nabla}$$

which captures the time-dependent changes at a fixed point in space, and the convective term accounts the changes experienced by a fluid element as it moves with the flow. The right-hand side represents, respectively, the gravitational force (ρ g) acting on the fluid, the pressure gradient force, and the viscous force due to velocity gradients. Adding to the Navier–Stokes equation the continuity equation, ensures mass conservation [55]:

Equation 3.3

$$\frac{\partial t}{\partial \rho} + \nabla \cdot (\rho \boldsymbol{u}) = 0$$

For incompressible fluids, continuity equation reduces to:

Equation 3.4

$$\nabla \cdot \boldsymbol{u} = 0$$

3.2.2 Motion of Bubbles in Liquids

The motion of a bubble in a liquid is determined from Newton's second law, as when a bubble is moving within a liquid, several distinct forces contribute to its dynamics. One of the main forces that affects how a bubble is moving in a liquid is the buoyancy force, which causes bubbles to rise. Buoyancy results from the difference in density between the liquid (ρ) and the gas (ρ_{gas}) inside the bubble and depends on the bubble's diameter. On the other hand, the drag force opposes the bubble's movement by resisting acceleration and helps bubbles establish a terminal rising velocity that depends on the bubble's size, shape, and the liquid's properties. Drag force gradually will balance the buoyancy, by allowing the bubble to rise at a nearly constant velocity. Additionally, as a bubble accelerates or decelerates, surrounding fluid must be displaced, creating an added mass effect. Lift forces can also develop when bubbles are in shear flows or rotating liquid fields, which cause their trajectories to deviate laterally and local pressure gradients further influence the bubble's movement and path, especially in complex flow environments.

The Lagrangian formulation of particle motion states that the rate of change of a particle's linear momentum is equal to the sum of all forces acting upon it. This can be expressed as [56]:

Equation 3.5

$$m_p \frac{dV}{dt} = F_{body} + F_{surf} + F_{coll}$$

where:

- m_p: particle mass
- F_{body}: body forces (proportional to the particle mass, e.g., gravity and buoyancy)
- F_{surf}: surface forces (scaling with particle surface area, e.g., drag and lift)
- F_{coll}:collision forces arising from interactions with other particles or with walls

The corresponding particle position equation is given by:

Equation 3.6

$$\frac{dx_p}{dt} = v_p$$

The Integration of the above equations gives the particle trajectory as a function of time. The body force is assumed to be equivalent to the gravitational force, acting in the direction of gravitational acceleration (g):

Equation 3.7

$$F_{body} \approx F_G = m_p g$$

The surface force acting on a spherical particle can be expressed in terms of the local pressure and viscous stresses acting over the particle surface:

Equation 3.8

$$\mathbf{F}_{surf} = \iint \left(-P\mathbf{i_r} + K_{rr}\mathbf{i_r} + K_{r\theta}\mathbf{i_\theta} + K_{r\varphi}\mathbf{i_\varphi} \right) dA_p$$

where i_r is the unit vector in the radial direction, and i_θ , i_ϕ are the unit vectors in the polar (θ) and azimuthal (ϕ) directions, respectively. An alternative and more practical approach is to decompose the total surface force into a linear combination of distinct fluid-dynamic contributions:

Equation 3.9

$$F_{surf} = F_D + F_L + F_{VM} + F_H + F_S + F_{Br} + F_{VT}$$

where:

- F_D: Drag force, opposing the relative motion between particle and fluid,
- F_L: Lift force, arising from particle spin or velocity gradients in the surrounding flow,
- F_{VM}: Virtual mass (added mass) force, due to acceleration of the displaced fluid.
- F_H: History (Basset) force, accounting for unsteady stresses over the particle surface.
- Fs: Stress force, representing fluid stresses in the absence of the particle,
- F_{Br}: Brownian force, caused by random molecular collisions,
- $F_{\nabla T}$: Thermophoretic force, resulting from molecular interactions along a temperature gradient.

For bubbles, the equation 3.5 can be expressed as follows[55], [57]:

Equation 3.10

$$m_b \frac{d\mathbf{u}_b}{dt} = F_B - F_G - F_D + F_L + F_{AM} + F_P$$

Where:

- F_B: buoyancy force
- F_G: gravity force
- F_D: drag
- F_L:lift
- F_{AM}: added mass
- F_p: pressure gradient forces

The buoyancy force is equal to [58], [59]:

Equation 3.11

$$\mathbf{F}_{B} = \rho_{l} \mathbf{g} V_{B}$$
 or

Equation 3.12

$$F_B = \frac{4}{3}\pi r^3 (\rho_l - \rho_{gas})g \approx \frac{4}{3}\pi r^3 \rho_l g \quad (\rho_{gas} \ll \rho_l)$$

Where ρ_l is the density of the liquid and V_B is the bubble volume. As it can be observed from the above equation, the buoyancy force acting on a bubble is directly proportional to the volume of liquid displaced, which depends on the cube of the bubble radius. Since the volume of a spherical bubble is the $V_B = \frac{4}{3}\pi r^3$, buoyant force increases rapidly with increasing bubble size. In contrast, the bubble's weight, which is depending on the gravity acting on the gas inside, increases slowly, as the gas density is several orders of magnitude smaller than that of the liquid, meaning that as the bubble radius increases, the net upward force, buoyancy minus the weight, becomes larger and promotes faster upward motion.

As the bubble is moving through the liquid, it also experiencing the drag forces, which are oppose its motion. More specifically, the drag force arises from viscous shear and pressure distribution around the bubble surface and depends on the bubble's projected area A_P and the drag coefficient C_D, which varies with the Reynolds number. The drag force can be expressed as [55]:

Equation 3.13

$$F_D = \frac{1}{2}\rho_l v_B^2 C_D A_p$$
 or

Equation 3.14

$$\boldsymbol{F_D} = \frac{1}{2} C_D \rho_l A_p (\boldsymbol{u_l} - \boldsymbol{u_b})^2$$

where C_D is the drag coefficient, $A_p = \pi r^2$ is the projected area, u_ℓ is the velocity of the liquid, and u_b the velocity of the bubble and v_B is the magnitude of the relative velocity between a bubble and the fluid. At low Reynolds numbers (Re < 1), viscous forces dominate and the flow around the bubble is classified as Stokes flow. Under the condition of drag follows Stokes' law [55]:

Equation 3.15

$$\boldsymbol{F_D} = 6\pi\mu r(\boldsymbol{u}_b - \boldsymbol{u}_l)$$

At higher Reynolds numbers, the drag coefficient becomes a function of both Reynolds and Eötvös number.

Given the balance of forces of buoyancy with drag and gravitational [55]:

Equation 3.16

$$F_D = F_B - F_G$$

The external liquid pressure, P, surrounding a bubble of radius R, is linked to the internal pressure, P_B, by [60]:

Equation 3.17

$$P_B - P = \frac{2\sigma}{R}$$

where the σ is the surface tension.

For smaller bubbles, the surface tension is strong relative to buoyancy and maintains spherical shape stability. When the bubble radius increases, the surface tension effects weaken and allows the deformation into ellipsoidal or spherical cap shapes [55]. The correlation between buoyancy and surface tension is determined by the Bond number, where if Bo<1, the surface tension dominates and if Bo>1 buoyancy dominates [55]:

Equation 3.18

$$Bo = \frac{(\rho_l - \rho_g)\boldsymbol{g}r^2}{\sigma}$$

The surface tension force acts tangentially along the bubble interface and helps maintain its spherical shape for small diameters and resist to deformation. In flows with velocity gradients or rotation, a lift force which is commonly referred to as the *Saffman lift force*. This force acts perpendicular to the direction of motion and to the local velocity gradient and causes the bubble to migrate laterally within the flow field. The Saffman lift force is given by the following equation [61]:

Equation 3.19

$$F_I = C_I \rho_I V_h (u_I - u_h) \times (\nabla \times u_I)$$

Where C_L is the lift coefficient which depends on Eötvös number and flow regime.

And the added mass force, where C_A is the added mass coefficient [55]:

Equation 3.20

$$F_{AM} = C_A \rho_l V_b \frac{D}{Dt} (\boldsymbol{u}_l - \boldsymbol{u}_b)$$

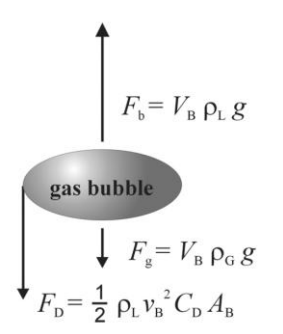


Figure 3.2 Balancing forces on a bubble [59]

Additionally, in the Lagrangian method, for each particle the equation of the transient momentum is solved as below [54], [62]:

$$\frac{d\mathbf{u_p}}{dt} = F_D(\mathbf{u} - \mathbf{u_p}) + \frac{\mathbf{g}(\rho_p - \rho)}{\rho_p} + \mathbf{F_{\alpha}}$$

Where:

• **u**_p: particle velocity

• u: local continuous-phase (fluid) velocity

• Fa: additional forces

And Drag acceleration F_D:

$$\boldsymbol{F_D} = \frac{3\mu C_D R e_p}{4\rho_p d^2}$$

with particle Reynolds number:

$$Re_p = \frac{\rho D_P |u - u_p|}{u}$$

and a typical drag law Schiller-Naumann for spheres:

$$C_D = \begin{cases} \frac{24}{Re_p}, & if \ Re_p \le 0.1 \\ \\ \frac{24}{Re_p} (1 + 0.15Re_p^{0.687}), & if \ 0.1 \le Re_p \le 10^3 \\ \\ 0.44, & if \ Re_p > 10^3 \end{cases}$$

Turbulence also has a critical role in bubble dynamics, as it modifies both the velocity distribution of the continuous phase and the forces acting on the bubble. In turbulent flows, eddies of various scales can enhance bubble dispersion, cause fluctuations in bubble trajectories, and modify their residence times within a system[51]. Small scale turbulence in particular can strongly affect the instantaneous velocity of bubbles, leading to highly non-linear and irregular motion compared to the relatively stable rise observed in laminar conditions [51].

3.3 Computational Modeling

3.3.1 Discrete Phase Model (DPM)

The discrete phase model is a computational fluid dynamics framework employed to simulate motion and interaction of distinct solid or liquid particles suspended inside a fluid [56]. In the context of DPM model, the trajectory of each particle is monitoring, as it traverses the fluid and computes the pressures exerted upon it. On the other hand, in the context of CFD, the word secondary phase denotes a phase of matter that is suspended or distributed inside a primary phase, which is generally a continuous phase or fluid, where this type of multiphase mixture must is examined within the Lagrangian framework.

To describe multiphase flow regimes, several key definitions are required. A particle refers to a relatively small, unattached body which is suspended within a continuous phase, while the group of such particles of the same material constitutes the dispersed phase. As consists of one dispersed phase and one continuous phase, it is referred to as two-phase flow and these concepts can be extended to systems involving multiple phases [56]. The term dispersed flow refers to a regime where the forces acting on the particle surface are predominantly influenced by interactions with the surrounding continuous flow, rather than by direct interactions among adjacent particles [56]. The dispersed is solving within the Lagrangian framework, while the continuous phase is solving within the Eulerian framework, meaning that DPM is a Lagrangian-Eulerian approach.

3.3.2 SST k-ω Model

The $k-\omega$ turbulent kinetic energy–specific dissipation rate model was originally developed by Wilcox [63]. This two-equation model solves additional transport equations for the turbulent kinetic energy k and the specific dissipation rate ω , which describes the rate at which turbulence energy is converted into thermal energy per unit turbulent kinetic energy [63]. The $k-\omega$ model is highly sensitive to the freestream value of ω , which limits its reliability in external and far-field flows. For that reason, Menter (1994) proposed the Shear Stress Transport (SST) $k-\omega$ model [64], [65], which blends the $k-\omega$ formulation near walls with the $k-\varepsilon$ formulation away from them using a blending function. The SST $k-\omega$ model is a two-equation eddy-viscosity and a low Reynolds turbulence model. The equations of the SST $k-\omega$ model are [65]:

Equation for k:

Equation 3.21

$$\frac{D\rho k}{Dt} = \tau_{ij} \frac{\theta u_i}{\theta \chi_i} - \beta^* \rho \omega k + \frac{\theta}{\theta \chi_i} \left[(\mu + \sigma_k \mu_t) \frac{\theta k}{\theta \chi_i} \right]$$

And the equation for ω :

Equation 3.22

$$\frac{D\rho\omega}{Dt} = \frac{\gamma}{\nu_t}\tau_{ij}\frac{\theta u_i}{\theta \chi_j} - \beta\rho\omega^2 + \frac{\theta}{\theta x_j}\left[\left(\mu + \sigma_\omega\mu_t\right)\frac{\theta\omega}{\theta x_j}\right] + 2(1 - F_1)\rho\sigma_{\omega^2}\frac{1}{\omega}\frac{\theta k}{\theta x_j}\frac{\theta\omega}{\theta x_j}$$

The eddy viscosity is defined as:

Equation 3.23

$$v_t = \frac{a_1 k}{\max(\alpha_1 \omega; \Omega F_2)}$$

Where ρ is the density of the fluid, k is the turbulent kinetic energy, u_i is the velocity component in x_i direction, τ_{ij} the Reynolds stress tensor, μ the molecular dynamic viscosity, μ_t turbulent (eddy) viscosity, σ_k the Turbulent Prandtl number for k, σ_{ω} the Turbulent Prandtl number for ω , $\sigma_{\omega 2}$ the alternative Turbulent Prandtl number, β^* the model coefficient and β the dissipation coefficient in ω equation , ω the specific dissipation rate, γ the model coefficient and F_1 and F_2 empirical functions. Also, $D/Dt=\theta/\theta t+u_i\theta/\theta x_i$ is the Lagrangian derivative.

3.3.3 Turbulence Interactions with Particles

Turbulence is the three-dimensional macroscopic expression of inertia and frictional forces resulting from increased vorticity and strain, attributed to the division of mechanical energy into rotational and translational forms[51]. The impact of turbulence on small submerged particles is a convective phenomenon that results in an ostensibly random dispersion of the particles throughout the flow field. A prominent result of this influence is the augmentation of the trajectory traversed by a particle as it transitions from one sector of the flow to another. The designated trajectory will consistently exceed that of laminar flows in turbulent flows within a specified geometrical sector, which exemplifies the concept of turbulent particle dispersion.

In dispersed multiphase systems, turbulence affects bubble dynamics through the below mechanisms [51]:

- Enhanced Mixing and Dispersion: Turbulence increases bubble dispersion by introducing random velocity fluctuations that modify bubble trajectories.
- Turbulent Fluctuation Forces: These include stochastic lift and drag fluctuations, which alter the bubble's slip velocity.
- Eddy–Bubble Interactions: Depending on the bubble size relative to the Kolmogorov length scale, bubbles may either be entrained by large eddies (large bubbles) or experience random oscillations and deformations due to small eddies (small bubbles).

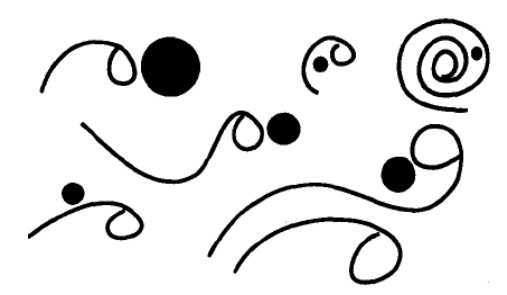


Figure 3.3 Turbulent flows eddy particle interaction [51].

The interaction strength is characterized by parameters such as the turbulent Reynolds number and the Stokes number, which determine how strongly a bubble responds to turbulent fluctuations. When the bubble's relaxation time is much smaller than the turbulent time scales, it follows the fluid motion closely, otherwise, it exhibits slip and preferential concentration in low-vorticity regions. When a small particle enters a turbulent flow and is smaller than the smallest eddy, it is confined inside the eddy for a set amount of time before being influenced by another. Increasing the particle inertia for a small particle, possessing a relaxation period less than all fluid time scales, diminishes the particle's fluctuating velocity while concurrently extending the particle's integral time scale[51]. A medium-sized particle interacts similarly with a larger eddy as a small particle, as previously explained [51]. However, when a medium particle interacts with a smaller or similarly sized eddy, it can either entirely disperse the eddy or alter its structure, contingent upon the nature of the interaction [51]. Furthermore, when a particle has a significant relative velocity with respect to the local turbulent structures, it may move through the eddies faster than the characteristic eddy turnover time and as a result, the particle does not remain within a single eddy for its entire lifetime but instead migrates from one eddy to another before the first eddy decays. This phenomenon is known as the Crossing Trajectory Effect (CTE) [51].

3.4 Bubble Trap Efficiency

The bubble trap efficiency expresses the percentage of bubbles that remained trapped inside the chamber relative to the total number introduced at the inlet. A higher efficiency value therefore indicates that a greater proportion of bubbles were successfully captured and prevented from escaping through the outlet, reflecting the overall effectiveness of the trap in removing air from the perfusion system. Similar CFD modeling techniques and efficiency evaluation methods for fluid-based trapping mechanisms that aim to investigate the efficiency of the bubble trapping mechanism using simulation models, are calculating the efficiency using the following formula [66], [67]:

Equation 3.24

$$n(\%) = \frac{Number\ of\ particle\ retainded\ within\ the\ system}{Total\ number\ of\ particles\ injected} \times 100$$

4 Methodology

4.1 Conceptual design.

The simulations in this study were performed using an Eulerian—Lagrangian framework where the continuous phase, which is the perfusate, was modeled in an Eulerian manner by solving the Navier—Stokes equations across the computational domain and the dispersed phase, meaning the bubbles, was treated in a Lagrangian reference frame using the Discrete Phase Model - DPM. The interaction between the phases was modeled as a two-way coupling, which means that not only were the bubbles influenced by the surrounding liquid flow, but their momentum exchange also acted back on the continuous phase.

The device was designed as a cylindrical chamber with a total volume of 150 mL, with a single inlet and two outlets, as the chamber configuration was selected to enable bubble separation through buoyancy motion while maintaining continuous fluid delivery. The inlet was used for the perfusate entry, while one outlet was designated for bubble removal and the other to return the perfusate to the system. It should be noted that in all simulations the outlet for the bubbles was not used as an active outlet, as it was kept closed considered as a wall, in order to simulate the operating condition in which bubble removal through this port is unavailable and to examine the condition where bubbles entering into the systems and the impact that inlet geometry has. The geometry was created in SolidWorks and imported into ANSYS Fluent.

At the inlet, the continuous phase (perfusate) enters the domain with a defined velocity. Bubbles were injected at the inlet as group of different sizes using the Discrete Phase Model (DPM) in ANSYS Fluent, representing entrained air carried by the perfusate. The injections consisted of groups of spherical bubbles with diameters of 50, 100, 200, 300, 400, and 500 µm and for each bubble size, 250 particles were injected, resulting in a total of 1500 bubbles being introduced into the system.

The outlet of the perfusate allows the continuous phase (perfusate) to exit the bubble trap and it was treated as a pressure outlet. For the dispersed phase, the outlet was defined as an "escape" boundary, so that bubbles reaching the outlet were assumed to leave the system. Finally, the internal walls of the bubble trap formed the housing of the fluid zone, modeled with a no-slip condition for the continuous phase and for the dispersed phase, bubble—wall interaction was set to "reflect," meaning bubbles colliding with the walls were returned to the flow field rather than trapped.

4.1.1 Design of the Bubble Trap

The geometry of the bubble trap was designed based on established features commonly found in commercial medical grade air trapping devices, such as the Capiox® Bubble Trap by Terumo Corporation.

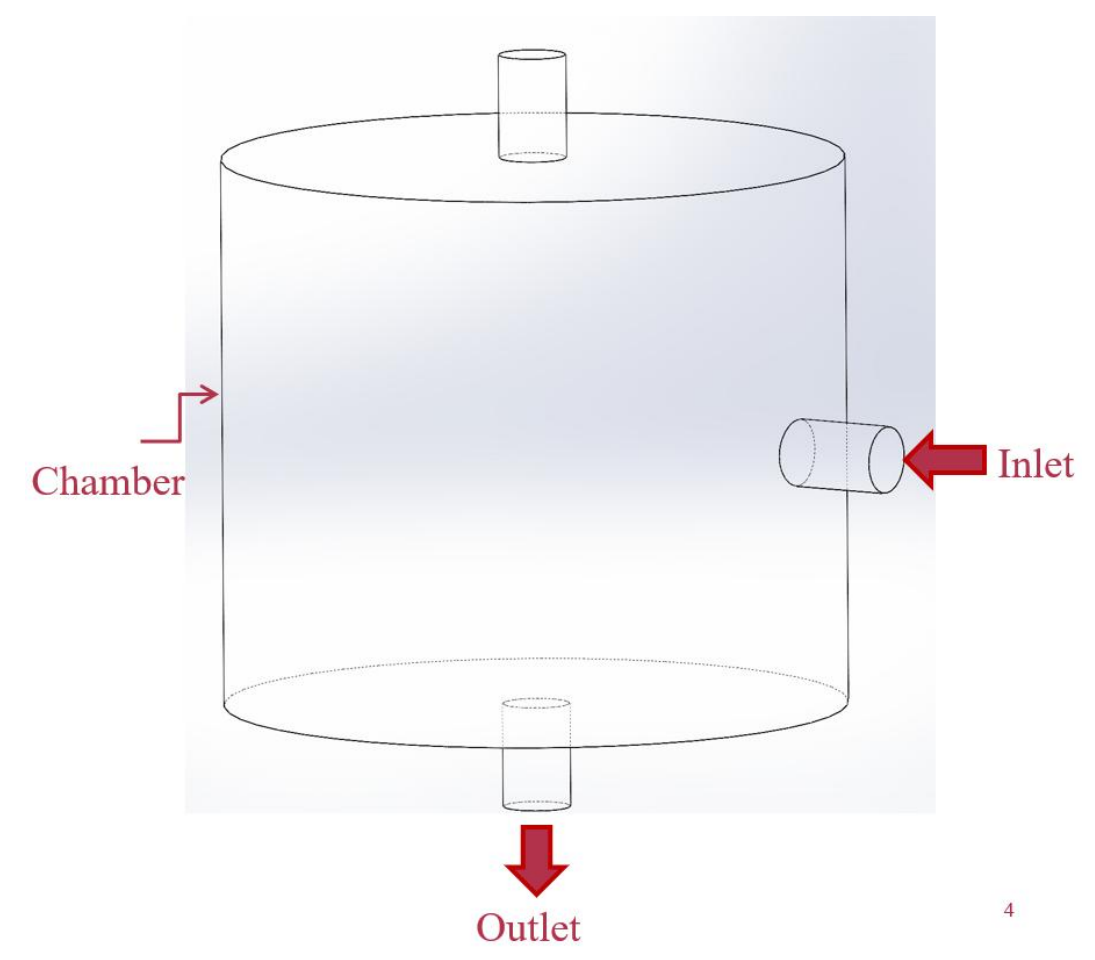


Figure 4.1 SolidWorkds 3D Model of the r30.0×53.0 geometry.

The model consists of a cylindrical housing made of polycarbonate (see Figure 4.1), with an internal volume constrained to approximately 150 mL to reflect clinically relevant capacities and to ensure consistency across all design iterations. The dimensions of the initial configuration include a radius of 30 mm and a height of 53 mm, where the inlet and outlet ports were both modeled with a diameter of 6.4 mm, corresponding to the standard 1/4 inch internal diameter used in aortic lines within perfusion circuits. Furthermore, the inlet was positioned tangentially at the mid-height 26.50mm of the cylindrical chamber wall and the outlet for the perfusate was located centrally at the bottom of the chamber to allow vertical downward flow of the liquid phase, while a secondary outlet, also 6.4 mm in diameter, was placed at the geometric center of the top surface to facilitate the escape of entrained air. This design was labeled as **r30.0×53.0** (see Figure 4.1-4.2).

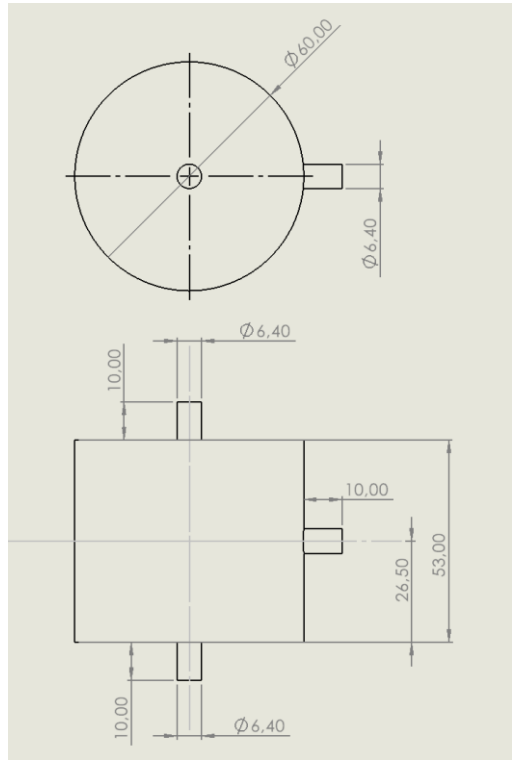


Figure 4.2 Geometrical Design of the Bubble Trap r30.0×53.0 Configuration.

Inlet Height Variation

To investigate the influence of vertical inlet positioning on internal flow behavior and bubble separation efficiency, two additional geometries were developed by modifying the inlet height while keeping all other design parameters constant. These include the fixed internal volume (150 mL), chamber dimensions (radius 30 mm, height 53 mm), and inlet/outlet diameters (6.4 mm). In all cases, the inlet maintained a tangential orientation to preserve the swirling flow characteristics established in the initial design.

In the first variation, the inlet was placed at one-quarter (1/4) of the chamber height from the base, corresponding to 13.25 mm above the bottom surface, positioning the inlet closer to the perfusate outlet at the bottom center of the chamber, in order to evaluate whether a lower inlet position would influence the efficiency of the bubble trap. The corresponding geometry was labeled as **r30.0x53.0_inlet13.25**.

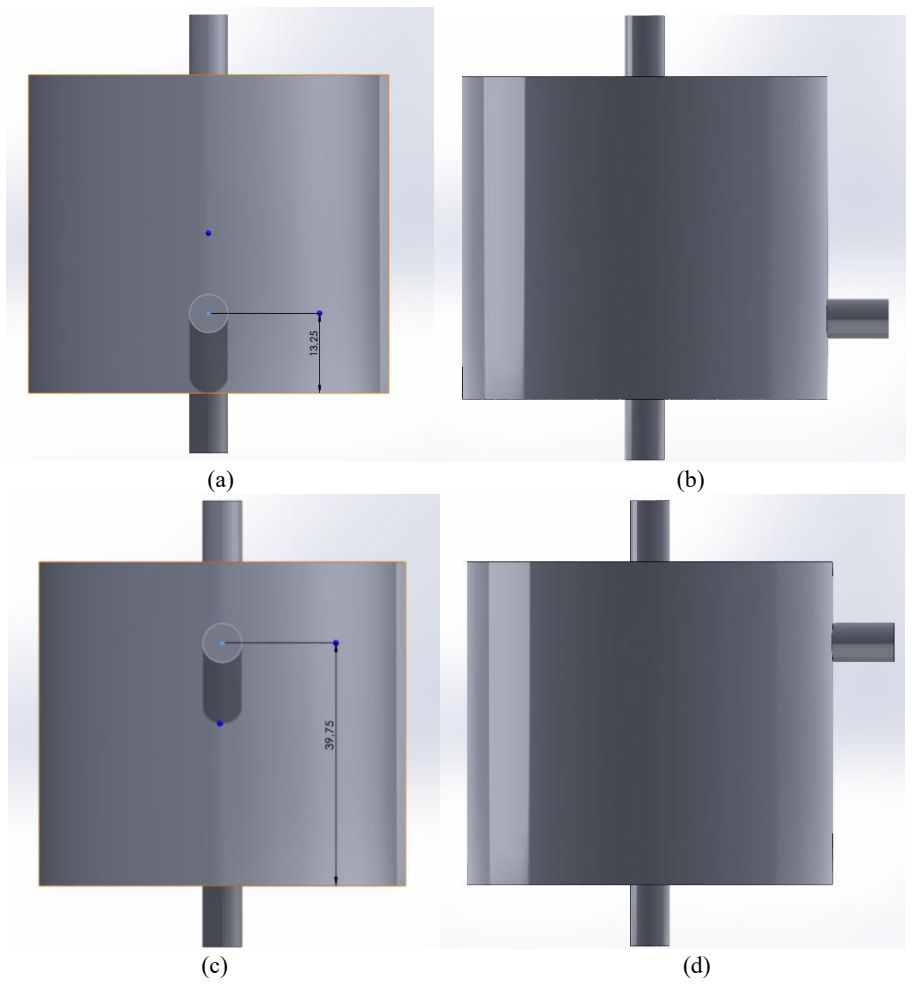


Figure 4.3 SolidWorks design of the geometry (a)-(b) r30.0x53.0_inlet13.25 (c)-(d) r30.0x53.0_inlet39.75.

In the second variation labeled as **r30.0x53.0_inlet39.75**, the inlet was positioned at three-quarters (3/4) of the chamber height, 39.75 mm from the bottom, in order to investigate whether positioning the inlet closer to the top and away from the perfusate outlet would influence the efficiency of bubble removal.

Inlet Angle Variation

Based on the findings of the inlet height analysis, the setup with the inlet at three-quarters (3/4) of the chamber height (39.75 mm from the base) demonstrate superior performance in terms of bubble removal efficiency (see Section 5.1). For this reason, the design of the inlet at 39.75 was selected as the reference geometry in order to investigate the impact of different inlet angulations.

In continuous, while maintaining all the other design parameters constant—including chamber dimensions (radius 30 mm, height 53 mm), inlet/outlet diameters (6.4 mm), and total internal volume (150 mL), the angular orientation of the inlet relative to the tangential direction of the cylindrical wall was varied, three inlet angles were tested: 30°, and 45°. The corresponding geometries were labeled r30.0x53.0 inlet39.75 15deg, r30.0x53.0 inlet39.75 30deg, and r30.0x53.0 inlet39.75 45deg.

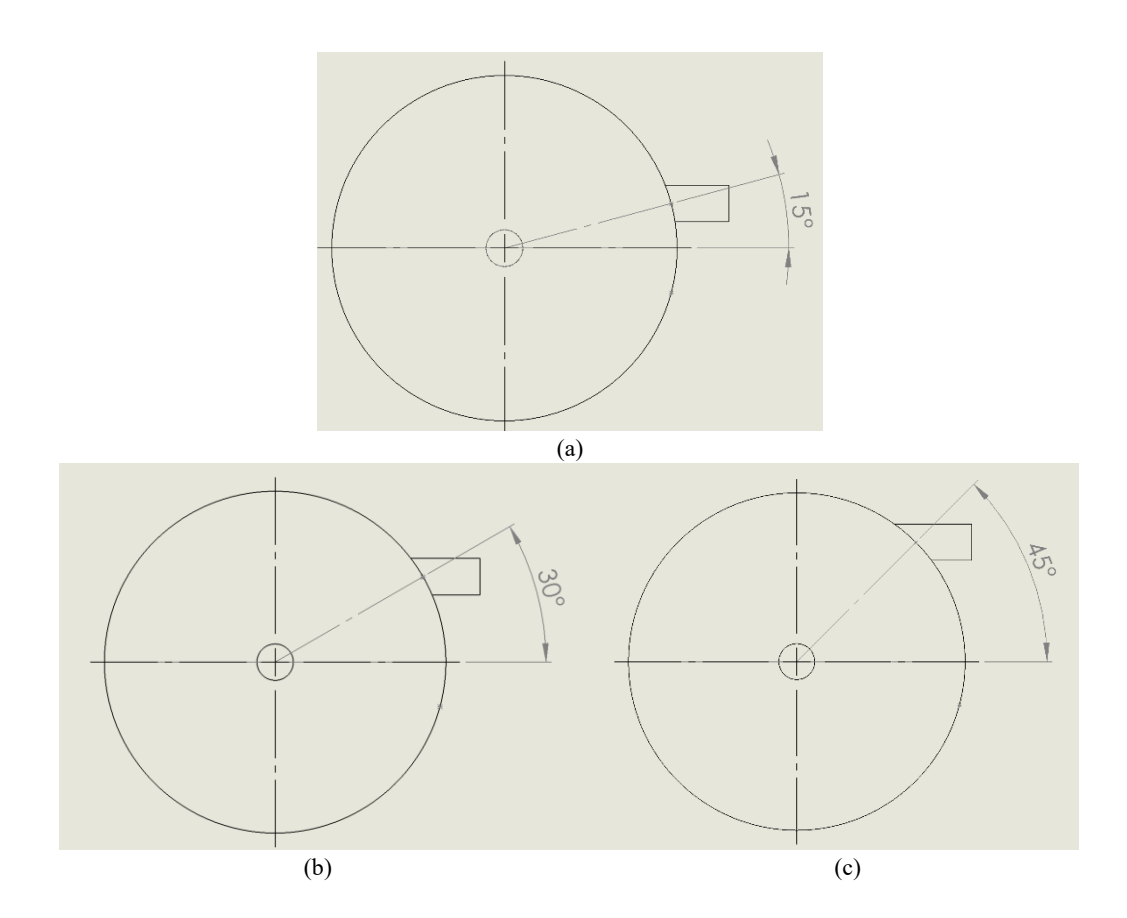


Figure 4.4 Geometrical Design of the Bubble Trap with inlet angulation (a) r30.0x53.0_inlet39.75_15deg, (b) r30.0x53.0_inlet39.75_30deg, (c) r30.0x53.0_inlet39.75_45deg.

All geometries used in this study were designed using **SolidWorks**®, based on a target internal volume of approximately **150 mL**, which was maintained across all variations. The models were subsequently exported for simulation, and the actual internal volume of each configuration was calculated from the CAD geometry. In the following table, the key design parameters of each tested geometry, such as the inlet height, the different angulations and the actual internal volume of each geometry, as calculated from the CAD model of each geometry are presented in the below Table:

Table 4:1 Geometrical Parameters of the Bubble Trap.

Geometry	Radius	Height	Inlet height	Inlet Degrees	Goal Volume	Model Volume
	r (mm)	h (mm)	h_inlet (mm)	inlet_deg (mm)	V (mL)	V (mL)
r30.0x53.0	30.00	53.00	26.5	0°	150	150.82
r30.0x53.0_inlet13.25	30.00	53.00	13.25	0°	150	150.82
r30.0x53.0_inlet39.75	30.00	53.00	39.75	0°	150	150.82
r30.0x53.0_inlet39.75_15deg	30.00	53.00	39.75	15°	150	150.82
r30.0x53.0_inlet39.75_30deg	30.00	53.00	39.75	30°	150	150.82
r30.0x53.0_inlet39.75_45deg	30.00	53.00	39.75	45°	150	150.82

4.1.2 Technical Specifications

The numerical setup of this study was established to reproduce physiological conditions representative of heart perfusion systems. Key parameters such as pressure, temperature, perfusate properties, flow rate, and inlet velocity were selected to ensure realistic simulation of the operational environment within the bubble trap. These parameters were determined based on clinically relevant values and are discussed in detail in the following sections.

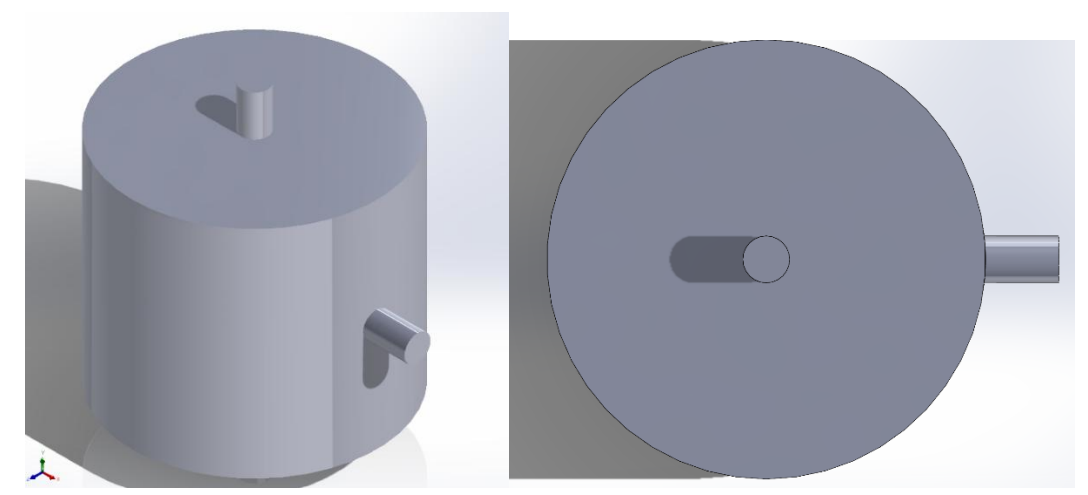


Figure 4.5 3D Model of the Bubble Trap of the Geometry r30.0×53.0.

The corresponding Technical Specifications are summarized in Table 4.2, and analyzed in the following Sections.

Table 4:2 Design Specifications of the Bubble Trap.

Parameter	Specification
Chamber Volume	150mL
Chamber Diameter	60mm
Chamber Height	53mm
Inlet/Outlet Diameter	6.4mm (1/4'')
Material	Medical-grade polycarbonate
Mean Pressure	80 mmHg
Flow Rate	750 mL/min
Temperature	37°C

4.1.2.1 Pressure

As the experiment of Elias Cyon [11] showed that the heart must contain a specific volume of serum to generate diastolic filling pressure, enabling the ventricle to eject fluid. In similar study by Kadipasaoglu et al, researchers utilized the Langendorff perfusion system for human hearts and maintained the perfusion pressure within the range of 80–100 mmHg to replicate physiological conditions and ensure optimal coronary perfusion [68]. Similarly, OCS systems maintain pressure of 75-80 mmHg

[69], [70], [71], [72]. Thus, the outlet pressure was chosen to be 80mmHg, to replicate normal conditions.

4.1.2.2 Temperature

Langendorff typically perfused at or near the normal body temperature of the species under investigation; generally, most researchers choose to perfuse their hearts at normal body temperature [1], [6], [73]. In similar studies the perfusion for a human heart was maintained at 37°C [68], [74], [75]. For this reason, all simulations in the present study were performed at a constant temperature of 37 °C to reflect physiologically relevant conditions. The preservation of temperature plays a significant role in perfusion as, according to Langendorff the heart rate elevates with rising temperature, to a peak that varied among individual hearts [11]. When the temperature exceeded the maximum, heart rate decreased significantly. The discrepancy suggests that each heart has a unique optimum temperature for effective pumping and the elasticity of the heart changes with temperature[11].

4.1.2.3 Perfusate

In order to simplify the simulation setup, the perfusate was assumed to have the thermophysical properties of water at $37\,^{\circ}\text{C}$, as the concentration of the triiodothyronine T3 in the perfusate is considerable low and equal to $39\mu\text{g/L}$ and therefore it was not expected to significantly influence the fluid's density or viscosity. The density and dynamic viscosity were set to $993.331\,\text{kg/m}^3$ and $0.69127\,\text{mPa·s}$, respectively values that correspond to those of water at $37\,^{\circ}\text{C}$. Similarly, experimental perfusates, such as Krebs–Henseleit solution, contain electrolytes and glucose, their overall composition is predominantly aqueous and their physical properties particularly viscosity and density, differ slightly from those of pure water [6], [68], [76], [77].

Table 4:3 Perfusate Properties at 37°C.

Properties	Values
Dynamic viscosity mPa s	0.69127
Density	993.331 kg/m³
Surface Tension of Water at 37°C	0.070396 N/m
Cp (Specific Heat)	4178.6 J/(kg K)
Thermal Conductivity	0.613

4.1.2.4 Flow Rate , Velocity and Reynolds Number

In ex vivo heart perfusion systems, such as the Organ Care System (OCS) developed by TransMedics, the coronary flow is typically maintained within the range of **700 to 800 mL/min** to ensure adequate oxygen and nutrient delivery to the myocardium under near-physiological conditions [69], [70], [71]. Accordingly, a flow rate of **750 mL/min** was selected in the present study to replicate realistic operating conditions in line with established perfusion practices.

The inlet velocity was calculated based on the volumetric flow rate and cross-sectional area of the inlet using the continuity equation:

Equation 4.1

$$Q = A \cdot u$$

Equation 4.2

$$A = \frac{\pi d^2}{4}$$

Where:

- Q: Volumetric flow rate (m³/s)
- A: Cross- sectional area (m²)
- u: Velocity (m/s)

From the Equations 4.1 and 4.2 given Q=750ml/min and an inlet diameter of d=6.4 mm, the inlet velocity was calculated as:

u = 0.38856 m/s

In order to characterize the flow regime at the inlet, the Reynolds number at the inlet was calculated using:

Equation 4.3

$$Re = \frac{\rho \cdot u \cdot D}{\mu}$$

Where:

- ρ: density (kg/m³)
- u: Velocity (m/s)
- D: diameter (m)
- μ: dynamic viscosity (Pa·s)

Given $\rho = 993 \text{kg/m}^3$, $\mu = 0.691 \times 10 - 3 \text{ Pa·s}$

Then:

The calculated Reynolds number at the inlet is 3573.44, based on a flow rate of 750 mL/min, an inlet diameter of 6.4 mm, and the physical properties of water at 37 °C. The intermediate range between the thresholds 2300 to 4000 corresponds to the transitional regime at the inlet.

4.2 Simulation Setup in ANSYS CFD

The discrete phase was modeled as spherical bubbles of $100 \mu m$, $200 \mu m$, $300 \mu m$, $400 \mu m$, and $500 \mu m$ in diameter, representing the typical range of microbubbles that may appear in perfusion system [31], [78]. These bubble groups were later injected into the continuous phase to evaluate the separation efficiency of the bubble trap [79].

4.2.1 Meshing

To ensure consistency and comparability between the different geometries, the same meshing methodology was applied across all geometrical configurations, resulting in a similar number of nodes and elements across the analyzed geometries (see Table 4:5). An unstructured tetrahedral mesh with a uniform element size of 1 mm was generated in ANSYS Meshing for the bubble trap as presented in the Figures 4.6. Similar researches according to bibliography have utilized unstructured mesh for DPM gasliquid problems [79].

The mesh cell size was selected in accordance with the recommendations provided in the ANSYS Fluent User Guide [80], which states that the particle or bubble diameter should be smaller than the characteristic size of the computational cell, ensuring accurate tracking of discrete phase trajectories without numerical instability or artificial particle—cell interactions. Based on this guideline, an unstructured mesh with an element size of 1 mm was applied, ensuring that even the largest injected bubbles (500 µm in diameter) remained smaller than the computational cells, in order to provide a balance between computational efficiency and the spatial resolution required to capture the hydrodynamic behavior of both the continuous and dispersed phases within the bubble trap.

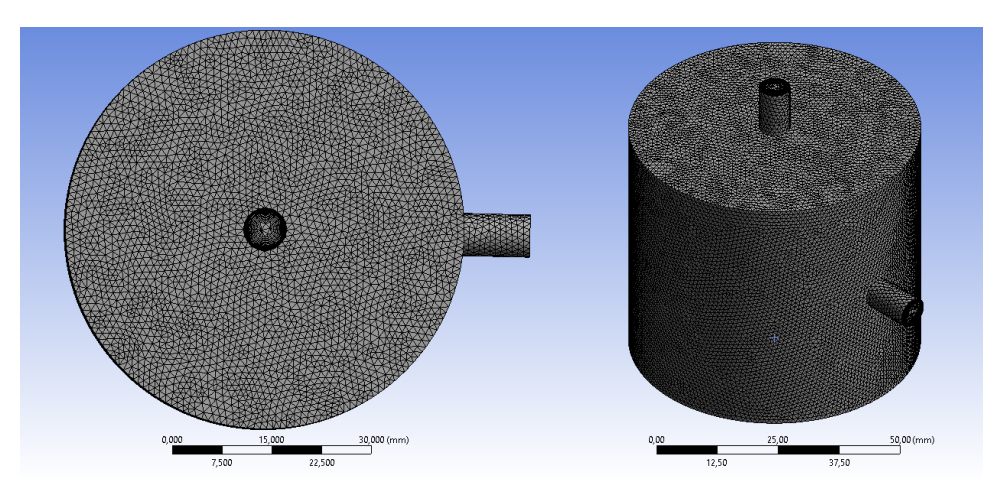


Figure 4.6 Generated Mesh of the Bubble Trap Geometry (r30.0×53.0)

In order resolve the near-wall region under the $k-\omega$ SST turbulence model that was used, 15 inflation layers were applied with a growth rate of 1.1, as the parameters determined after several trials to maintain $y^+<1$. The achieved y^+ values are summarized in Table 4:4.

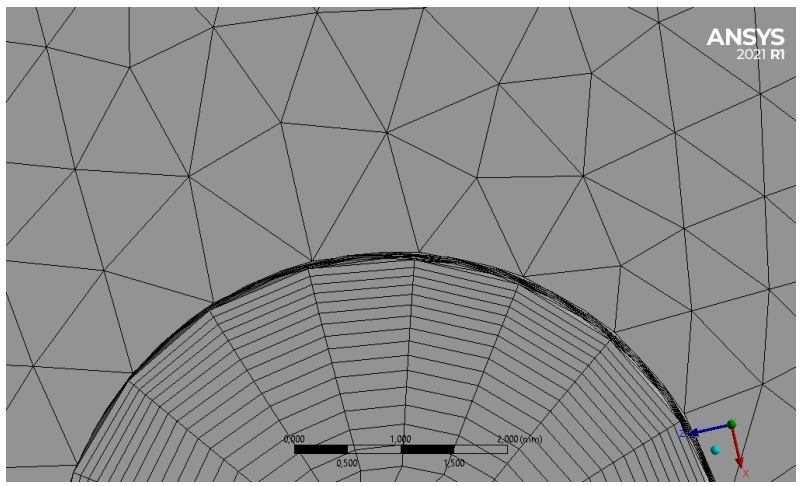


Figure 4.7 Inflation Layers Applied Near the Wall of Mesh.

Table 4:4 Calculated Y⁺ Values for the Bubble Trap Geometries

Geometry	Y ⁺
r30.0x53.0	0.53
r30.0x53.0_inlet13.25	0.48
r30.0x53.0_inlet39.75	0.47
r30.0x53.0_inlet39.75_15deg	0.47
r30.0x53.0_inlet39.75_30deg	0.54
r30.0x53.0_inlet39.75_45deg	0.62

Lastly, mesh quality was verified using standard metrics from ANSYS Meshing. All generated meshes satisfied the criteria about the minimum orthogonal quality, which should be greater than 0.1 and the maximum skewness, which should be below 0.9, according to Ansys User Guide. The number of nodes and elements for each geometry, along with aforementioned mesh quality metrics are presented in the below table:

Table 4:5 Summary of Mesh Quality Parameters and Element Statistics for each Geometry.

Geometry	Min Orthogonal Quality	Max Skewness	Nodes	Elements
r30.0x53.0	0.11152	0.88848	460167	1582537
r30.0x53.0_inlet13.25	0.12572	0.87428	459810	1580671
r30.0x53.0_inlet39.75	0.10889	0.89111	459998	1581189
r30.0x53.0_inlet39.75_15deg	0.12352	0.87648	459160	1579926
r30.0x53.0_inlet39.75_30deg	0.11015	0.88985	458960	1579383
r30.0x53.0 inlet39.75 45deg	0.11154	0.88232	460035	1582217

In the ANSYS Meshing also the named selections were created in order to define the boundaries that used in the simulations. The outlets were assigned as *outlet_bubbles* and *outlet_perfusate* and the inflow was assigned as *inlet*. The boundary definitions are illustrated in Figure 4.8, where they are labeled as A, B, and C, respectively.

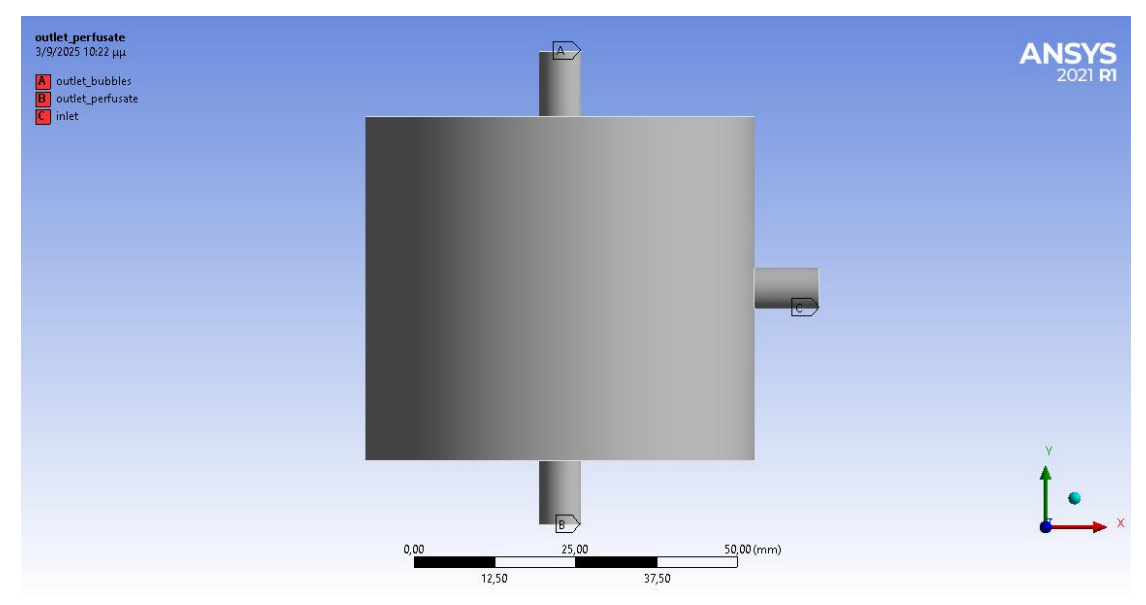


Figure 4.8: Boundary named selections: A) outlet bubbles, B) outlet perfusate, and C) inlet.

4.2.2 General Settings

Solver Type

A pressure-based solver was selected as the flow is incompressible and dominated by liquid and gas interaction without significant density changes due to pressure variations.

Time Dependency: A **transient simulation** was conducted as bubble behavior inside the trap changes with time. The transient approach allowed for observing the time evolution of the bubbles and the liquid-gas interface [80].

Gravity

The inclusion of gravitational acceleration is crucial in the simulation because bubble movement directly depends on gravitational effects as described in Section 3.2. For that reason, gravity was activated and set at -9.81 m/s².

$$g = -9.81 \text{m/s}^2$$

Turbulence Model

The Shear Stress Transport (SST) $k-\omega$ turbulence model was used to resolve the turbulent flow field within the bubble trap as it combines the robustness of the standard $k-\omega$ formulation near the walls with the free-stream independence of the $k-\varepsilon$ model in the bulk flow. It is particularly well-suited for internal flows with separation, recirculation, and adverse pressure gradients, all of which are expected in the bubble trap due to the sudden expansion, inlet jet, and swirling regions. Previous studies on have also demonstrated the effectiveness of the SST $k-\omega$ model in capturing flow structures relevant to bubble transport and removal [81], like bubble degassers [82] and perfusion systems [83]. In order to improve predictive accuracy in regions of complex geometry, the **curvature correction** and **corner flow correction** features were activated.

Materials

In the Materials setup, the fluid was defined as the *perfusate* as the properties described in the Section 4.1.2.3. The solid domain was assigned as *polycarbonate* with a density of 1200kg/m³, Cp=1220 J/(kg K) and Thermal Conductivity equal to 0.2 W/(mK), and the *inert particles* representing the air bubbles were defined with the corresponding physical properties as described in the below section.

4.3 Discrete Phase Model Setup

4.3.1 General DPM Set up

In generals DPM set up tab, the interaction with the continuous phase was enabled, meaning that momentum exchange between the bubbles and the perfusate was accounted for through two-way coupling. Also the unsteady particle tracking was used as bubble motion inside the trap is inherently time-dependent.

Since gravity was enabled in the simulation, buoyancy effects were automatically accounted for in the discrete phase model. In Physical models the Saffman lift force was activated to account for the lateral migration of bubbles in shear flows like similar studies, which can influence their trajectories in regions of velocity gradients [61]. Without this effect, bubbles would be influenced only by drag and buoyancy, which could underestimate their lateral migration across streamlines [61]. Bubble–bubble collision modeling and break up were not included, as the objective of this study was to examine bubble transport and trapping behavior without the added complexity of coalescence or breakup phenomena. Brownian motion and thermophoresis were neglected.

4.3.2 Injections

In order to assess the performance of the bubble trap, a controlled injection of air bubbles was performed during the simulation. In accordance with the approach adopted in similar computational studies, the bubbles were modeled as spherical discrete phase particles with constant diameter and uniform material properties [78]. A total of 1500 air bubbles were introduced at the initial time step of the simulation (t = 0.0001s) using. The injection consisted of six distinct bubble size groups, each comprising 250 bubbles, with diameters of 50 μ m, 100 μ m, 200 μ m, 300 μ m, 400 μ m, and 500 μ m, respectively.

The injection position was defined at the inlet boundary of the domain, where in order to avoid direct wall interaction, the bubbles were positioned 2 mm away from the inlet wall and distributed within a stagger radius of 1 mm around the injection centerline.

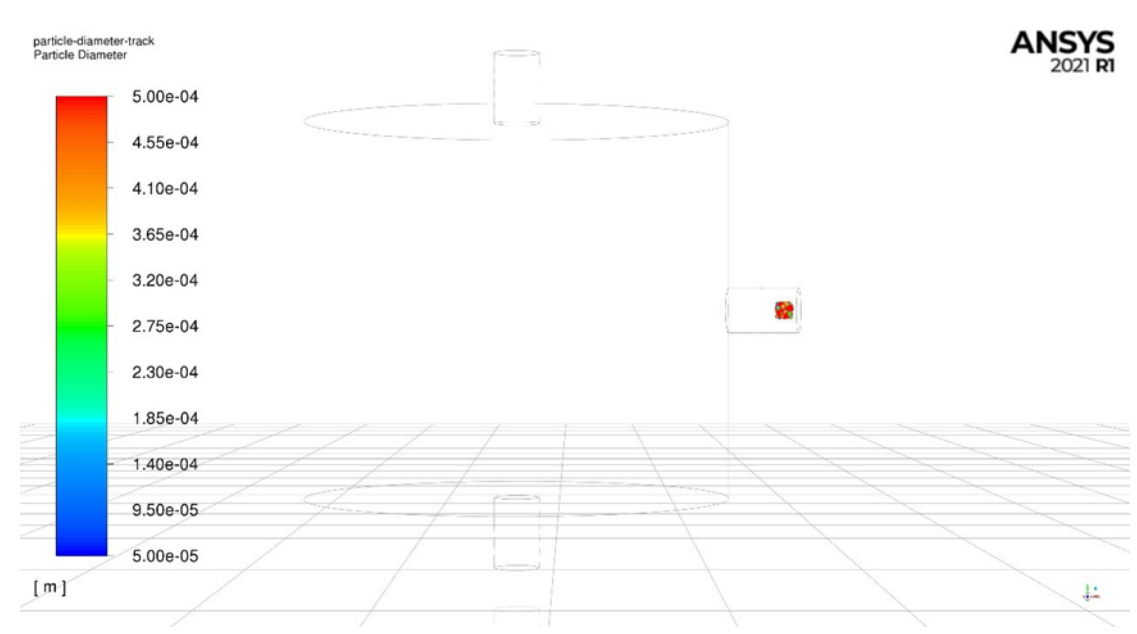


Figure 4.9 Group of bubbles injections at the inlet within a stagger radius of 1mm (front view).

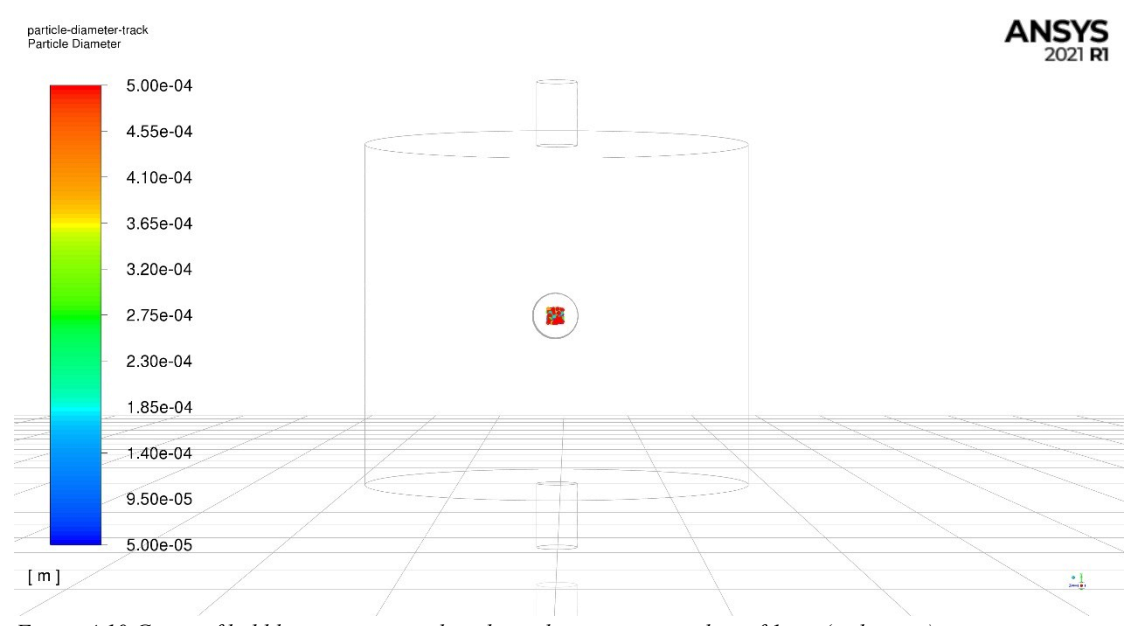


Figure 4.10 Group of bubbles injections at the inlet within a stagger radius of 1mm (right view).

The Volume of each bubble was calculated given the below equations, for the different diamters [56]:

Equation 4.4

$$V_{bubble} = \frac{4}{3} \pi \left(\frac{d}{2}\right)^3$$

Equation 4.5

$$m_{bubble} = \rho_{air} \cdot V_{bubble}$$

Where:

• V_{bubble}: volume of a single bubble [m³]

• M_{bubbles}: mass of a single bubble [kg]

• d: bubble diameter [m]

• ρ_{air} : air density at 37°C equal to 1.138 kg/m³

Table 4:6 summarizes the volume and mass of each bubble and the mass per size group and the sum of 250 bubbles, for each size group.

Table 4:6 Injected Bubble Characteristics for the Discrete Phase Model (DPM) Simulation.

Bubble Diameter (µm)	Number of bubbles injected	Volume per bubble (m³)	Mass per bubble (kg)	Mass of 250 bubbles (kg)
50	250	6.54E-14	7.45E-14	1.86E-11
100	250	5.24E-13	5.96E-13	1.49E-10
200	250	4.19E-12	4.77E-12	1.19E-09
300	250	1.41E-11	1.61E-11	4.02E-09
400	250	3.35E-11	3.81E-11	9.53E-09
500	250	6.54E-11	7.45E-11	1.86E-08

Then, the total mass of air injected into the system was calculated based on the number and size distribution of the discrete air bubbles. Assuming spherical geometry and a constant air density of ρ_{air} =1.138 m³ at 37 °C, the volume of air corresponding to the total mass was computed using the fundamental relationship [56]:

Equation 4.6

$$V = \frac{m}{\rho}$$

Where:

• **V**: total air volume [m³]

• **m**: total air mass [kg]

• ρ : Air density = 1.138 kg/m³ at 37 °C

Then:

Table 4:7 Total Injected Bubble Mass and Volume in the DPM Simulation.

Number of bubbles injected	1500
Total Mass of bubbles [kg]	3.35E-08
Total Mass of bubbles [μg]	33.54
Total Volume of air injected [μL]	29.47

The corresponding mass of each bubble group as calculated above and presented in the Table 4:6, were set for each injection and the temperature of all bubble groups was set to 37 °C (310.15 K). No explicit injection velocity was set as the bubbles were allowed to move with the continuous phase velocity at the inlet, based in bibliography [84] and reflecting the physical scenario in which entrained air is carried into the system by the perfusate flow without any additional imposed momentum.

Lastly, the Grace drag law was selected as the drag model, as it is suitable for spherical bubbles in liquid media [80] and to represent the influence of turbulence on bubble trajectories, stochastic tracking was enabled through the Discrete Random Walk (DRW) model. In that way, bubble motion is influenced by instantaneous turbulent velocity fluctuations superimposed on the mean flow[80]. The random eddy lifetime option was applied, which assumes that bubbles remain within a turbulent eddy for a characteristic eddy lifetime before interacting with a new eddy [51].

4.4 Boundary Conditions

4.4.1 Inlet

At the inlet, a velocity boundary condition was applied with a value of **0.38856 m/s**, as calculated in the Section 4.1.2.4, given Q=750ml/min. The turbulence specification method was set to *intensity and hydraulic diameter*, with a turbulence intensity of 3%, which is common for pipes according to Ansys Guide and a hydraulic diameter of 6.4mm, corresponding to the inlet diameter as obtained from the relation Dh=D, based on the following equation:

Equation 4.7

$$D_h = \frac{4(\frac{\pi D^2}{4})}{\pi D} = D$$

Where:

• **D:** the diameter of the circular tube

The temperature of the continuous phase (perfusate) at the inlet was fixed at 37 °C (310.15 K) in order to represent physiological conditions as described in previous Section 4.1.2.2. For the discrete phase, the inlet boundary was defined with the *reflect* option, which means that the bubbles that interacting with the inlet were reflected back into the flow domain rather than escaping.

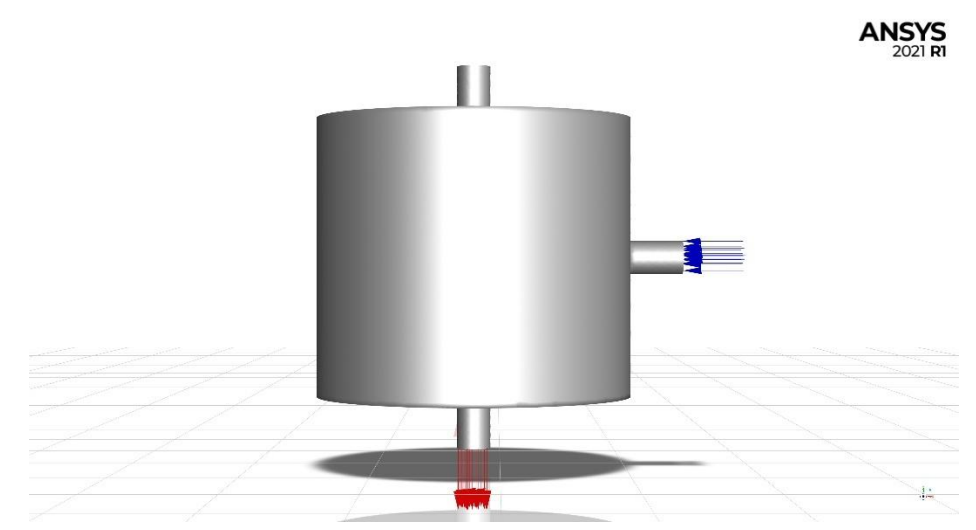


Figure 4.11 Boundary Conditions Setup. The blue arrows represent the inlet, where the perfusate enters the chamber, and the red arrows indicate the outlet, where the flow exits the system.

4.4.2 **Outlet**

The outlet of each geometry was defined as a pressure outlet with a fixed pressure of 80 mmHg (10665.791 Pa) and the turbulence specification method was set to *intensity* and hydraulic diameter, with a turbulence intensity of 3% and a hydraulic diameter of 6.4mm, corresponding to the outlet diameter based on the Equation 4.7. For the discrete phase, the boundary condition was set to **escape**, allowing bubbles that reached the outlet to leave the domain.

4.4.3 Walls

The walls of the bubble trap were set as stationary walls with a no-slip condition applied to the continuous phase in order for velocity to be zero at the solid boundaries. For the thermal boundary condition, convection was applied to represent heat transfer between the housing and the environment. The material properties corresponding to polycarbonate were used, with a heat transfer coefficient of 10 W/m²·K and a free-stream temperature of 25 °C, representative of standard laboratory conditions. Lastly for the discrete phase, the wall boundary condition was set to *reflect*, meaning that when bubbles met with the housing walls were reflected.

4.5 Simulation Procedure

For improved convergence according to Ansys Theory Guide for multiphase flows, the Coupled scheme was selected in terms of the pressure-velocity coupling, meaning that the momentum and continuity equations were solved simultaneously. Gradients were calculated using the Least Squares Cell-Based and for the pressure interpolation, the PRESTO! method was applied, which recommended for flows involving gravity. For the momentum, turbulent kinetic energy, specific dissipation rate, and energy equations, the *Second-Order Upwind* scheme was applied. The discretization schemes and solution methods applied in the simulations are summarized in Table 4:8.

Table 4:8 Summary of Solver Coupling and Discretization Schemes.

Scheme	Coupled
Gradient	Least Square Cell Based
Pressure	PRESTO!
Momentum	Second Order Upwind
Turbulent Kinetic Energy	Second Order Upwind
Specific Dissipation Rate	Second Order Upwind
Energy	Second Order Upwind

The solution was initialized using the standard initialization method in ANSYS Fluent, with values computed from all cell zones. After several trials a fixed time step size of 0.0001s, leading to converge. The simulation was run for a total of 40,000 time steps with a 20 iterations/time step, corresponding to a flow time of 4s, where during this period it was observed that bubbles began to escape from the trap and reached a stabilized behavior.

Several report definitions were created in order to monitor both the continuous and discrete phase behavior during the simulations. For the discrete phase, the injected mass of air through the inlet, which corresponds to bubbles that were injected and the escaped mass of air through the outlet, which corresponds to bubbles that were escaped recorded.. In addition, surface report definitions were applied at both the inlet and the outlet boundaries to record pressure, velocity, and temperature.

Table 4:9 CFD Model Settings

Solver Type	Pressure-based		
Time Dependency	Transient Simulation		
Gravity	Activated		
Energy Equation	On		
Interaction with the Continuous Phase	On		
DPM	On		
Wall	No slip		

The residuals for continuity, momentum, and turbulence equations (k and ω) were set to 1×10^{-3} and the energy equation was assigned with a criterion of 1×10^{-6} to ensure accurate thermal resolution. Convergence was also confirmed by monitoring stabilized mass flow rates and the steady trend of bubble trajectories during the transient simulation. More specifically, as part of the numerical validation, the mass flow rate fluxes at the inlet and outlet were compared, where the relative difference between inlet and outlet fluxes was found to be below 10^{-8} % (see Table 4:10), indicating that mass conservation was preserved throughout the simulations [85].

4 Methodology

Table 4:10 Mass Flow Rate Flux Difference Between Inlet and Outlet for Each Geometry.

Mass Flow Rate Flux Difference Inlet/Outlet

r30.0x53.0	2.27E-09
r30.0x53.0_inlet13.25	5.19E-09
r30.0x53.0_inlet39.75	5.13E-08
r30.0x53.0_inlet39.75_15deg	1.89E-09
r30.0x53.0_inlet39.75_30deg	2.69E-09
r30.0x53.0_inlet39.75_45deg	1.53E-08

5 Results and Discussion

5.1 Efficiency

The efficiency of each geometry was calculated based on the Equation 3.24, and for the ejected bubbles it can be transformed as:

$$n(\%) = \frac{Number\ of\ bubbles\ retainded\ within\ the\ system}{Total\ number\ of\ bubbles\ injected} \times 100$$

As already mentioned, for each geometry a group of 1500 bubbles was injected consisting of a group of 250 bubbles with a diameter of $50\mu m$, $100 \mu m$, $200 \mu m$, $300 \mu m$, $400 \mu m$, and $500 \mu m$, respectively, with a constant total injected air mass of $3.35 \ 10^{-8}$ kg. The below Table summarizes the injected/escaped air mass, the number of bubbles that are injected/escaped and the calculated efficiency for each geometry.

Table 5:1 Summary of Injected and Escaped Air Mass, Bubble Count, and Bubble Trapping Efficiency for Each Bubble Trap Geometry.

Geometry	Injected Air Mass [Kg]	Escaped Air Mass Escaped [Kg]	Bubbles Injected	Bubbles Remained	Bubbles Escaped	Efficiency [%]
r30.0x53.0	3.35E-08	2.20E-11	1500	1408	92	93.87
r30.0x53.0_inlet13.25	3.35E-08	3.81E-11	1500	1400	100	93.33
r30.0x53.0_inlet39.75	3.35E-08	8.34E-12	1500	1444	56	96.27
r30.0x53.0_inlet39.75_15deg	3.35E-08	7.15E-12	1500	1460	40	97.33
r30.0x53.0_inlet39.75_30deg	3.35E-08	5.36E-12	1500	1463	37	97.53
r30.0x53.0_inlet39.75_45deg	3.35E-08	6.70E-13	1500	1491	9	99.40

The effect of inlet height on bubble trap efficiency was examined in the first stage of the study. It was observed in all geometries that bubble escape was strongly size-dependent, with highest number of escaped bubbles belonging to the smallest size groups (50 μ m and 100 μ m), while the bubbles that were 200 μ m were almost entirely retained and escaped only in geometries r30.0x53.0 and r30.0x53.0_inlet13.25 and bubbles of 300 μ m escaped only in geometry r30.0x53.0_inlet13.25 with the low inlet. Larger bubbles larger than 300 μ m, were entirely retained within the system, in all different configurations (see Table 5:2). The results reflect clinical practice, where microbubbles escape easier from bubble trapping systems rather than larger bubbles [86], [87].

Also, it was noted that, when the inlet was placed closer to the perfusate outlet (r30.0x53.0_inlet13.25), the number of escaping small bubbles increased, leading to a reduction in efficiency to 93.33% compared to the baseline geometry r30.0x53.0, which presented an efficiency equal to 93.87%. On the other hand, when positioning the inlet higher in the chamber the retention of bubbles improved, reducing the escape of smaller bubbles and leading to the highest efficiency among the tested inlet heights, which is equal to 96.27%. Based upon this optimal configuration, the second stage of

the analysis investigated the influence of inlet angulation, by progressive tilting of the inlet from 15° to 45° produced incremental improvements in performance. Then the efficiency is progressively increased, as in 15° inlet angulation the geometry presented an efficiency of 97.33%, the 30° inlet angulation presented an efficiency of 97.53% and the geometry with a 45° inlet angulation presented the highest efficiency reaching to 99.40%, where a few of the smallest bubbles ($50\mu m$) escaped. The results of each geometry are presented in the table below and the findings of each geometry are analyzed in the next sections.

Table 5:2 Escaped Bubbles by Bubble's Diameter and Corresponding Bubble Trapping Efficiency for Inlet Height and Angulation.

Escaped Bubbles							
Bubble Size [μm]	r30.0x53.0	r30.0x53.0 _inlet13.25	r30.0x53.0 _inlet39.75	r30.0x53.0 _inlet39.75 _15deg	r30.0x53.0 _inlet39.75 _30deg	r30.0x53.0 _inlet39.75 _45deg	
50	71	79	48	32	32	9	
100	20	19	8	8	5	0	
200	1	1	0	0	0	0	
300	0	1	0	0	0	0	
400	0	0	0	0	0	0	
500	0	0	0	0	0	0	
Total	92	100	56	40	37	9	
Trapping Efficiency [%]	93.87	93.33	96.27	97.33	97.53	99.40	

As it is observed, among all tested configurations, the geometry r30.0x53.0_inlet39.75_45deg has the highest efficiency, achieving 99.40% bubble retention with nine of the 1500 injected bubbles escaping. This can be explained by the combined influence of inlet height and angulation. Placing the inlet at a highest position of the chamber, far from the outlet, increases bubble residence time, allowing larger bubbles to rise toward the top of the chamber, while the 45° inlet angulation promotes recirculating flow patterns that slow down bubble transport and prevent the direct escape through the outlet. The bar chart below illustrates the number of escaped bubbles per diameter group at all different inlet configurations.

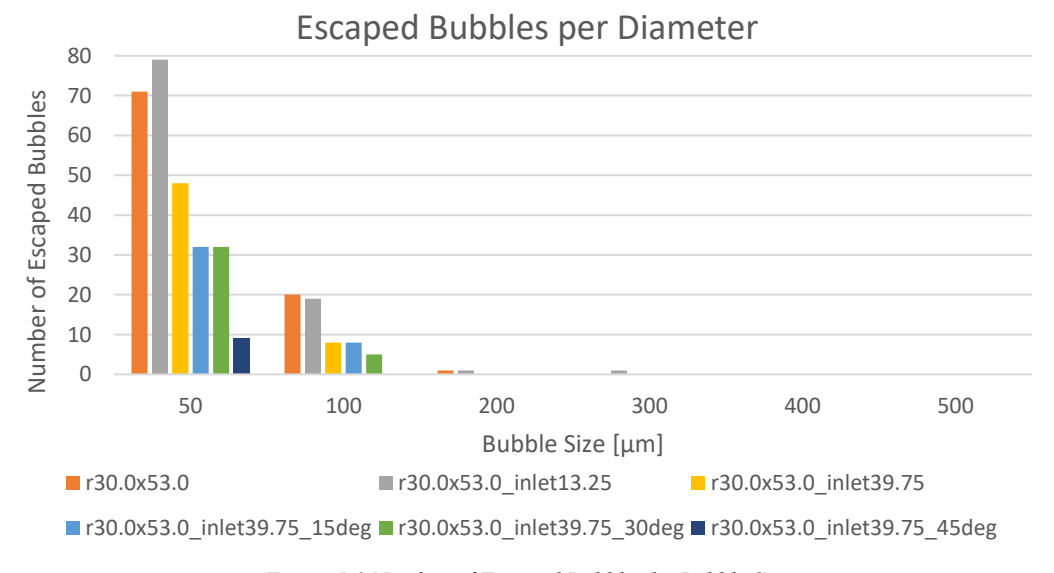


Figure 5.1 Number of Escaped Bubbles by Bubble Size

5.1.1 Inlet Height Variation

To begin with, the effect of inlet height on bubble trap performance was evaluated. The two configurations r30.0x53.0_inlet13.25 and r30.0x53.0_inlet39.75, were tested in addition to the baseline geometry r30.0x53.0. Results showed that the initial geometry had an efficiency of 93.87%, with 92 bubbles escaping out of 1500 injected, the lower inlet position (13.25 mm) reduced efficiency to 93.33%, with 100 bubbles escaping, while the upper inlet position (39.75 mm) improved efficiency to 96.27%, with 56 bubbles escaping. Therefore, inlet height has a direct impact on bubble escape behavior and trapping efficiency, as when placing the inlet at a higher position led to 2.94% increase in trapping efficiency and an upward trend can be observed in the plot of Trapping efficiency vs Inlet Height (Figure 5.2), as the inlet height increases, the trapping efficiency also improves.

96.5 Trapping Efficiency [%] 96 95.5 95 94.5 94 93.5 93 0 10 20 30 40 50 Inlet Height (mm)

Inlet Height - Bubble Trapping Efficiency

Figure 5.2 Inlet Height vs. Bubble Trapping Efficiency

As it can be observed from the Figures 5.3 (a)-(c), smaller bubbles tended to accumulate near the bottom of the chamber and follow the main flow path toward the outlet, whereas larger bubbles were located toward the upper regions of the chamber closer to the inlet. This can be attributed to buoyancy effects, as larger bubbles tend to accumulate at the top of the chamber primarily due to their higher buoyancy force relative to the drag force from the surrounding fluid. More specifically, the buoyancy force F_B acting on a bubble is proportional to its volume (Equation 3.12), while the drag force F_D (Equation 3.13), is proportional to the bubble's surface area and velocity. Because buoyancy increases with the cube of the bubble radius R^3 , larger bubbles experience a stronger upward force and rise more rapidly through the fluid and this causes them to separate and collect near the upper surface of the chamber.

In contrast, smaller bubbles (e.g., 50–100 µm) have lower buoyancy forces, can easily carried along the streamlines toward the outlet and exhibit a greater tendency to escape the system, especially in geometries where the jet is more direct and recirculation zones are weaker. This behavior is consistent with bibliographic findings and clinical observations, where microbubbles are known to persist despite bubble trap mechanisms, while larger bubbles are more efficiently captured [86], [87].

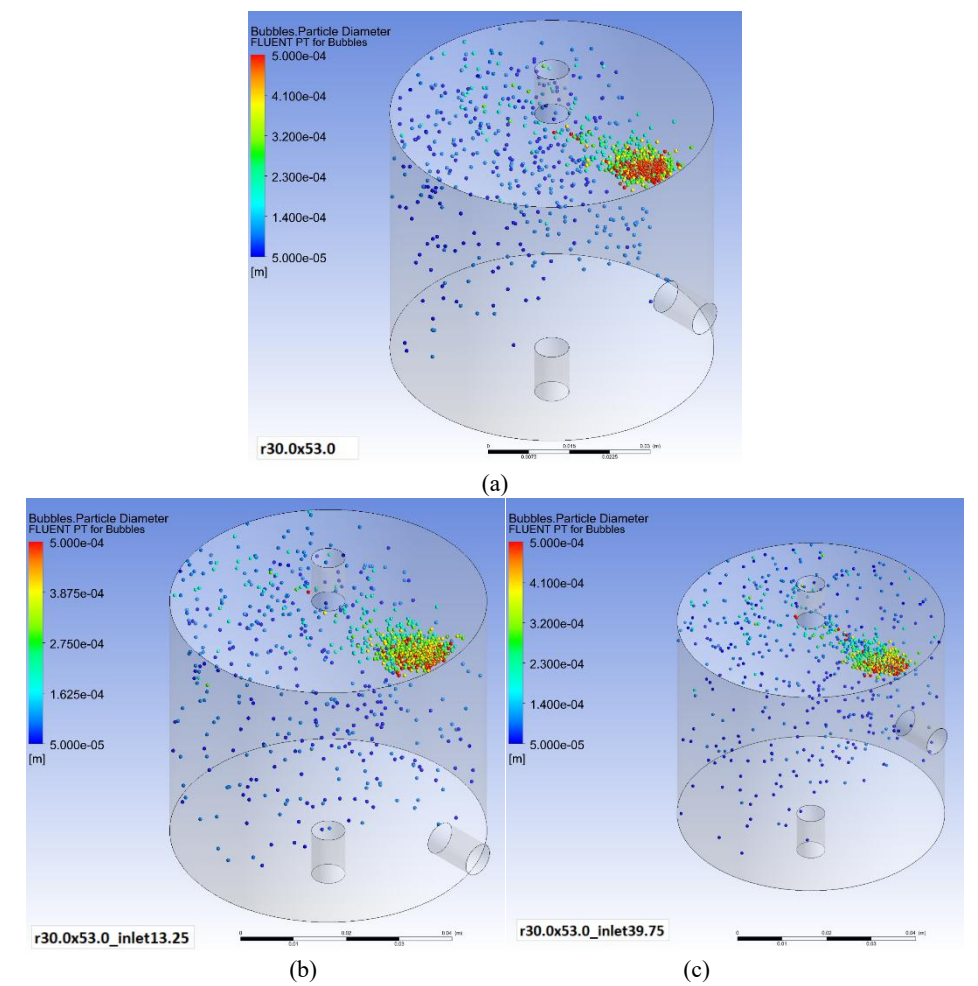


Figure 5.3 Spatial Distribution of Bubbles with Different Size in the Geometries of Different Inlet Height (a) r30.0x53.0 (b) r30.0x53.0 inlet13.25 (c) r30.0x53.0 inlet39.75, after the 4s simulation.

5.1.2 Inlet Angle Variation

In continuous, the effect of inlet angulation was evaluated for the geometry with the inlet placed at three-quarters of the chamber height (39.75 mm), which had already demonstrated higher efficiency compared to the baseline geometry and the geometry of low inlet configuration. At 15°, the number of escaped bubbles decreased to 40, achieving an efficiency of 97.33%, while at 30° it further reduced to 37 with an efficiency of 97.53%. The best performance was achieved at 45°, where 9 bubbles escaped, corresponding to an efficiency of 99.40%. When angulation was introduced the efficiency progressively increased, compared to the geometry with the highest performance (r30.0x53.0_inlet39.75) among inlet height configurations by 1.06%, 1.26% and 3.13% for the 15°, 30°, and 45° inlet angulations, respectively. As the angulation increases, the jet is redirected toward the chamber walls, creating stronger recirculation zones and promoting longer bubble retention within the chamber and this enhanced mixing effect allows more bubbles to rise and be trapped before reaching the outlet. The plot of Inlet Angulations vs. Bubble Trapping Efficiency in the Figure 5.4 illustrates the relationship between inlet angulation and bubble trapping efficiency,

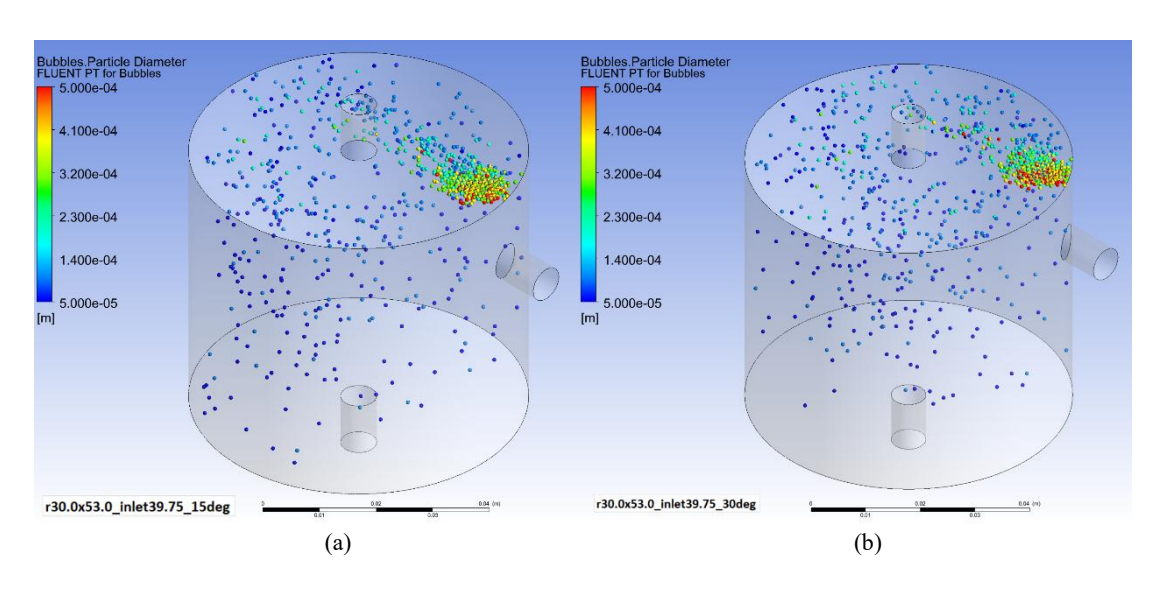
showing a positive correlation between the two parameters, as the inlet angulation increases from 15° to 45°, the trapping efficiency rises steadily.

100 99.5 20 99.5 20 99.5 20 98.5 98 98.5 97 0 10 20 30 40 50 Inlet Angulation [°]

Inlet Angulation - Bubble Trapping Efficiency

Figure 5.4 Inlet Angulations vs. Bubble Trapping Efficiency

Similarly with the inlet height configurations, in all geometries with the different angulations, a pattern can be observed, as larger bubbles (colored red to yellow, 300–500 μm) accumulate and remain concentrated near the top region of the chamber, while smaller bubbles (blue to green, 50–200 μm) follow the flow path and are distributed in the chamber. As the inlet angulation increases, the jet flow is redirected along the chamber wall, inducing a stronger counterclockwise recirculation pattern and this enhances bubble retention, as the flow circulation helps redirect small bubbles away from the outlet and toward the upper region where buoyancy dominates.



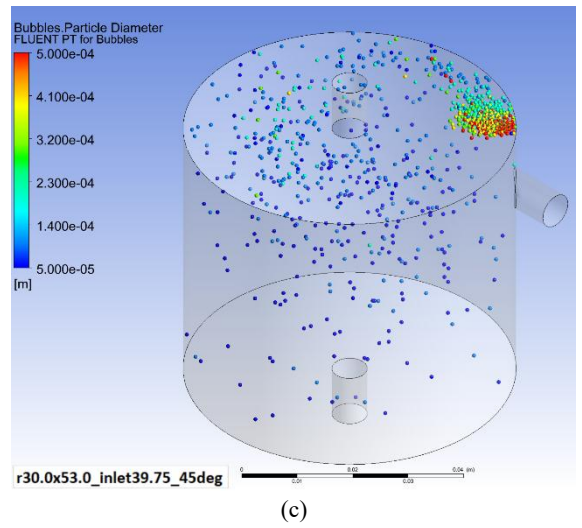
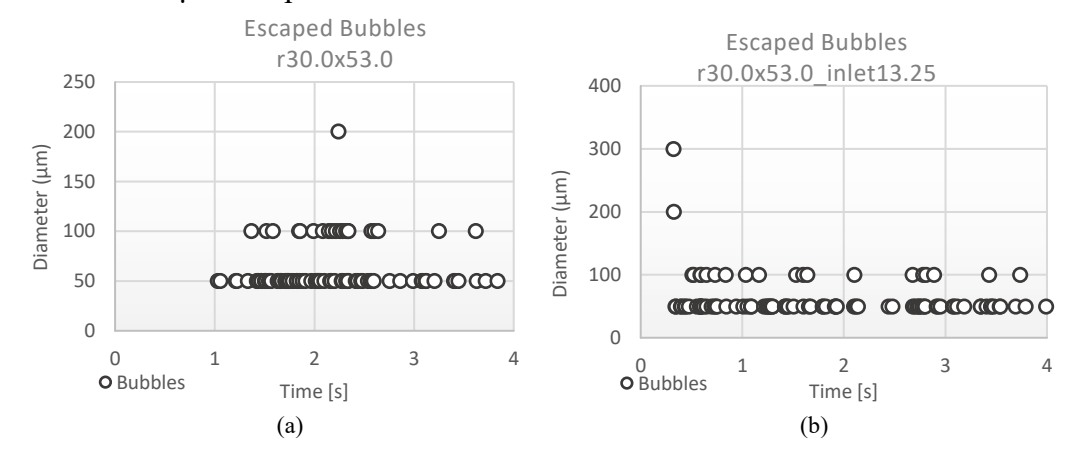


Figure 5.5 Spatial Distribution of Bubbles with Different Size in the Geometries of Different Inlet Angulation (a) r30.0x53.0_inlet39.75_15deg (b) r30.0x53.0_inlet39.75_30deg (c) r30.0x53.0_inlet39.75_45deg , after the 4s simulation.

5.1.3 Bubbles escaping over time

In the following figures the time at which the first bubbles escaped and how bubbles escaping through time, for each geometry can be observed, providing insight into how inlet position and angulation influence bubble residence time and early escape behavior. In the low inlet case (Figure 5.6b), the first bubbles escaped early in the beginning of the simulation, with more than 30 bubbles exiting by 1s and a sharp release between 2-3s, meaning that positioning the inlet closer to the outlet provides a direct path for bubbles to leave the chamber with low residence time. Also, lager bubbles of $100\mu m$ and one of $200\mu m$ escaped before 1s.



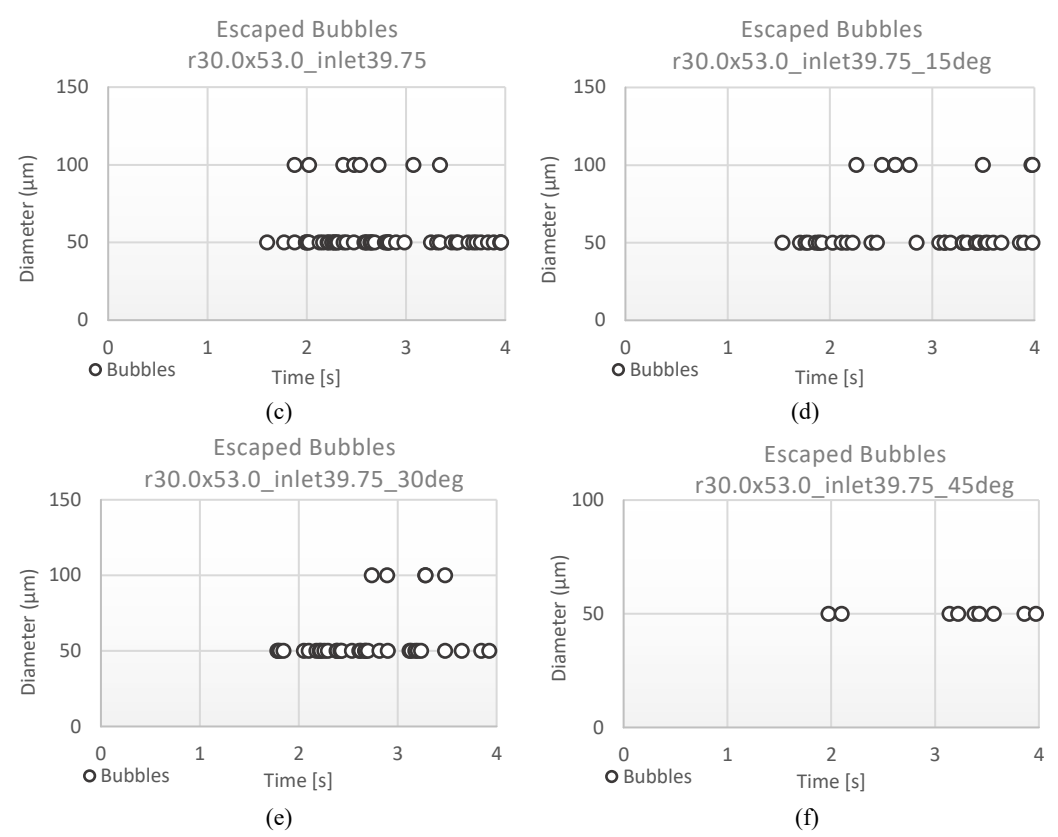


Figure 5.6 Plots of Escaped Bubbles over Time (a) r30.0x53.0 (b) r30.0x53.0 inlet13.25 (c) r30.0x53.0 inlet39.75 (d) r30.0x53.0 inlet39.75 15deg (e) r30.0x53.0 inlet39.75 30deg (f) r30.0x53.0 inlet39.75 45deg

The baseline geometry (Figure 5.6a) also demonstrated early bubble release, where no bubbles escaped during the first second, but a large release occurred at 2–3s (40 and 39 bubbles, respectively), showing that while some recirculation delayed bubble transport, the central velocity jet still carried many bubbles to the outlet. By placing the inlet higher (Figure 5.6c), the number of bubbles that escaped by the 2s, reduced to 6 bubbles and a higher number of bubbes that escaped can be observed during the 3s, like most geometries. When the inlet was positioned higher and combined with angulation (Figures 5.6 (d)-(f)), the escape of bubbles was delayed and their overall number was reduced. The Table 5:3 summarizes the escaped bubbles over time.

Table 5:3 Number of Escaped Bubbles over time for all geometries, along with the corresponding Bubble Trapping Efficiency.

Number of Escaped Bubbles							
Time [s]	r30.0x53.0	r30.0x53.0_ inlet13.25	r30.0x53.0_ inlet39.75	r30.0x53.0_ inlet39.75_ 15deg	r30.0x53.0_ inlet39.75_ 30deg	r30.0x53.0_ inlet39.75_ 45deg	
1	0	30	0	0	0	0	
2	40	32	6	8	4	1	
3	39	21	33	12	21	1	
4	13	17	17	20	12	7	
Total	92	100	56	40	37	9	
Trapping Efficiency [%]	93.87	93.33	96.27	97.33	97.53	99.40	

For the 15° inlet geometry (Figure 5.6d), bubble escape began before 2s with 8 bubbles, followed by a moderate release of 12 bubbles at 3s, and a more substantial release of 20 bubbles at 4s, leading to a total of 40 escaped bubbles. In the case of the 30° inlet geometry (Figure 5.6e), bubble escape was slightly more delayed and more evenly distributed across time. Only 4 bubbles escaped at 2s, followed by 21 at 3s, and 12 at 4s, for a total of 37 bubbles, meaning that bubbles were retained longer within the chamber compared to the baseline and low-inlet cases. Finally, the 45° inlet geometry (Figure 5.6f), exhibited the latest and lowest bubble release, with most bubbles retained within the chamber until the end of the simulation, as a single bubble escaped at 2s and another at 3s, while the majority (7 bubbles) escaped at 4s. The results of each simulation, regarding the number of bubbles with the corresponding bubbles size that escaped over time, are presented in Appendix A and the plots in Appendix E can show the correlation of bubble size and the number that escaped over time, as described above.

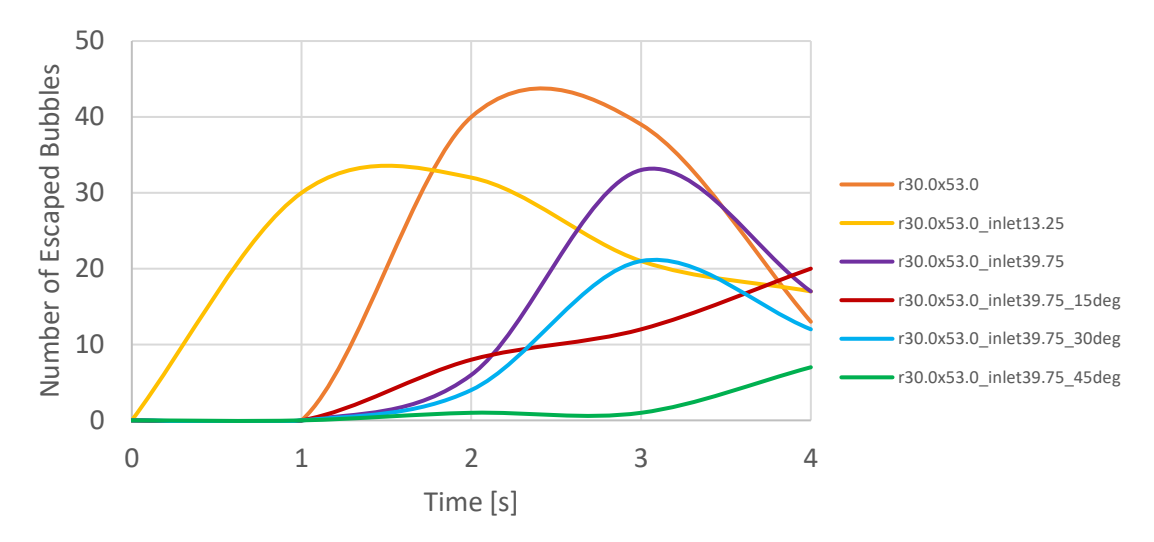


Figure 5.7 Time Evolution of Bubble Escape for the Different Inlet Configurations.

Furthermore, from the Figure 5.7 it can be observed that the low-inlet geometry (r30.0x53.0_inlet13.25) and the baseline configuration (r30.0x53.0) exhibit a steep and early rise in escaped bubbles, with sharp peaks around 2–3 s, indicating that most bubbles exited the system rapidly. In contrast, the geometries with higher inlet positioning and angular orientation (r30.0x53.0_inlet39.75, _15°, _30°, and _45°) display delayed and broader peaks, indicating that bubble escape occurred more gradually and over a longer time, leading to an enhanced recirculation and mixing inside the chamber and allowing bubbles to remain suspended longer before reaching the outlet. Furthermore, the lower amplitude of these peaks confirms a smaller total number of escaped bubbles, reflecting a more efficient separation process. Among all tested geometries, the 45° angled high-inlet configuration achieved the best performance, with the smallest and latest peak, demonstrating that this orientation most effectively, by promoting bubble retention through recirculating flow structures. Figure 5.8 illustrates the distribution of bubble escape for all tested geometries.

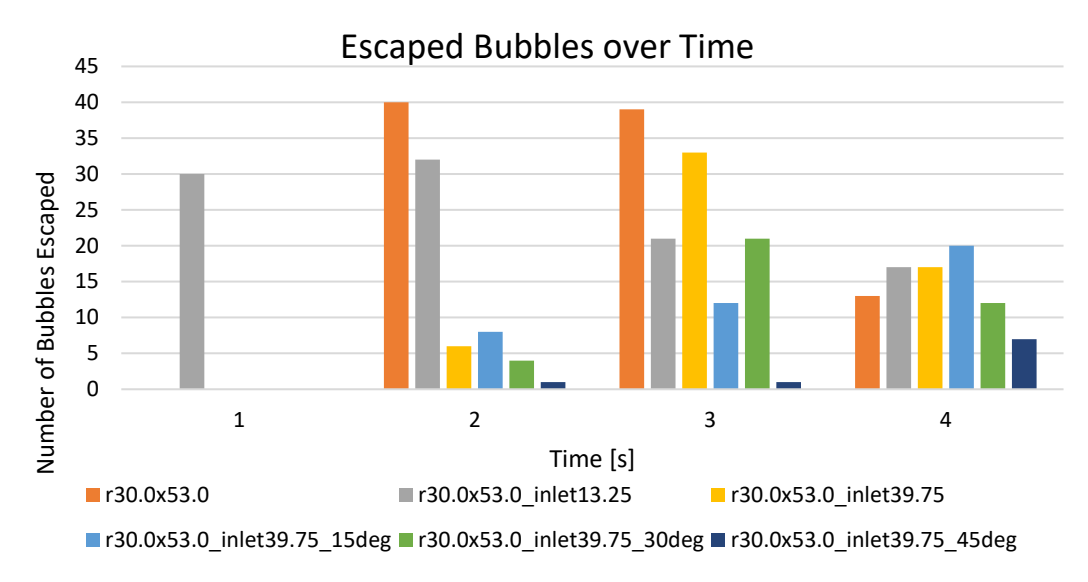


Figure 5.8 Number of Escaped Bubbles over time across the different geometries

5.2 Pressure

The mean inlet static pressure remained stable across all geometries at approximately 81.25-81.28 mmHg, with variations of $\pm 0.02-0.03$ mmHg and the corresponding mean pressure drop was ranging from 1.25 to 1.28 mmHg (see Table 5:4).

Table 5:4 Mean Inlet Static Pressure and Pressure Drop in the different geometries.

	Mean P _{inlet} [mmHg] ±Std	ΔP Mean [mmHg] ±Std
r30.0x53.0	81.25 ± 0.03	1.25 ± 0.03
r30.0x53.0_inlet13.25	81.28 ± 0.02	$1.28 \pm \ 0.02$
r30.0x53.0_inlet39.75	81.28 ± 0.02	1.28 ± 0.02
r30.0x53.0_inlet39.75_15deg	81.27 ± 0.02	$1.27 \pm \ 0.02$
r30.0x53.0_inlet39.75_30deg	81.26 ± 0.02	1.26 ± 0.02
r30.0x53.0 inlet39.75 45deg	81.27 ± 0.03	1.27 ± 0.03

Among all the tested geometrical configurations, the geometry with the inlet at the middle of the chamber (r30.0x53.0) presented the lowest pressure drop equal to 1.25mmHg, the configurations of low/high height presented pressure drop equal to 1.28mmHg and the geometries with angulation of 15°,30°,45° presented a pressure drop of 1.27 mmHg,1.26 mmHg and 1.27 mmHg, respectively. The expected pressure drop drives the flow through the bubble trap and ensures continuous perfusate circulation from inlet to outlet, leading to higher inlet pressure than the outlet as anticipated and it is caused by wall friction, viscous losses and local flow resistance within the chamber. No major deviations occur among the geometries, suggesting that changes in inlet height and angulation have minimal influence on the overall hydraulic resistance of the system. The plots of pressure and pressure drop are presented in Appendix B and C, respectively.

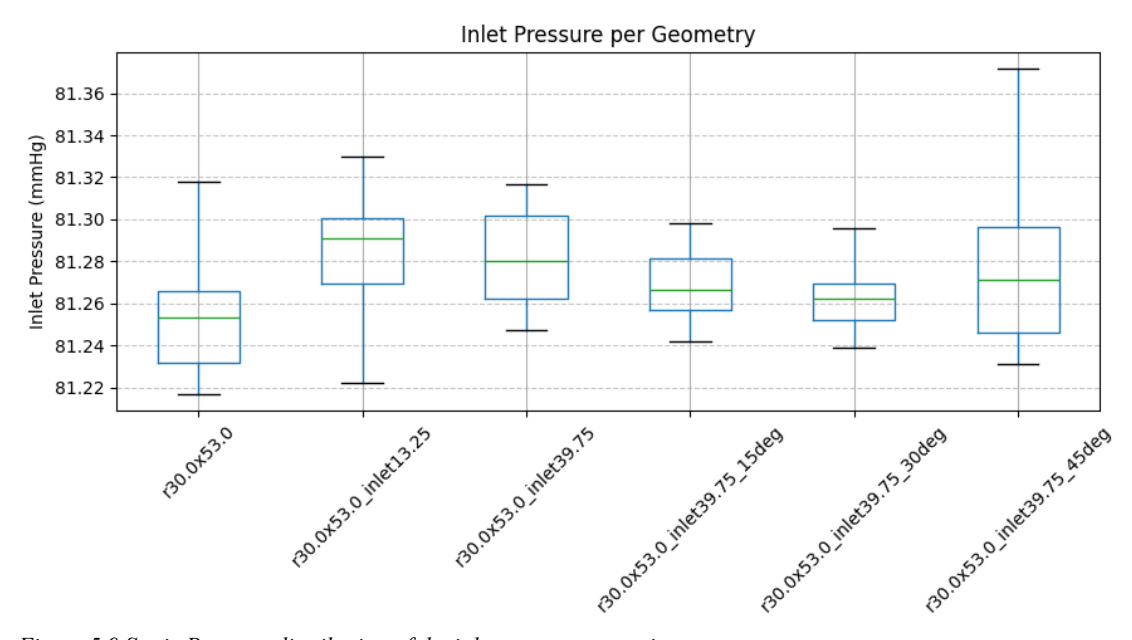


Figure 5.9 Static Pressure distribution of the inlet across geometries

The mean static pressure drop across all tested geometries in this study was 1.25–1.28mmHg, with only small differences between inlet height and angulations (see Figure 5.10). These values are consistent with findings in the literature. For example, Herbst et al. [88] reported pressure drops of 0.4-2.3mmHg for conventional arterial-line filters under physiological flow conditions, conducitng CFD analysis, meaining that the present bubble trap designs operate within the same range as other clinical devices. From a design perspective, this indicates that improvements in bubble entrapment efficiency and particularly in the 45° angled configuration, which achieved 99.4% efficiency, can be achieved without introducing additional hydraulic resistance.

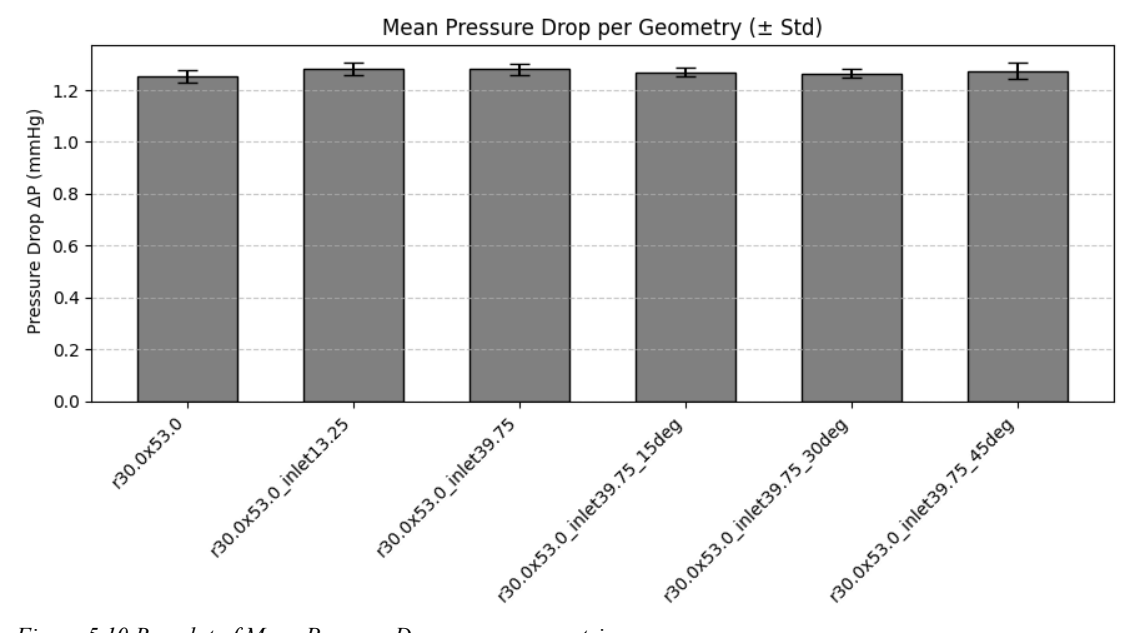
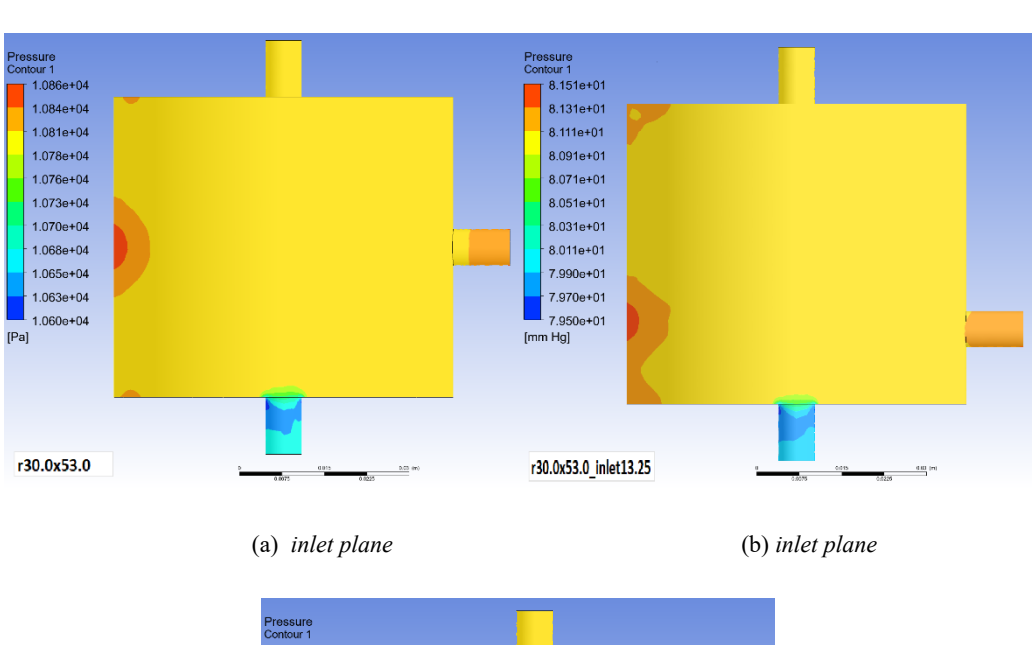
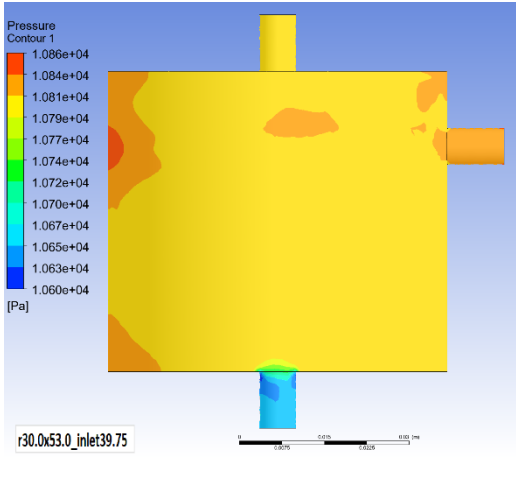
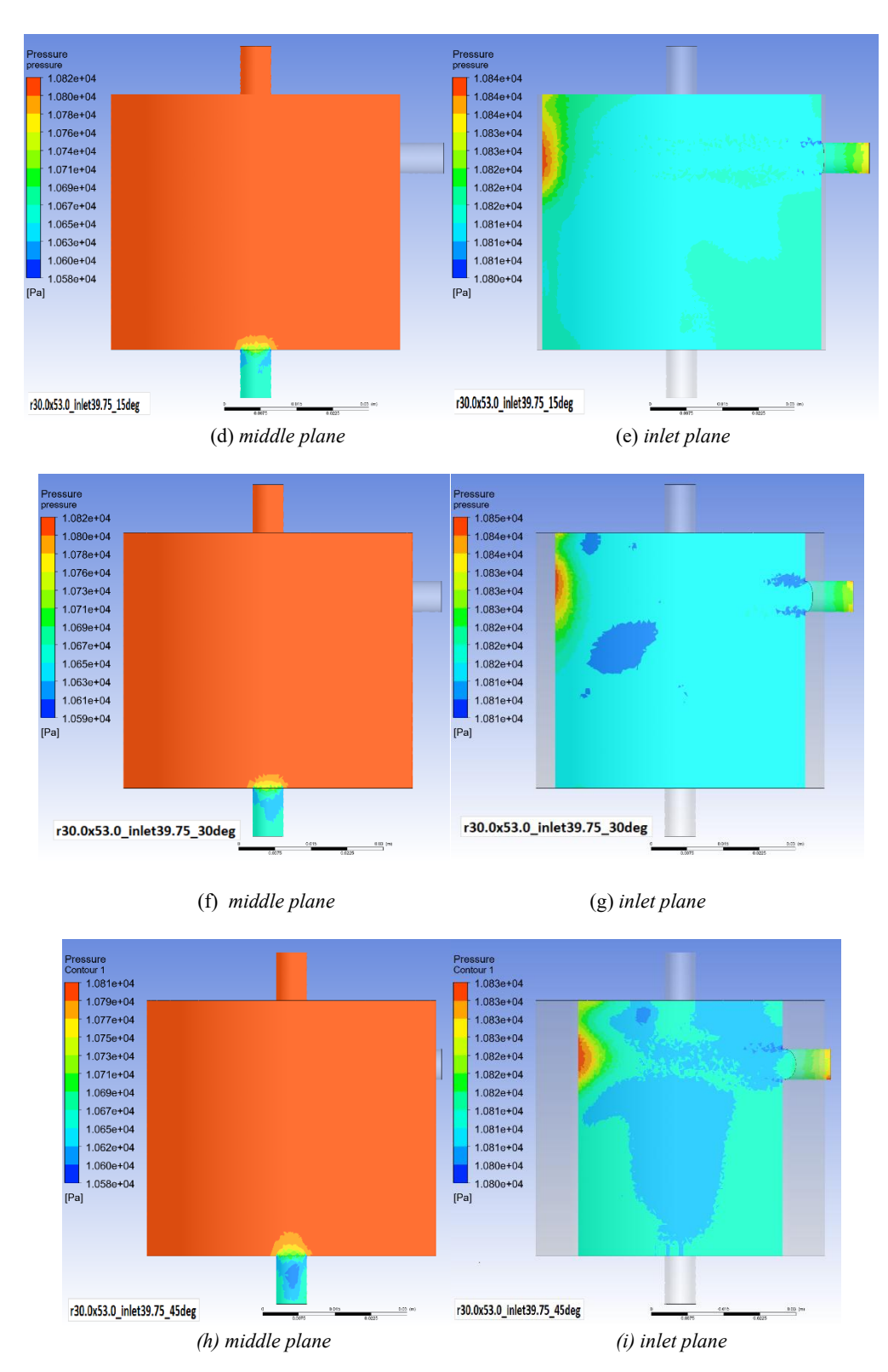


Figure 5.10 Bar plot of Mean Pressure Drop across geometries

From the Equation 3.17, given the surface tension of water at 37° C, the Laplace pressure across the gas–liquid interface for bubbles with diameters ranging from 50 to 500 μ m varies between 42.2 mmHg and 4.2 mmHg, respectively. Since the Laplace pressure is substantially higher than the flow-induced pressure drop, the imposed hydraulic gradient is insufficient to cause any deformation of the bubbles as they travel through the system. Consequently, the bubble dynamics within the chamber are primarily influenced by local flow recirculation patterns and shear forces, rather than by static pressure variations along the main flow direction.





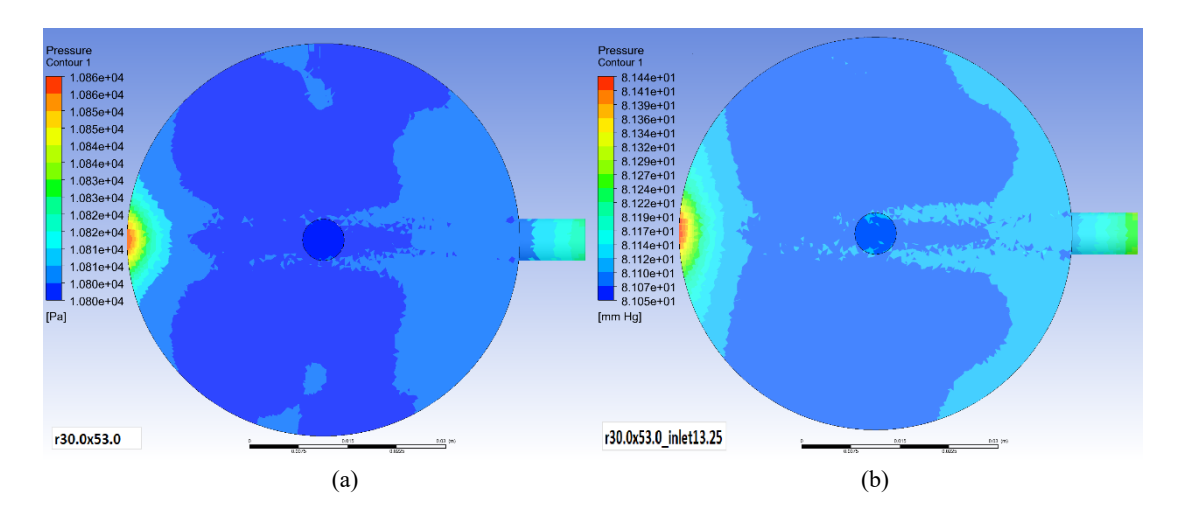


 $Figure \ 5.11 \ Contours \ of \ Static \ Pressure \ of \ the \ different \ configurations \ (a) \ r30.0x53.0 \ (b) \ r30.0x53.0 \ inlet 13.25 \ (c) \ r30.0x53.0 \ inlet 39.75 \ (d)-(e) \ r30.0x53.0 \ inlet 39.75 \ 15 deg \ , \ (f)-(g) \ r30.0x53.0 \ inlet 39.75 \ 30 deg \ , \ (h)-(i) \ r30.0x53.0 \ inlet 39.75 \ 45 deg$

From the static pressure contours (Figures 5.11), across all geometries, it can be observed that the pressure distribution within the chamber is relatively uniform, with no major difference in the middle plane observed between the geometries. The highest

pressure is noted at the inlet region and near the walls, where the perfusate jet enters the chamber, as the orientation of the inlet leads to stronger jet, creating zones of high pressure near the walls and localized high pressure zones can be observed along the chamber walls at the points where the inlet jet impinges, corresponding to regions of direct fluid impact, where momentum transfer from the entering jet increases static pressure. Lastly, the lowest pressure in all geometries occurred at the outlet at the bottom center, as expected, given that as the flow travels toward the outlet, energy is dissipated through frictional losses, turbulence, and recirculation, leading to a progressive reduction in static pressure. Also, according to Bernoulli's principle, the acceleration of the flow toward the outlet further lowers static pressure because of the previous reasons, which explains why the minimum values were consistently observed at the outlet region.

Furthermore, the top view contours of static pressure in the Figures 5.12 (a)-(f) are showing that with a tangential inlet, the entering jet imparts swirl momentum to the perfusate and the resulting swirling flow establishes a radial pressure gradient by radial equilibrium, so static pressure rises toward the outer wall where tangential velocity and the centrifugal term are largest and drops toward the center. As inlet angulation increases $(15^{\circ} \rightarrow 30^{\circ} \rightarrow 45^{\circ})$, the jet is directed more strongly along the wall, increasing the tangential momentum and thus the centrifugal pressure head at the walls. Consequently, the high-pressure ring along the wall becomes more pronounced, especially in the the configurations with inlet angulation (Figures 5.12 (d)-(f)) and spatially continuous, while the core remains comparatively low-pressure. Similar pressure distribution patterns have been reported in CFD studies of cyclone separators with swirl chambers, where tangential inlet flow generates a centrifugal field leading to higher static pressure near the walls and lower pressure along the central core [89]. The lower pressure in the center of the chamber creators calm regions, where bubbles and especially the smaller ones, move with the flow.



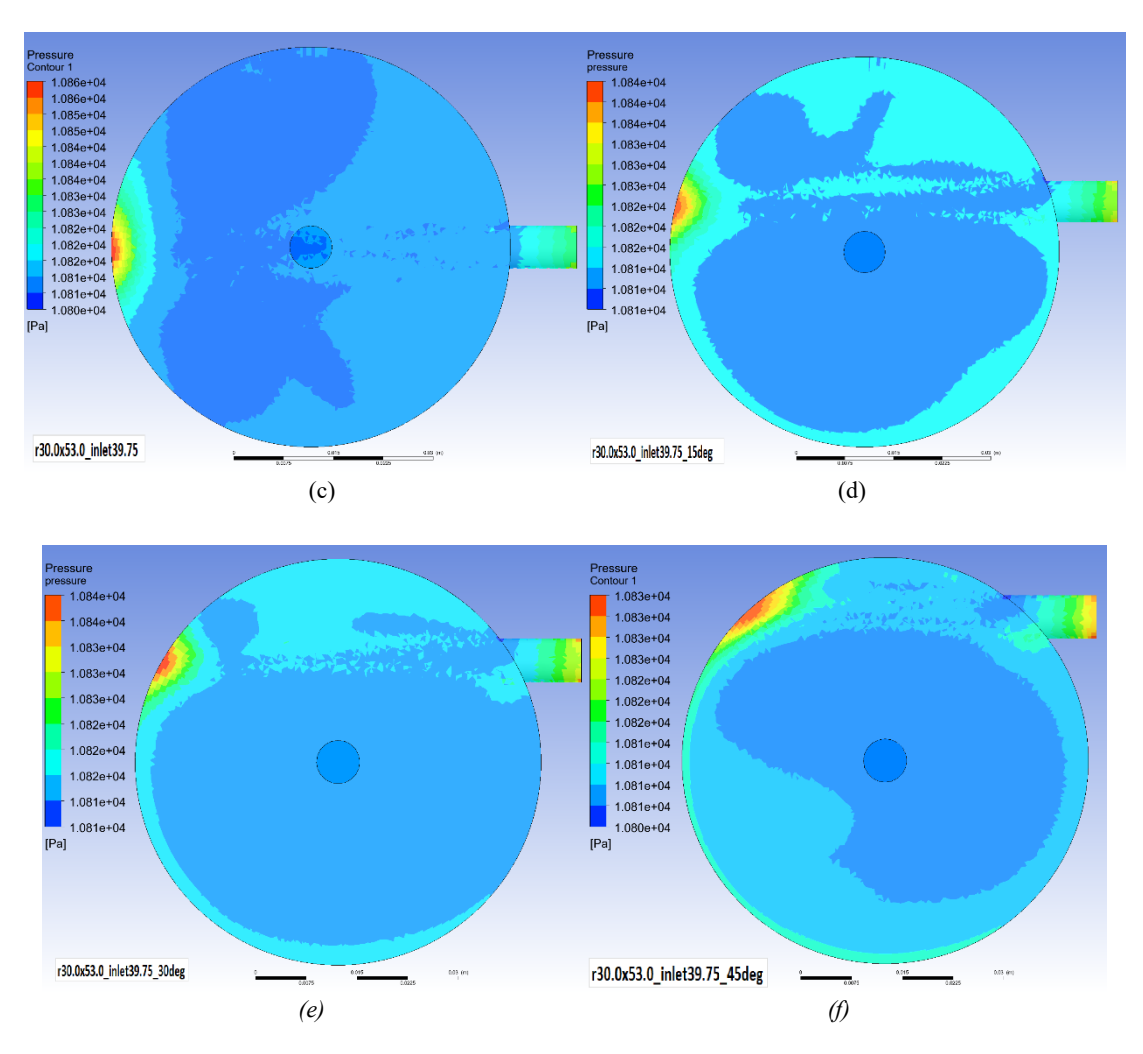


Figure 5.12 Cross Sectional Contours of Static Pressure (top view) on the inlet plane of the different configurations (a) r30.0x53.0 (b) r30.0x53.0 inlet13.25 (c) r30.0x53.0 inlet39.75 (d) r30.0x53.0 inlet39.75_15deg (e) r30.0x53.0 inlet39.75_30deg (f) r30.0x53.0 inlet39.75_45deg

5.3 Velocity

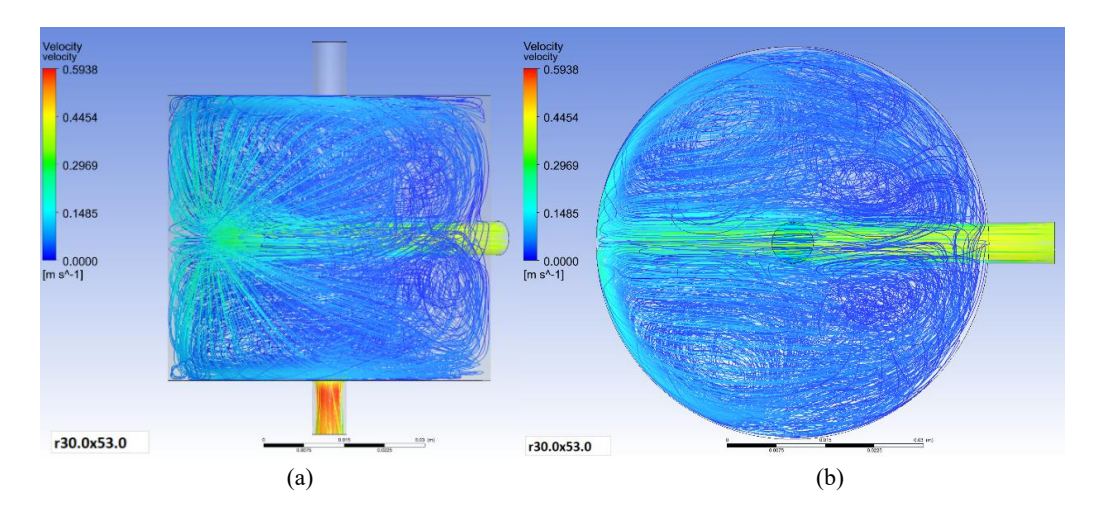
From the velocity magnitude streamlines that are presented below, it can be observed how the inlet affects the flow field inside the chamber and the trapping of bubbles. For the geometry r30.0x53.0 (see Figure 5.13 (a)-(b)), it can be observed that the flow enters at the middle and travels directly across the chamber and then creates a horizontal jet toward the walls. Recirculation zones can be visible at the top and bottom of the chamber, but the central jet provides a path for bubbles, especially for the smaller ones, to escape, a fact that explains the moderate efficiency of 93.87%.

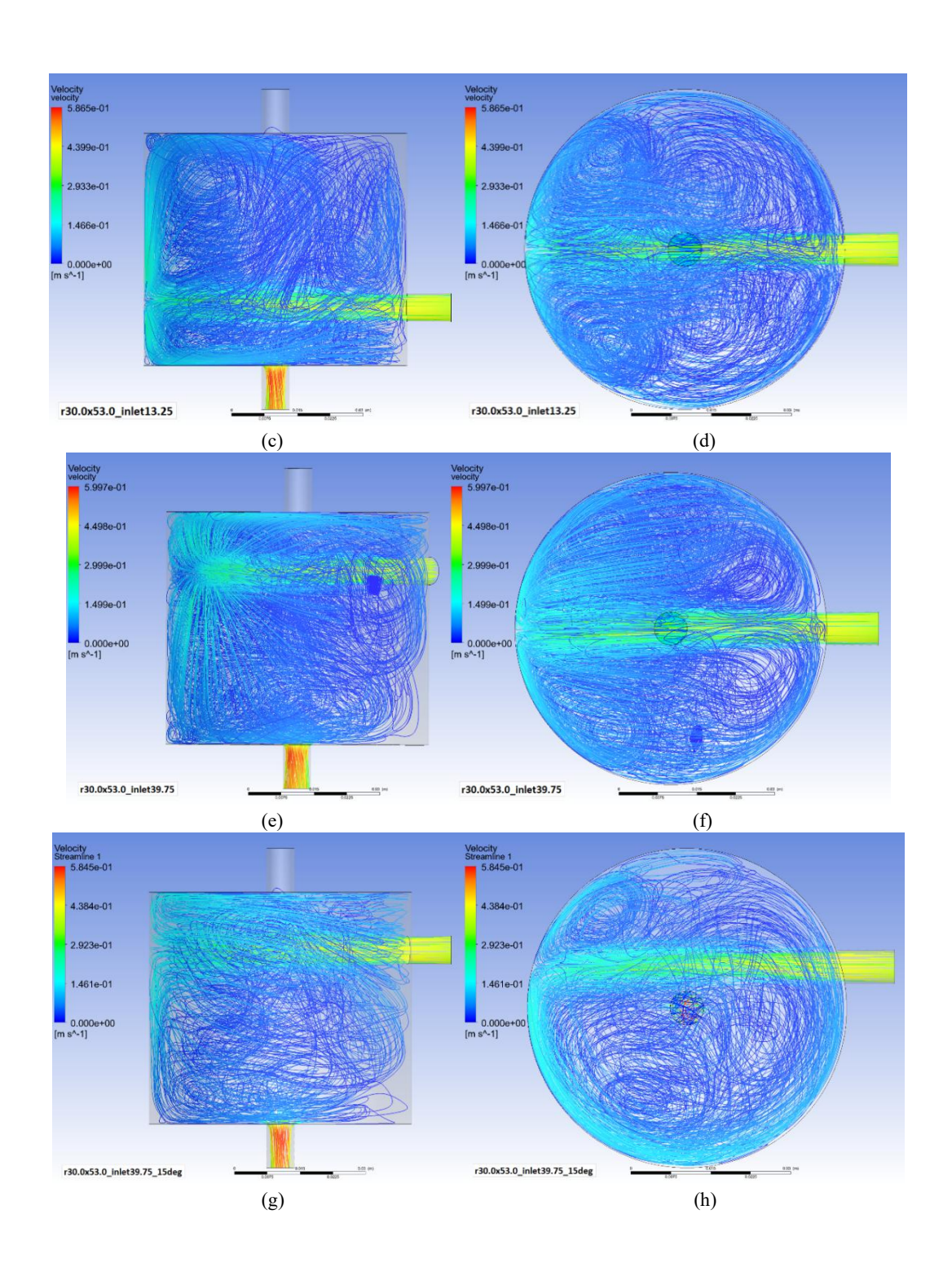
When the inlet is placed closer to the bottom of the outlet (see Figure 5.13 (c)-(d)), the jet is observed to be along the lower part of the chamber, where the streamlines show strong circulation near the base. Because the main jet is aligned with the outlet, bubbles have a higher probability of being transported directly out, explaining the reduced efficiency (93.33%) compared to the first geometry. Also, as the jet is closer to the outlet, bigger bubbles can escape as they don't have the time needed to rise to the top of the chamber and even larger bubbles, such as one of 200 µm and 300µm, were able to escape. Moreover, as discussed in paragraph 5.1.3, a higher number of bubbles

escaped during the early stages of the simulation in the geometry r30.0x53.0_inlet13.25, a fact that can be explained from the jet closer to the outlet, which allowed bubbles to be carried directly out of the chamber. As the inlet was placed higher, from the Figure 5.13 (e)-(f) it can be observed that the incoming jet was directed across the upper region, away from the outlet, reducing the likelihood of bubbles being immediately entrained toward the exit. As a result, bubbles had more time to rise under buoyancy, leading to an improved efficiency.

The geometries without inlet angulation appear multiple recirculation zones with flow patterns that allowed smaller bubbles to be entrained toward the outlet, reducing the overall trapping efficiency. From the Figures 5.13 (g)-(l), it can be observed that when angulation was introduced, the streamlines became smoother and increasingly aligned with the chamber walls. At the geometry r30.0x53.0_inlet39.75_15deg (see Figure 5.13 (g)-(h)), the incoming jet was starting to divert upward and began to align with the chamber wall, reducing the strength of the direct path toward the outlet. This trend is becoming more pronounced at 30° and 45° (see Figure 5.13 (i)-(l)), where the streamlines appeared progressively smoother, distributed across the chamber boundaries and following the walls, creating more smooth and extended recirculation zones, which increases the bubbles residence time and subsequent the efficiency.

In general, viscous shear forces, acting perpendicular to the main flow direction, are significant near the chamber walls and within regions of strong velocity gradients, as they induce lateral bubble migration, altering local vorticity and promoting mixing within the chamber. Furthermore, as the perfusate enters tangentially, it induces a swirling motion within the chamber, creating a pressure gradient where the pressure is higher near the walls and lower toward the centerline. This radial pressure difference generates a centrifugal effect that pushes both the liquid and entrained bubbles outward toward the chamber walls. For larger bubbles, this outward force, combined with buoyancy, helps them move toward the upper wall region where they accumulate and eventually separate due to the lower local velocity and higher buoyant rise. Smaller bubbles, however, experience a stronger influence from the drag and viscous forces compared to the centrifugal force, causing them to follow the recirculating flow patterns rather than separating immediately.





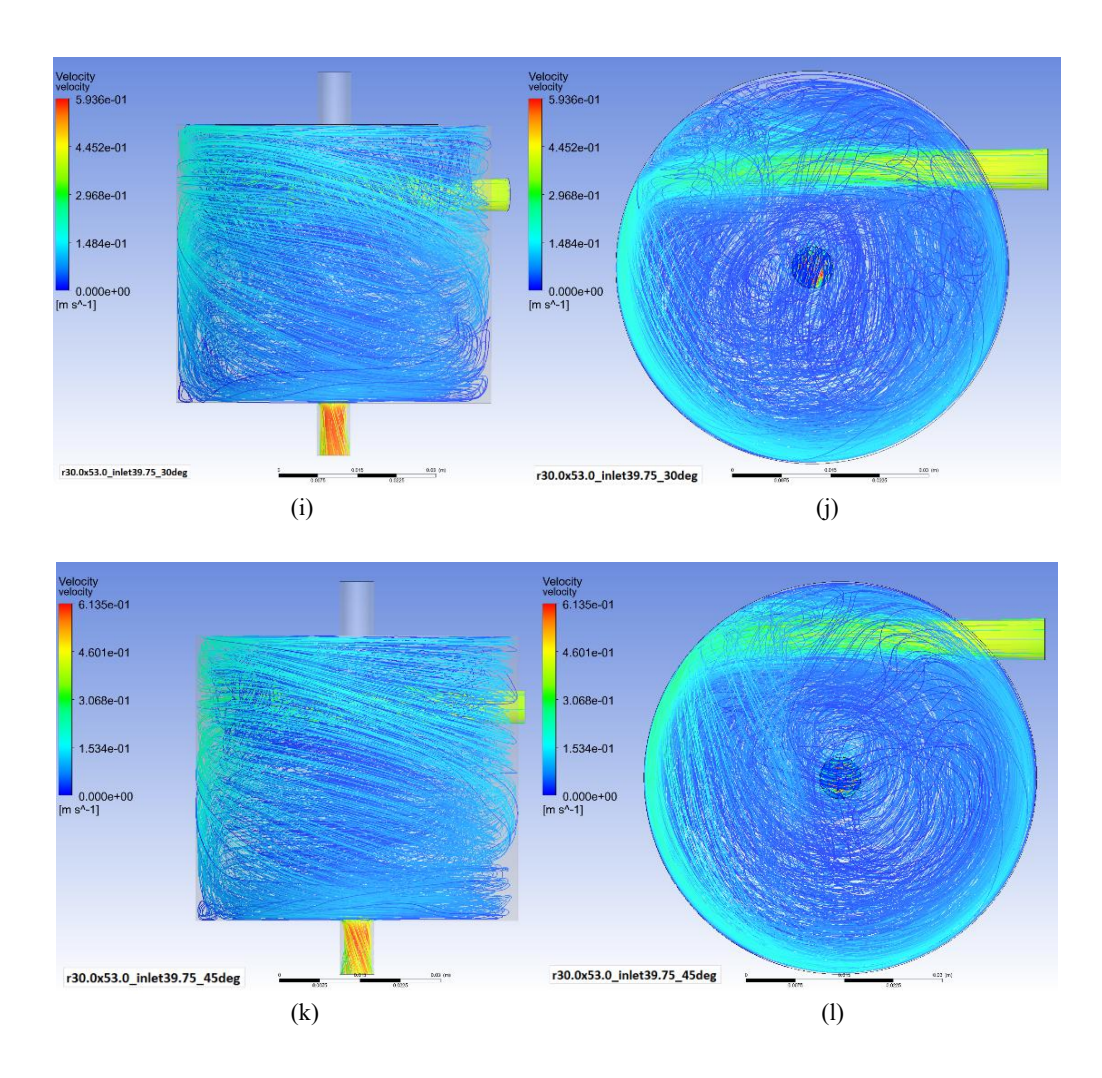


Figure 5.13 Velocity magnitude streamline plots for the different geometries (a)-(b) r30.0x53.0, (c)-(d) r30.0x53.0_inlet13.25 (e)-(f) r30.0x53.0_inlet39.75_15deg, (i)-(j) r30.0x53.0_inlet39.75_30deg, (k)-(l) r30.0x53.0_inlet39.75_45deg

During the simulations, it was observed that bubbles concentrated at the top region of the chamber, as the flow field promotes bubble accumulation in low velocity recirculation zones, as already discussed. For example in Figure 5.14 (r30.0x53.0_inlet39.75_45deg), it can be observed that the bubbles are concentrated at the top of the chamber, in a place where it is directly on the velocity jet, but in low velocity recirculation zone.

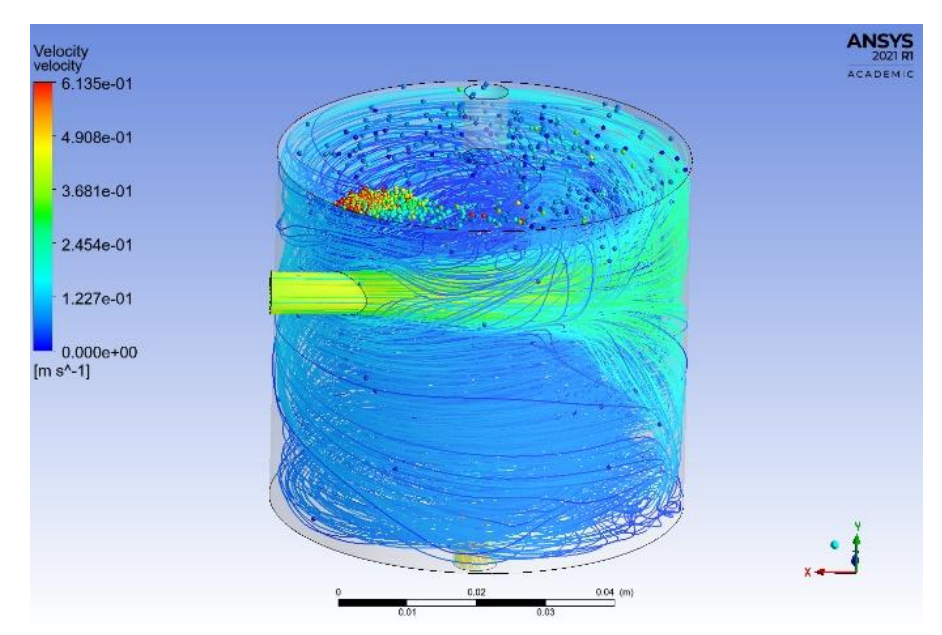


Figure 5.14 Bubbles distribution across the velocity streamlines of the geometry r30.0x53.0_inlet39.75_45deg.

The area-weighted average velocity magnitude at the outlet was monitored for all geometries and the plots are presented in the Appendix D. Across all cases, the outlet velocity stabilized close to the inlet velocity confirming mass conservation, as already discussed in Paragraph 4.5. Geometry r30.0x53.0 and low inlet r30.0x53.0 inlet13.25 presented nearly identical outlet velocity, with smooth temporal profiles that indicate stable flow. For the high-inlet geometry r30.0x53.0 inlet39.75, the mean outlet velocity magnitude remained consistent with the design value but displayed slightly larger fluctuations, reflecting the development of stronger recirculation zones inside the chamber. When inlet angulation was introduced (15°, 30°, 45°), the outlet velocity profiles showed minor increase in velocity magnitude value. This effect can be attributed to the combined influence of flow redirection and the presence of sharp edges, which promote local jet contraction and acceleration, as the angled inlet promotes enhanced mixing and redirects the flow toward the outlet, increasing local velocity magnitudes through recirculation and flow contraction near sharp edges.

5.4 Temperature

The mean outlet temperature across the six geometries revealed small numerical differences, all within the range of 36.991–36.993 °C. In the below Table 5:5 the mean values of outlet Temperature are presented:

Table 5:5 Mean values of outlet Temperatureare for all geometries.

	Mean Outlet Temperature ±Std
r30.0x53.0	36.991 ± 0.005
r30.0x53.0_inlet13.25	36.991 ± 0.005
r30.0x53.0_inlet39.75	36.993 ± 0.003
r30.0x53.0_inlet39.75_15deg	36.993 ± 0.003
r30.0x53.0_inlet39.75_30deg	36.992 ± 0.004
r30.0x53.0_inlet39.75_45deg	36.991 ± 0.005

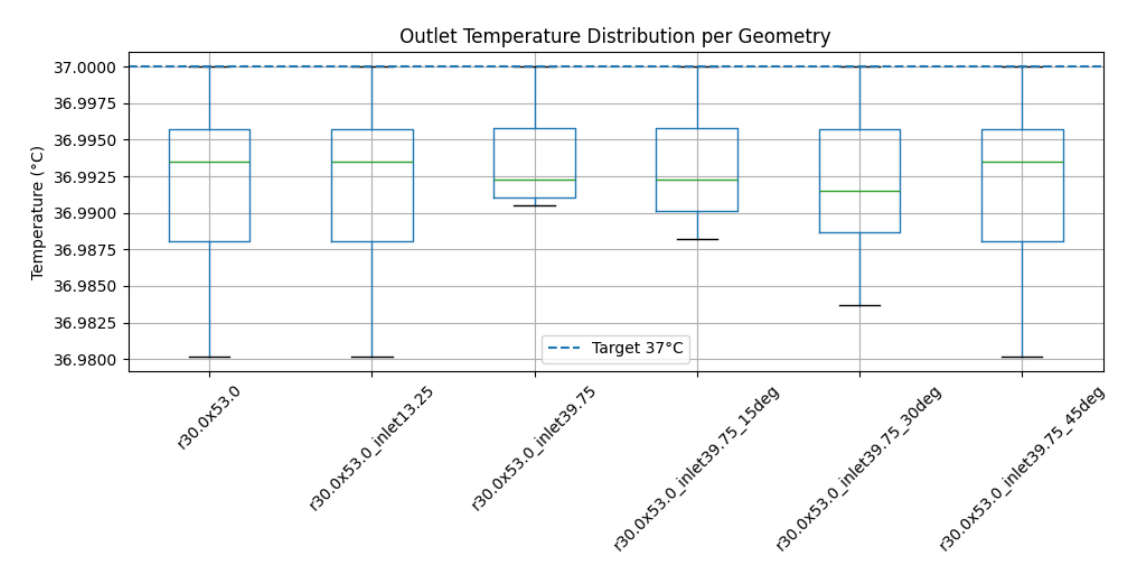
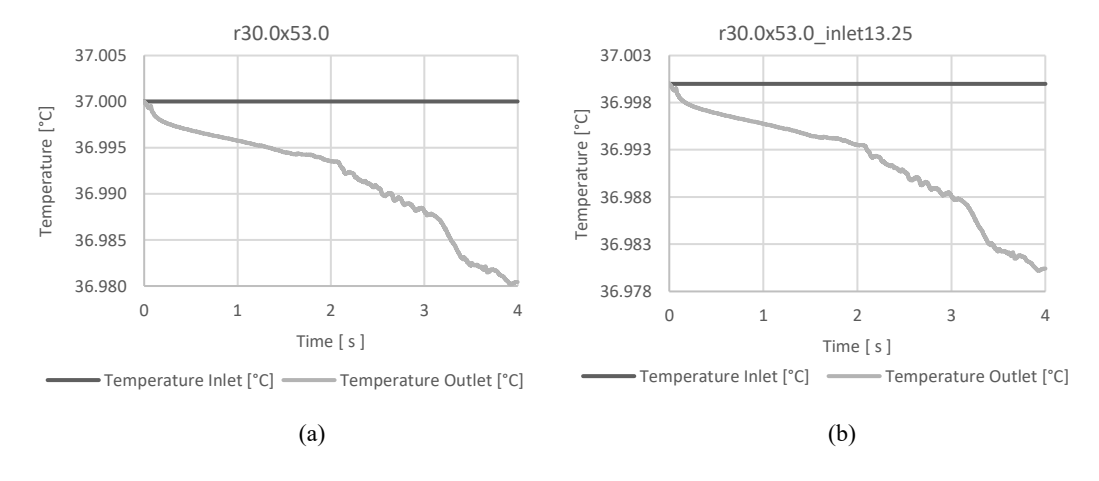


Figure 5.15 Outlet Temperature Distribution for all geometries.

Since the inlet temperature was set at 37 °C, the system maintained the fluid temperature very close to physiological conditions regardless of geometry (see Figure 5.15). All geometries maintained the perfusate temperature with minimal loss, ranging from 0.007 °C to 0.009 °C. The largest difference can be observed in the geometries r30.0x53.0, r30.0x53.0_inlet13.25, and r30.0x53.0_inlet39.75_45deg with outlet values of 36.991 °C representing 0.009 °C of loss. In contrast, the geometries r30.0x53.0_inlet39.75 and r30.0x53.0_inlet39.75_15deg have the smallest deviation, from the inlet value of 37 °C, where the outlet temperature decreased to 36.993 °C, corresponding to a loss of approximately 0.007 °C. The plots of the average weighted inlet and outlet temperature through time are presented below.



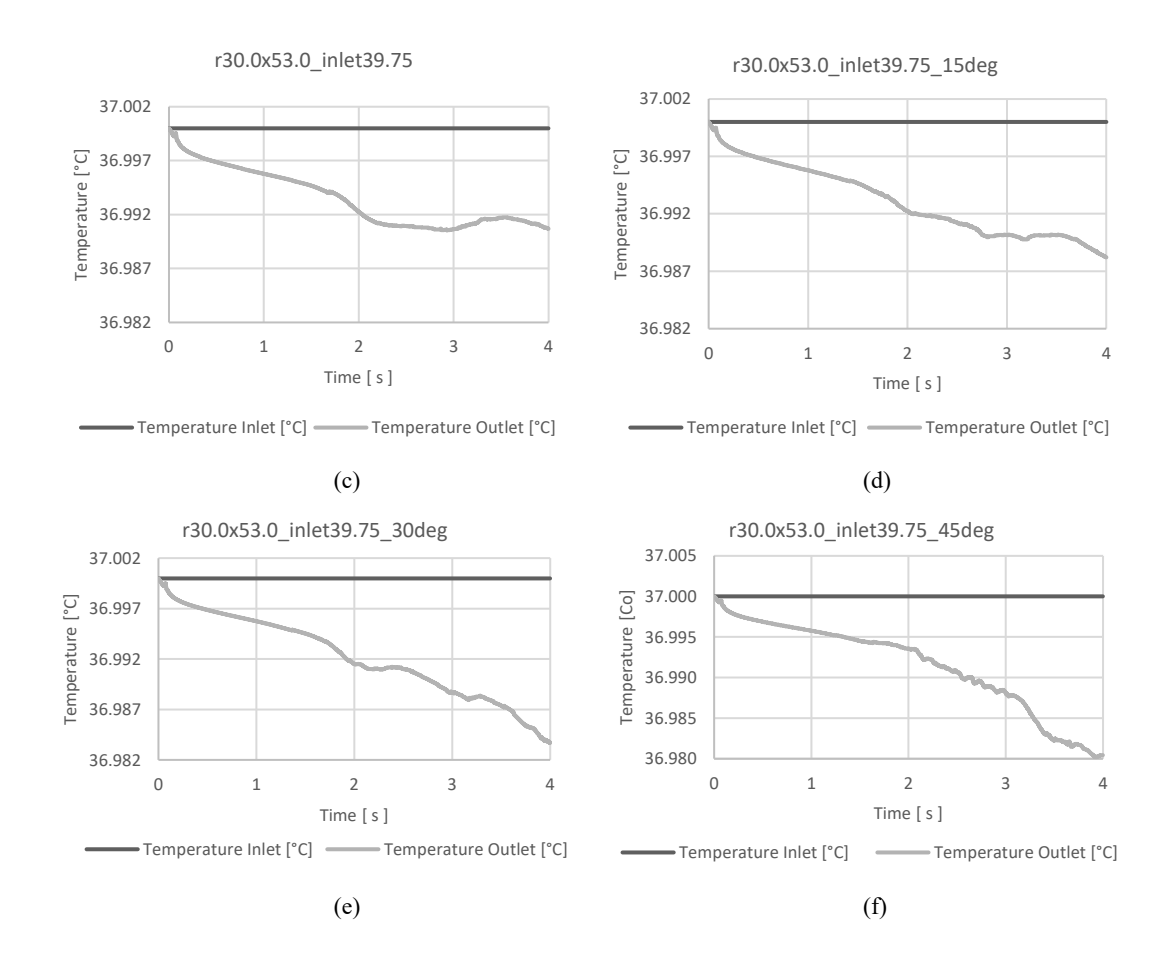


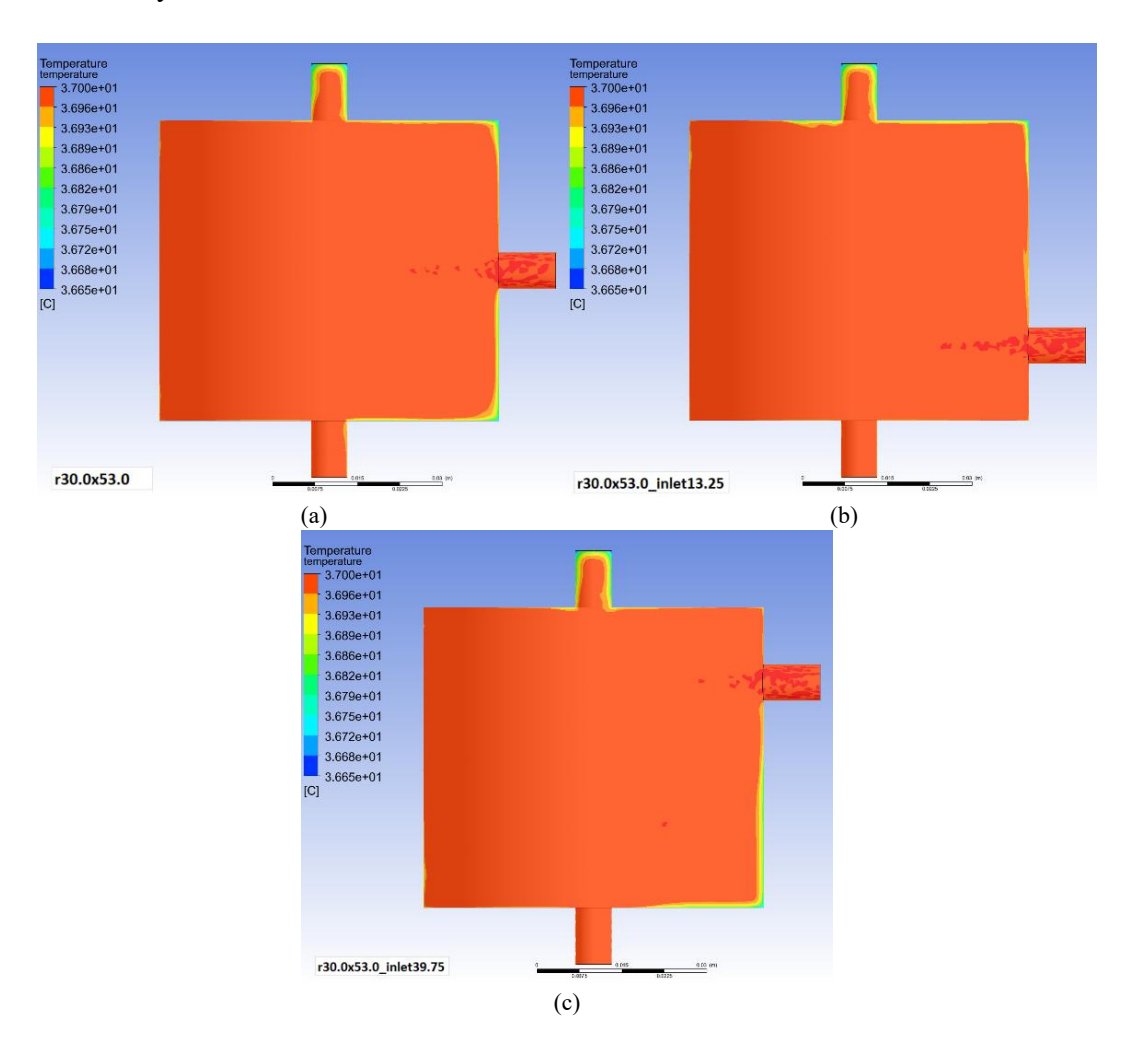
Figure 5.16 Plots of Average Weighted Temperature vs Time (a) r30.0x53.0 (b) r30.0x53.0_inlet13.25 (c) r30.0x53.0_inlet39.75 (d) r30.0x53.0_inlet39.75_15deg (e) r30.0x53.0_inlet39.75_30deg (f) r30.0x53.0 inlet39.75 45deg

As can be observed from the temperature contours (see Figures 5.17), as the perfusate enters the chamber at 37 °C, undergoes some heat loss across all geometries. In every configuration, lower temperature regions are located near the chamber walls, especially at the upper part of the chamber where the perfusate comes into contact with the environment and is linked to heat transfer through the chamber boundaries, as the larger contact surface area at the top facilitates greater losses. Additionally, localized cooler regions can be noted at the upper chamber where bubbles tend to accumulate, as bubbles reduce the effective thermal conductivity of the fluid domain and create zones of thermal insulation and enhance the local temperature drop. Localized cooler spots are also observed at the corners of the chamber, particularly in areas where the main jet does not directly impinge. In these zones, reduced flow mixing and weaker convective transport allow more heat to dissipate toward the walls. Spots with the higher temperature can be noted at the inlet, as the perfusate entering the chamber at 37 °C locally increases the temperature before mixing and heat dissipation occur.

For example, in the geometry r30.0x53.0 (Figure 5.17a), the temperature drop is primarily observed near the upper walls and in the bottom chamber corners, where the jet dissipates and heat transfer to the environment becomes more pronounced. The inlet13.25 configuration (see Figure 5.17b) shows a similar pattern but with slightly larger cooled zones near the corners at the top of the chamber and smaller at the bottom,

because the lower inlet position reduces direct jet impingement in the upper chamber, but is closer to the bottom of the chamber.

Additionally, in the geometry r30.0x53.0_inlet39.75 (Figure 5.17c), cooler zones can be spotted at the top of the chamber where the contact of the upper walls surface with the environment is larger and at the bottom of the chamber, as the strong jet is at the top of the chamber, where the inlet is positioned, away from the bottom part. Similarly, for the 15°, 30° and 40° angled inlets, cooler spots can be noted at the top and the bottom of the chambers for the reasons described above. Furthermore, at the inlet planes, at the top of the chamber cooler zones can be spotted at the top of the chamber where bubbles concerted near the inlet (see Figures 5.3-5.4), because of the reduced thermal conductivity that bubbles create.



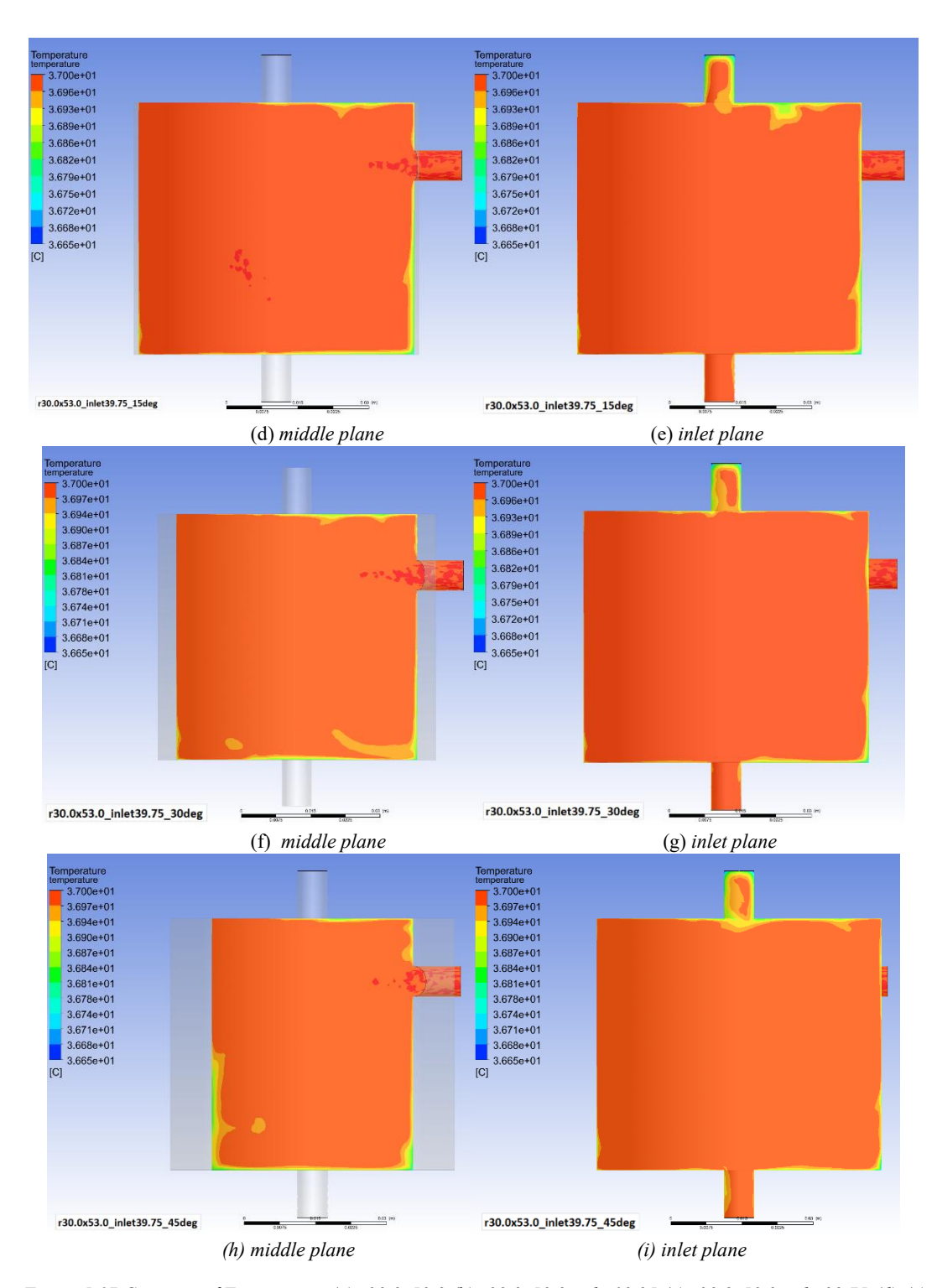


Figure 5.17 Contours of Temperature (a) r30.0x53.0 (b) r30.0x53.0_inlet13.25 (c) r30.0x53.0_inlet39.75 (d)-(e) r30.0x53.0_inlet39.75_15deg , (f)-(g) r30.0x53.0_inlet39.75_30deg , (h)-(i) r30.0x53.0_inlet39.75_45deg

Across all geometries (see Figures 5.17), the overall temperature distribution within the chamber appears uniform and no major differences in temperature can be spotted, suggesting that the inlet configuration primarily influences localized patterns rather than the overall thermal behavior of the chamber.

5.5 Turbulence Kinetic Energy

From the volume rendering contours of Turbulence Kinetic Energy, it can be observed that regions of high turbulence kinetic energy (TKE) correspond to the path of the inlet jet, indicating that turbulence is primarily generated by the strong velocity gradients and shear forces formed as the jet impinges on the chamber wall and interacts with the surrounding fluid. In the baseline geometry (see Figure 5.18a), the inlet jet enters the chamber horizontally and spreads toward the opposite wall, creating turbulence mainly in the central region, leading to the distribution of bubbles throughout the chamber, with a noticeable accumulation near the upper surface, as already discussed. On the other hand, when the inlet was positioned lower (Figure 5.18b) the jet became more direct and aligned with the outlet and the flow traveled along the lower part of the chamber, producing an elongated higher energy zone and elevated turbulence levels near the outlet, that can direct bubbles, especially smaller ones, to escape quickly.

In contrast, when the inlet was placed higher (Figure 5.18c), it is observed that the jet is entering closer to the upper section of the chamber and expanding along the upper part. This led to an increased turbulence near the top and calmer zones near the bottom, allowing bubbles to rise and accumulate near the upper surface. Thus, the reduced turbulence kinetic energy in the lower region and the upward recirculating pattern contributed to improved bubble retention and delayed escape.

When inlet angulation was introduced (15°, 30°, and 45° - Figures 5.18 (d)-(f)), zones of high turbulence kinetic energy (TKE) are concentrated along the path of the tangential inlet jet, especially near the wall impingement region where the flow first enters the chamber. In the 15° inlet angulation, the high-TKE region is concentrated near the inlet and extends moderately along the chamber wall, at 30° angulation, the jet becomes more closely aligned with the chamber wall and in the 45° angulation, the inlet jet adheres even more closely to the wall, creating a more high-TKE zone near the periphery of the chamber. The tangential momentum of the incoming flow establishes a swirling field that stabilizes as it progresses toward the chamber center. This generates a strong centrifugal effect, pushing bubbles outward and upward while maintaining a relatively low-turbulence region near the core. Consequently, most bubbles accumulate near the upper wall, where buoyancy dominates and escape to the outlet is minimized resulting in increased bubble trapping efficiency.

In general, high TKE regions correspond to the primary mixing zones, where momentum transfer between the incoming jet and the surrounding fluid generates turbulent eddies and this localized turbulence enhances bubble dispersion within the chamber. Finally, across all configurations, uncolored or transparent regions in the volume renderings corresponded to low-TKE zones can be noted, indicating stable and low-turbulence flow, where mainly located near the upper corners and chamber walls, acted as calm regions and where bubbles could remain suspended or gather under buoyancy forces.

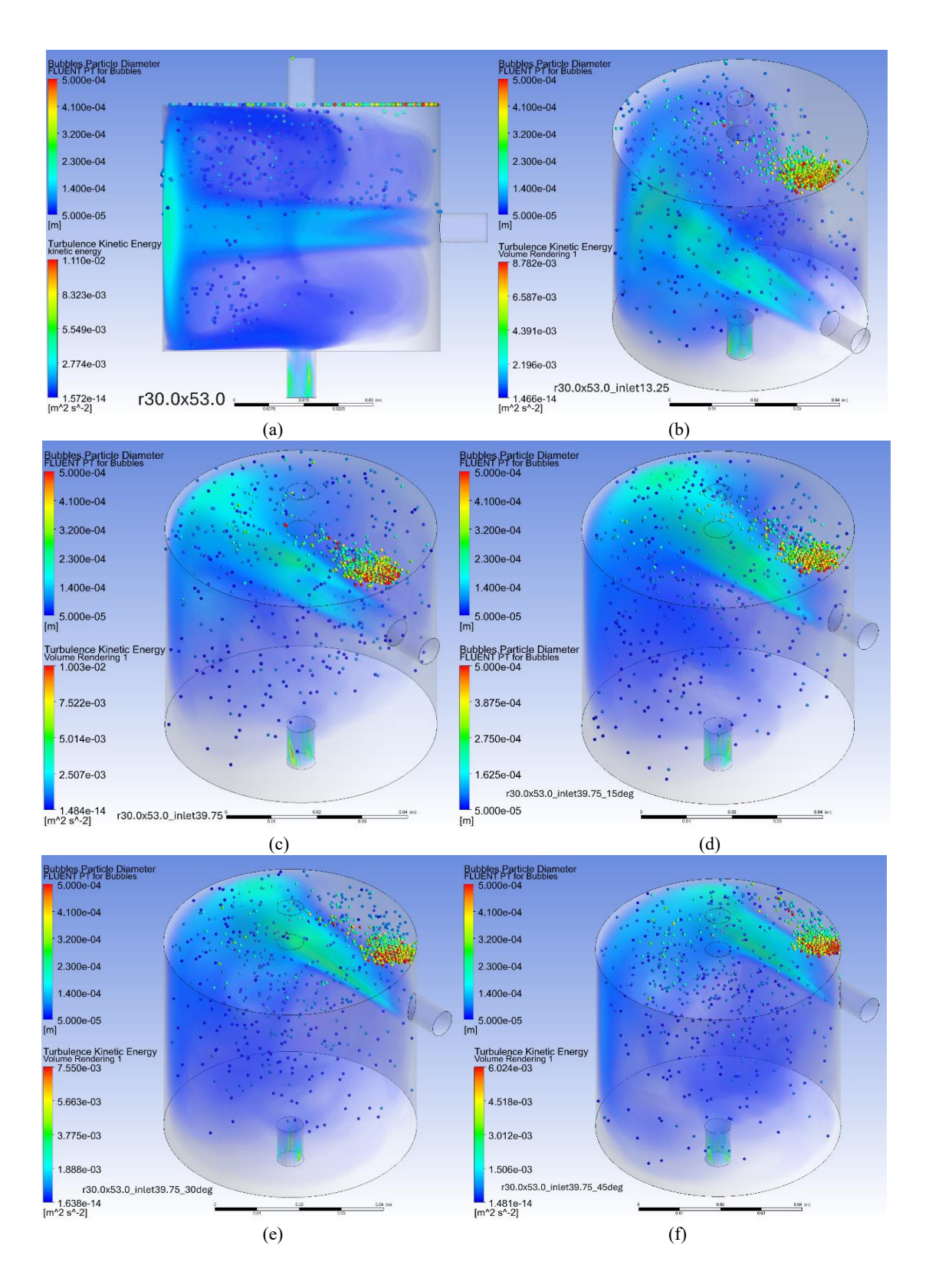


Figure 5.18 Volume Rendering Contours of Turbulence Kinetic Energy (a) r30.0x53.0 (b) r30.0x53.0_inlet13.25 (c) r30.0x53.0_inlet39.75 (d) r30.0x53.0_inlet39.75_15deg (e) r30.0x53.0_inlet39.75_30deg (f) r30.0x53.0_inlet39.75_45deg

6 Conclusion

6.1 Discussion

This study aimed to examine how the variations in inlet configuration affect the introduction of bubbles into the bubble trap in heart perfusion systems. For that a reason a series of CFD simulations were conducted on different geometrical configurations, by changing the inlet height and angulation.

In terms of efficiency, results showed that bubble trapping efficiency is influenced by the position and orientation of the inlet. More specifically, the baseline geometry r30.0x53.0, presented 93.87% efficiency during the insertion of the bubbles into the systems. It was observed that bubble escape began during the 2s of the simulation with the higher number of bubbles escaping during this period. When inlet was placed lower into the chamber and closer to the outlet of the perfusate, efficiency decreased to 93.33%, as the shortened flow path facilitated faster bubble escape from the outlet. In contrast, the geometry r30.0x53.0_inlet39.75, where the inlet was positioned higher in the chamber, led to an increased efficiency of 96.27%, as the elevated jet promoted the recirculation of bubbles into the chamber and delayed bubble escape.

Given the higher efficiency achieved with the elevated inlet position, an inlet angulation was introduced, in order to further examine whether the bubble escape behavior will be affected. When a 15° angulation was introduced to the inlet of the geometry r30.0x53.0_inlet39.75_15deg, efficiency increased to 97.33% and afterwards, with a 30° inlet angulation, geometry r30.0x53.0_inlet39.75_30deg, presented an increased efficiency of 97.53%. Finally, at 45° geometry r30.0x53.0_inlet39.75_45deg achieved the highest efficiency of 99.40%, with nine of 1500 bubbles escaping throughout the simulation, meaning that tangential inlets improve separation.

The velocity streamlines provided further insight into the relationship between inlet configuration and bubble trapping efficiency during the introduction of air bubbles to the system. In particular at the low-inlet geometry, the velocity jet was directed almost immediately toward the outlet, producing a more linear flow path that facilitated faster bubble escape and reduced efficiency, as the bubbles could escape during the first second of the simulation. By contrast, in the high-inlet geometry, the jet entered at an elevated position and spread across the chamber, promoting stronger recirculation and longer residence time, which delayed bubble release. When inlet angulation was introduced, the streamlines were redirected toward the chamber walls, generating broader recirculation zones and reducing the likelihood of bubbles following a direct path to the outlet. For that reason the angled configurations and particularly the 45° case, achieved the highest efficiency, as bubbles were forced into stable recirculation loops where buoyancy driven separation could occur before reaching the outlet.

Furthermore, in the low-inlet configuration (13.25 mm), bubbles began to escape almost immediately, with 30 bubbles lost during the first second, highlighting that a

direct alignment of the jet close to the outlet shortens residence time and reduces separation efficiency. Similarly, the geometry **r30.0x53.0** showed early bubble escape at 2 seconds, with strong peaks at 2–3 seconds. By contrast, the higher-inlet and angled geometries delayed the onset of bubble escape, with the 45° angulated inlet showing the latest and lowest release of bubbles, mainly concentrated at 4 seconds.

From these results, it can be concluded that the inlet position can influence the bubble trapping efficiency during the introduction of the bubbles to the system, as placing the inlet lower in the chamber and closer to the outlet led more bubbles to escape, whereas positioning it higher promoted recirculation and delayed their escape, resulting in higher overall efficiency. Also, these findings show that when introducing inlet angulation, can enhance the bubbles trapping efficiency by redirecting the jet toward the chamber walls, by creating stronger recirculation zones and minimizing direct bubble trajectories to the outlet.

During this study also it was noted that bubble size plays a significant role in bubble escape, as similar studies have shown and also from clinical practice. Smaller bubbles $(50-100~\mu\text{m})$ were consistently the ones most likely to escape, regardless of geometry, due to their lower buoyancy and stronger tendency to follow the carrier fluid streamlines. Larger bubbles ($\geq 300~\mu\text{m}$), on the other hand, were efficiently trapped across most of the geometries and were not observed at the outlet. Only one bubble of $200\mu\text{m}$ and $300~\mu\text{m}$ escaped in geometry in the low inlet configuration $\mathbf{r30.0x53.0_inlet13.25}$. This size-dependent escape behavior is consistent with findings in the literature [5], [8], [90], where microbubbles are known to be more challenging to remove in perfusion systems.

The analysis of static pressure and temperature distributions revealed that the different inlet configurations did not significantly affect the overall hydraulic and thermal performance of the system. Across all geometries, the mean static pressure drop remained nearly constant, ranging between 1.25 and 1.28 mmHg. Higher pressure values were located at the inlet, and the highest pressure was noted near the walls, where the jet impinges, while the lowest pressure occurred at the outlet, in accordance with Bernoulli's principle and energy dissipation along the flow path. Similarly, the temperature field was uniform in all cases, with a temperature loss of approximately 0.007–0.009 °C between the inlet and outlet. Cooler regions were observed along the upper chamber walls and corners, areas where bubbles accumulated and the fluid had prolonged contact with the environment, as well as at the bottom corners of the chamber. Finally, it was observed that bubbles tended to accumulate in regions of lower turbulent kinetic energy (TKE), where the local flow velocity and energy dissipation were reduced.

6.2 Recommendations for Future Research

Future studies could explore a wider range of geometrical configurations of the bubble trap that could affect and further optimize its efficiency in terms of bubbles escape. In particular, variations in the chamber diameter and height could be examined to determine how these parameters influence the internal flow field, bubble trajectories, and trapping efficiency. For example, the proportion of height/diameter of the chamber could be examined, to investigate whether there is an optimal value. In that way, it will be valuable to understand how the overall chamber volume and proportions affect the residence time of bubbles and their likelihood of being captured or escaping through the outlet. Moreover, different inlet and outlet arrangements could be tested to evaluate their impact on flow recirculation and bubble separation mechanisms. For instance, positioning the inlet and outlet at different vertical or horizontal locations, either toward the upper or lower regions of the chamber, in order to determine how their placement affects flow circulation or bubble rise behavior. Furthermore, the examined geometries could be tested in similar systems with higher flow needs, such as cardiopulmonary bypass (CPB) and extracorporeal membrane oxygenation (ECMO) circuits, where effective bubble removal is equally critical for patient safety.

Another recommendation for future work would be to test the geometries with the incorporation of filters with various materials and pore sizes to study the influence of bubble retention, especially for smaller bubbles. Moreover, the simulations can be conducted over longer time periods, in order to allow the observation of transient effects, including variations in pressure and temperature across different geometries, and provide a more comprehensive evaluation of long-term system stability under physiological conditions. Lastly, different types of injections, bubbles sizes or multiphase models, such as VOF could be tested.

7 References

- [1] O. Langendorff and A. Yon, 'Untersuchungen am überlebenden Säugethierherzen', *Pflüger*, *Arch*, vol. 70, pp. 473–486, 1898, Accessed: Dec. 15, 2024. [Online]. Available: https://doi.org/10.1007/BF01662056
- [2] S. Mangini *et al.*, 'Heart transplantation: review', Apr. 01, 2015. doi: 10.1590/S1679-45082015RW3154.
- [3] S. J. J. Langmuur, J. H. Amesz, K. M. Veen, A. J. J. C. Bogers, O. C. Manintveld, and Y. J. H. J. Taverne, 'Normothermic Ex Situ Heart Perfusion with the Organ Care System for Cardiac Transplantation: A Meta-analysis', Sep. 01, 2022, *Lippincott Williams and Wilkins*. doi: 10.1097/TP.00000000000004167.
- [4] A. Aliabadi-Zuckermann, A. Zuckermann, and M. R. Mehra, "'No Hearts Left Behind": A global proposal to rescue discarded donor hearts', *The Journal of Heart and Lung Transplantation*, Jul. 2025, doi: 10.1016/j.healun.2025.07.009.
- [5] M. Barak and Y. Katz, 'Microbubbles: Pathophysiology and clinical implications', *Chest*, vol. 128, no. 4, pp. 2918–2932, 2005, doi: 10.1378/chest.128.4.2918.
- [6] R. M. Bell, M. M. Mocanu, and D. M. Yellon, 'Retrograde heart perfusion: The Langendorff technique of isolated heart perfusion', Jun. 2011. doi: 10.1016/j.yjmcc.2011.02.018.
- [7] P. L. Marsh *et al.*, 'Iatrogenic air embolism: pathoanatomy, thromboinflammation, endotheliopathy, and therapies', 2023, *Frontiers Media SA*. doi: 10.3389/fimmu.2023.1230049.
- [8] C. Laus, M. M. Uth, and R. S. S. Hank, 'Gas Embolism', N Engl J Med, Feb. 2000.
- [9] D. M. Eckmann and S. L. Diamond, 'Surfactants Attenuate Gas Embolism-induced Thrombin Production', 2004. [Online]. Available: www.anesthesiology.org.
- [10] B. Schroeder, A. Barbeito, Shahar Bar-Yosef, and J. B. Mark, 'Chapter 45 Cardiovascular Monitoring', 2015. doi: 10.1016/B978-0-7020-5283-5.00045-X.
- [11] Heinz-Gerd Zimmer, 'The Isolated Perfused Heart and Its Pioneers', *NEWS IN PHYSIOLOGICAL SCIENCES*, vol. 13, 1998.
- [12] F. Wild, 'Ueber die peristaltische Bewegung des Oesophagus, nebst einigen Bemerkungen über diejenigen des Darms.', Zeitschrift für rationelle Medicin, vol. 5, pp. 76–132, 1846.
- [13] M. Skrzypiec-Spring, B. Grotthus, A. Szelag, and R. Schulz, 'Isolated heart perfusion according to Langendorff-Still viable in the new millennium', *J Pharmacol Toxicol Methods*, vol. 55, no. 2, pp. 113–126, Mar. 2007, doi: 10.1016/j.vascn.2006.05.006.
- [14] E. Cyon, 'Über den Einfluss der Temperaturänderungen auf Zahl, Dauer und Stärke der Herzschläge. Aus dem physiolog. Institut. Vorgelegt von C. Ludwig.', *Mathematisch- Physische Classe*, vol. 18, pp. 256–306, 1866.
- [15] H.N.Martin and M. Foster, 'The direct influence of gradual variations of temperature upon the rate of beat of the dogs', vol. XXI, pp. 663–690, 1883.
- [16] K. J. Broadley, 'The Langendorff Heart Preparation-Reappraisal of its Role as a Research and Teaching Model for Coronary Vasoactive Drugs'.

- [17] R. Lateef, A. Al-Masri, and A. Alyahya, 'Langendorff's isolated perfused rat heart technique: a review', *Int J Basic Clin Pharmacol*, pp. 1314–1322, 2015, doi: 10.18203/2319-2003.ijbcp20151381.
- [18] M. Soliman, 'PACING THE HEART: IS IT A MUST IN STUDYING MYOCARDIAL CONTRACTILE FUNCTION IN ISOLATED HEARTS PERFUSED USING THE LANGENDORFF SYSTEM'. [Online]. Available: https://www.researchgate.net/publication/265285514
- [19] Porter WT, 'A new method for the study of the isolated mammalian heart.', *Am J Physiol*, no. 1, pp. 511–518, 1898.
- [20] Schaefer EA, 'Do the coronary vessels possess vasomotor nerves?', *Arch Sci Biol*, no. II, pp. 251–257, 1904.
- [21] Bohr DF, 'Adrenergic receptors in coronary arteries.', *Ann NY Acad Sci*, vol. 139:, pp. 799–807, 1967.
- [22] L. C. Drew GM, 'Characterization of the coronary vascular p-adrenoceptors in the pig.', *Br J Pharmacology*, vol. 46, pp. 348–350, 1972.
- [23] K. J. Broadley, 'The Langendorff Heart Preparation-Reappraisal of its Role as a Research and Teaching Model for Coronary Vasoactive Drugs'.
- [24] N. Motayagheni, 'Modified Langendorff technique for mouse heart cannulation: Improved heart quality and decreased risk of ischemia', *MethodsX*, vol. 4, pp. 508–512, 2017, doi: 10.1016/j.mex.2017.11.004.
- [25] R. Liao, B. K. Podesser, and C. C. Lim, 'The continuing evolution of the Langendorff and ejecting murine heart: new advances in cardiac phenotyping', *Am J Physiol Heart Circ Physiol*, vol. 303, pp. 156–167, 2012, doi: 10.1152/ajpheart.00333.2012.-The.
- [26] X. Rossello, A. R. Hall, R. M. Bell, and D. M. Yellon, 'Characterization of the Langendorff Perfused Isolated Mouse Heart Model of Global Ischemia-Reperfusion Injury: Impact of Ischemia and Reperfusion Length on Infarct Size and LDH Release', *J Cardiovasc Pharmacol Ther*, vol. 21, no. 3, pp. 286–295, May 2016, doi: 10.1177/1074248415604462.
- [27] 'Isolated Heart Perfusion Systems for mouse to rabbit animal models Cardioplegia Refractory Period Tissue Engineering Contractility Studies Safety Pharmacology Cardiovascular Screening Myocyte Harvesting & Isolation Electrophysiology (ECG, MAP) Phenotyping of Transgenics Ischemia and Reperfusion Ex Vivo Perfusion Cardiac Mapping Hemodynamics'. [Online]. Available: www.harvardapparatus.com
- [28] Mike Poullis, 'Exploring the Boundaries of Perfusion. Left Field: Square Tubes and Current Changes!', *J Extra Corpor Technol*, vol. 2006, no. 41, Aug. 2009, doi: 10.1510/mmcts.2005.001198.
- [29] K. E. Gipson *et al.*, 'Elimination of gaseous microemboli from cardiopulmonary bypass using hypobaric oxygenation', *Annals of Thoracic Surgery*, vol. 97, no. 3, pp. 879–886, Mar. 2014, doi: 10.1016/j.athoracsur.2013.08.074.
- [30] S. Wang, B. J. Chin, F. Gentile, A. R. Kunselman, D. Palanzo, and A. Ündar, 'Potential Danger of Pre-Pump Clamping on Negative Pressure-Associated Gaseous Microemboli Generation During Extracorporeal Life Support-An In Vitro Study', *Artif Organs*, vol. 40, no. 1, pp. 89–94, Jan. 2016, doi: 10.1111/aor.12540.
- [31] F. Born, F. König, J. Chen, S. Günther, C. Hagl, and N. Thierfelder, 'Generation of Microbubbles in Extracorporeal Life Support and Assessment of New

- Elimination Strategies.', *Artif Organs*, vol. 44, no. 3, pp. 268–277, Mar. 2020, doi: 10.1111/aor.13557.
- [32] M. Schonburg *et al.*, 'A dynamic bubble trap reduces microbubbles during cardiopulmonary bypass: A case study', *Journal of Extra-Corporeal Technology*, vol. 32, no. 3, pp. 165–169, 2000, doi: 10.1051/ject/2000323165.
- [33] D. P. Herbst, 'Application of Micropore Filter Technology: Exploring the Blood Flow Path in Arterial-Line Filters and Its Effect on Bubble Trapping Functions', 2017.
- [34] R. E. Clark, R. A. Beauchamp, T. B. Ferguson, C. S. Weldon, and M. Louis, 'Comparison of bubble and membrane oxygenators in short and long perfusions', 1979.
- [35] M. N. Inamdar, B. V Venkataraman, and M. A. Aleem, 'A SIMPLE AND IMPROVED PERFUSION APPARATUS FOR ISOLATED HEARTS METHODS', 1994. [Online]. Available: http://journals.lww.com/iphr
- [36] M. Yacin Sikkandar, N. M. Sudharsan, S. Sabarunisha Begum, and E. Y. K. Ng, 'Computational Fluid Dynamics: A Technique to Solve Complex Biomedical Engineering Problems-A Review'.
- [37] E. I. Basri *et al.*, 'Computational Fluid Dynamics Study in Biomedical Applications: A Review', 2016. [Online]. Available: https://www.researchgate.net/publication/309389664
- [38] A. Santiago *et al.*, 'Fully coupled fluid-electro-mechanical model of the human heart for supercomputers', *Int J Numer Method Biomed Eng*, vol. 34, no. 12, Dec. 2018, doi: 10.1002/cnm.3140.
- [39] I. Mourouzis *et al.*, 'Effects of T3 Administration on Ex Vivo Rat Hearts Subjected to Normothermic Perfusion: Therapeutic Implications in Donor Heart Preservation and Repair', *Transplant International*, vol. 36, Feb. 2023, doi: 10.3389/ti.2023.10742.
- [40] F. Tu *et al.*, 'Triiodothyronine enhances cardiac contractility in septic rats and probably through Akt-Caspase9 pathway to reduce septic-induced cardiomyocyte apoptosis', *Mol Cell Probes*, vol. 66, Dec. 2022, doi: 10.1016/j.mcp.2022.101852.
- [41] A. I. Lourbopoulos, I. S. Mourouzis, A. G. Trikas, I. K. Tseti, and C. I. Pantos, 'Effects of thyroid hormone on tissue hypoxia: Relevance to sepsis therapy', Dec. 01, 2021, MDPI. doi: 10.3390/jcm10245855.
- [42] I. S. Mourouzis, A. I. Lourbopoulos, A. G. Trikas, I. K. Tseti, and C. I. Pantos, 'Triiodothyronine prevents tissue hypoxia in experimental sepsis: potential therapeutic implications', Dec. 01, 2021, *Springer Science and Business Media Deutschland GmbH*. doi: 10.1186/s40635-021-00382-y.
- [43] R. Pinnelas and J. A. Kobashigawa, 'Normothermic Perfusion in Heart Transplantation: A Review of the TransMedics® Organ Care System', *Future Cardiol*, vol. 18, no. 1, pp. 5–15, Jan. 2022, doi: 10.2217/fca-2021-0030.
- [44] J. E. Villanueva, Y. Joshi, S. Emmanuel, L. Gao, and P. S. Macdonald, 'Expanding Donor Heart Utilization Through Machine Perfusion Technologies', Dec. 01, 2022, *Springer Science and Business Media B.V.* doi: 10.1007/s40472-022-00375-0.
- [45] J. N. Schroder *et al.*, 'Transplantation Outcomes with Donor Hearts after Circulatory Death', *New England Journal of Medicine*, vol. 388, no. 23, pp. 2121–2131, Jun. 2023, doi: 10.1056/nejmoa2212438.

- [46] D. García Sáez *et al.*, 'Evaluation of the organ care system in heart transplantation with an adverse donor/recipient profile', *Annals of Thoracic Surgery*, vol. 98, no. 6, pp. 2099–2106, Dec. 2014, doi: 10.1016/j.athoracsur.2014.06.098.
- [47] S. Jou *et al.*, 'Heart transplantation: advances in expanding the donor pool and xenotransplantation', *Nat Rev Cardiol*, vol. 21, no. 1, pp. 25–36, Jan. 2024, doi: 10.1038/s41569-023-00902-1.
- [48] J. Stehlik *et al.*, 'The registry of the international society for heart and lung transplantation: 29th official adult heart transplant report 2012', *Journal of Heart and Lung Transplantation*, vol. 31, no. 10, pp. 1052–1064, Oct. 2012, doi: 10.1016/j.healun.2012.08.002.
- [49] N. M. Zahari *et al.*, 'Introduction of discrete phase model (DPM) in fluid flow: A review', in *AIP Conference Proceedings*, American Institute of Physics Inc., Nov. 2018. doi: 10.1063/1.5066875.
- [50] Z. Valizadeh, M. Shams, and H. Dehghani, 'Eulerian- lagrangian dense discrete phase model (DDPM) of stenotic LAD coronary arteries in comparison with single phase modeling', *Med Eng Phys*, vol. 128, Jun. 2024, doi: 10.1016/j.medengphy.2024.104164.
- [51] J. S. Shirolkar, C. F. M. Coimbra, and M. Queiroz Mcquay, 'FUNDAMENTAL ASPECTS OF MODELING TURBULENT PARTICLE DISPERSION IN DILUTE FLOWS', 1996.
- [52] W. P. Adamczyk, A. Klimanek, R. A. Białecki, G. Węcel, P. Kozołub, and T. Czakiert, 'Comparison of the standard Euler-Euler and hybrid Euler-Lagrange approaches for modeling particle transport in a pilot-scale circulating fluidized bed', *Particuology*, vol. 15, pp. 129–137, 2014, doi: 10.1016/j.partic.2013.06.008.
- [53] D. Hirche, F. Birkholz, and O. Hinrichsen, 'A hybrid Eulerian-Eulerian-Lagrangian model for gas-solid simulations', *Chemical Engineering Journal*, vol. 377, Dec. 2019, doi: 10.1016/j.cej.2018.08.129.
- [54] Z. Zhang and Q. Chen, 'Comparison of the Eulerian and Lagrangian methods for predicting particle transport in enclosed spaces', *Atmos Environ*, vol. 41, no. 25, pp. 5236–5248, Aug. 2007, doi: 10.1016/j.atmosenv.2006.05.086.
- [55] J. R. G. M. E. W. Roland Clift, *Bubbles, Drops, and Particles*. 2005.
- [56] E. Loth, 'PARTICLES, DROPS AND BUBBLES: FLUID DYNAMICS AND NUMERICAL METHODS', 2010.
- [57] J. Magnaudet and I. Eames, 'THE MOTION OF HIGH-REYNOLDS-NUMBER BUBBLES IN INHOMOGENEOUS FLOWS', 2000. [Online]. Available: www.annualreviews.org
- [58] M. C. Ruzicka, 'On bubbles rising in line', 2000. [Online]. Available: www.elsevier.com/locate/ijmulflow
- [59] M. Schlüter, S. Scheid, S. John, and N. Räbiger, 'Fluidization of Fine Particles in Bubble Wakes Affects Hydrodynamics in Three-Phase Flows', 2004.
- [60] 'CAVITATION AND BUBBLE DYNAMICS'.
- [61] P. G. Saffman, 'The lift on a small sphere in a slow shear flow', 1965.
- [62] N. M. Zahari *et al.*, 'Introduction of discrete phase model (DPM) in fluid flow: A review', in *AIP Conference Proceedings*, American Institute of Physics Inc., Nov. 2018. doi: 10.1063/1.5066875.

- [63] D. C. Wilcox, 'Reassessment of the scale-determining equation for advanced turbulence models', *AIAA Journal*, vol. 26, no. 11, pp. 1299–1310, Nov. 1988, doi: 10.2514/3.10041.
- [64] F. R. Menter, 'Improved Two-Equation k-Turbulence Models for Aerodynamic Flows'.
- [65] F. R. Menter, 'Two-equation eddy-viscosity turbulence models for engineering applications', *AIAA Journal*, vol. 32, no. 8, pp. 1598–1605, 1994, doi: 10.2514/3.12149.
- [66] M. Faram, 'CFD for the Water Industry; The Role of CFD as a Tool for the Development of Wastewater Treatment Systems', 2000. [Online]. Available: https://www.researchgate.net/publication/237644314
- [67] M. Mohsin and D. R. Kaushal, 'A 2D-CFD (VOF model) analysis of invert trap for bed load removal in an open rectangular sewer drain', *Particulate Science and Technology*, vol. 35, no. 1, pp. 54–66, Jan. 2017, doi: 10.1080/02726351.2015.1131786.
- [68] K. A. Kadipasaoglu *et al.*, 'Laboratory Investigation An Ex Vivo Model for the Reperfusion of Explanted Human Hearts', 1993.
- [69] M. Alomari *et al.*, 'Is the Organ Care System (OCS) Still the First Choice With Emerging New Strategies for Donation After Circulatory Death (DCD) in Heart Transplant?', *Cureus*, Jun. 2022, doi: 10.7759/cureus.26281.
- [70] A. Ardehali *et al.*, 'Ex-vivo perfusion of donor hearts for human heart transplantation (PROCEED II): A prospective, open-label, multicentre, randomised non-inferiority trial', *The Lancet*, vol. 385, no. 9987, pp. 2577–2584, Jun. 2015, doi: 10.1016/S0140-6736(15)60261-6.
- [71] N. Pizanis *et al.*, 'Introduction of machine perfusion of donor hearts in a single center in Germany', *IJC Heart and Vasculature*, vol. 47, Aug. 2023, doi: 10.1016/j.ijcha.2023.101233.
- [72] M. M. Koerner, A. Ghodsizad, U. Schulz, A. El Banayosy, R. Koerfer, and G. Tenderich, 'Normothermic ex vivo allograft blood perfusion in clinical heart transplantation', *Heart Surgery Forum*, vol. 17, no. 3, 2014, doi: 10.1532/HSF98.2014332.
- [73] F. J. Sutherland and D. J. Hearse, 'THE ISOLATED BLOOD AND PERFUSION FLUID PERFUSED HEART', *Pharmacol Res*, vol. 41, no. 6, 2000, doi: 10.1006rphrs.2000.0653.
- [74] J.M. de Bakker et al., 'Ventricular human heart', *J Am Coll Cardiol*, no. 15, pp. 1594–1607, 1990.
- [75] B. L. Spencer *et al.*, 'Extending heart preservation to 24 h with normothermic perfusion', *Front Cardiovasc Med*, vol. 11, 2024, doi: 10.3389/fcvm.2024.1325169.
- [76] C. Gonzalez-Castillo, R. Rubio, and T. Zenteno-Savin, 'Coronary flow-induced inotropism is modulated by binding of dextrans to the endothelial luminal surface', *Am J Physiol Heart Circ Physiol*, vol. 284, pp. 1348–1357, 2003, doi: 10.1152/ajpheart.00323.
- [77] V. Olejnickova, M. Novakova, and I. Provaznik, 'Isolated heart models: cardiovascular system studies and technological advances', Jul. 22, 2015, *Springer Verlag.* doi: 10.1007/s11517-015-1270-2.
- [78] G. B. Fiore, U. Morbiducci, R. Ponzini, and A. Redaelli, 'Bubble tracking through computational fluid dynamics in arterial line filters for cardiopulmonary

- bypass', ASAIO Journal, vol. 55, no. 5, pp. 438–444, Sep. 2009, doi: 10.1097/MAT.0b013e3181b3800c.
- [79] C. L. Wu, A. S. Berrouk, and K. Nandakumar, 'Three-dimensional discrete particle model for gas-solid fluidized beds on unstructured mesh', *Chemical Engineering Journal*, vol. 152, no. 2–3, pp. 514–529, Oct. 2009, doi: 10.1016/j.cej.2009.05.024.
- [80] ANSYS Fluent User Guide. 2023.
- [81] C. L. Rumsey and P. R. Spalart, 'Turbulence Model Behavior in Low Reynolds Number Regions of Aerodynamic Flowfields For submission to AIAA Journal'.
- [82] M. Wang, Q. Nie, G. Xie, Z. Tan, and H. Yu, 'Mathematical Modelling and CFD Simulation for Oxygen Removal in a Multi-Function Gas-Liquid Contactor', *Processes*, vol. 11, no. 6, Jun. 2023, doi: 10.3390/pr11061780.
- [83] S. Sarfare *et al.*, 'Computational Fluid Dynamics Turbulence Model and Experimental Study for a Fontan Cavopulmonary Assist Device', *J Biomech Eng*, vol. 145, no. 11, Oct. 2023, doi: 10.1115/1.4063088.
- [84] V. Papadopoulou, M. X. Tang, C. Balestra, R. J. Eckersley, and T. D. Karapantsios, 'Circulatory bubble dynamics: From physical to biological aspects', 2014, *Elsevier*. doi: 10.1016/j.cis.2014.01.017.
- [85] H. K. Versteeg and W. Malalasekera, 'An Introduction to Computational Fluid Dynamics Second Edition'. [Online]. Available: www.pearsoned.co.uk/versteeg
- [86] M. Puthettu, S. Vandenberghe, P. Bagnato, M. Gallo, and S. Demertzis, 'Gaseous Microemboli in the Cardiopulmonary Bypass Circuit: Presentation of a Systematic Data Collection Protocol Applied at Istituto Cardiocentro Ticino', *Cureus*, Feb. 2022, doi: 10.7759/cureus.22310.
- [87] E. M. L. Chung *et al.*, 'Size distribution of air bubbles entering the brain during cardiac surgery', *PLoS One*, vol. 10, no. 4, Apr. 2015, doi: 10.1371/journal.pone.0122166.
- [88] D. P. Herbst and H. K. Najm, 'Development of a New Arterial-Line Filter Design Using Computational Fluid Dynamics Analysis'.
- [89] K. Elsayed and C. Lacor, 'The effect of cyclone inlet dimensions on the flow pattern and performance', *Appl Math Model*, vol. 35, no. 4, pp. 1952–1968, Apr. 2011, doi: 10.1016/j.apm.2010.11.007.
- [90] M. Schönburg Kerckhoff-Klinik *et al.*, 'Significant reduction of air microbubbles with the dynamic bubble trap during cardiopulmonary bypass', 2001.

7 References

8 Appendix

8.1 Appendix A: Escaped Bubbles per Size through time

Table 8:1 Number of Escaped Bubbles by Size and Time for the Geometry r30.0x53.0.

	50μm	100μm	200µm	300µm	400μm	500μm
1 s	0	0	0	0	0	0
2s	34	6	0	0	0	0
<i>3s</i>	26	12	1	0	0	0
4s	11	2	0	0	0	0
Total	71	20	1	0	0	0

Table 8:2 Number of Escaped Bubbles by Size and Time for the Geometry r30.0x53.0_inlet13.25.

	50μm	100μm	200µm	300µm	400μm	500μm
1s	21	7	1	1	0	0
2s	27	5	0	0	0	0
<i>3s</i>	16	5	0	0	0	0
4s	15	2	0	0	0	0
Total	79	19	1	1	0	0

Table 8:3 Number of Escaped Bubbles by Size and Time for the Geometry r30.0x53.0_inlet39.75.

	50μm	100μm	200μm	300µm	400μm	500μm
1 s	0	0	0	0	0	0
2s	5	1	0	0	0	0
<i>3s</i>	28	5	0	0	0	0
4s	15	2	0	0	0	0
Total	48	8	0	0	0	0

Table 8:4 Number of Escaped Bubbles by Size and Time for the Geometry r30.0x53.0_inlet39.75_15deg.

	50μm	100μm	200μm	300µm	400μm	500μm
1 s	0	0	0	0	0	0
2s	8	0	0	0	0	0
3s	7	5	0	0	0	0
4 s	17	3	0	0	0	0
Total	32	8	0	0	0	0

8 Appendix

Table 8:5 Number of Escaped Bubbles by Size and Time for the Geometry r30.0x53.0_inlet39.75_30deg.

	50μm	100μm	200µm	300µm	400μm	500μm
1 s	0	0	0	0	0	0
2s	4	0	0	0	0	0
3s	19	2	0	0	0	0
4 s	9	3	0	0	0	0
Total	32	5	0	0	0	0

 $\textit{Table 8:6 Number of Escaped Bubbles by Size and Time for the Geometry } r30.0x53.0_inlet 39.75_45 deg.$

	50μm	100μm	200µm	300µm	400μm	500μm
1 s	0	0	0	0	0	0
2s	1	0	0	0	0	0
<i>3s</i>	1	0	0	0	0	0
4s	7	0	0	0	0	0
Total	9	0	0	0	0	0

8.2 Appendix B: Plots of Pressure Area-Weighted Average

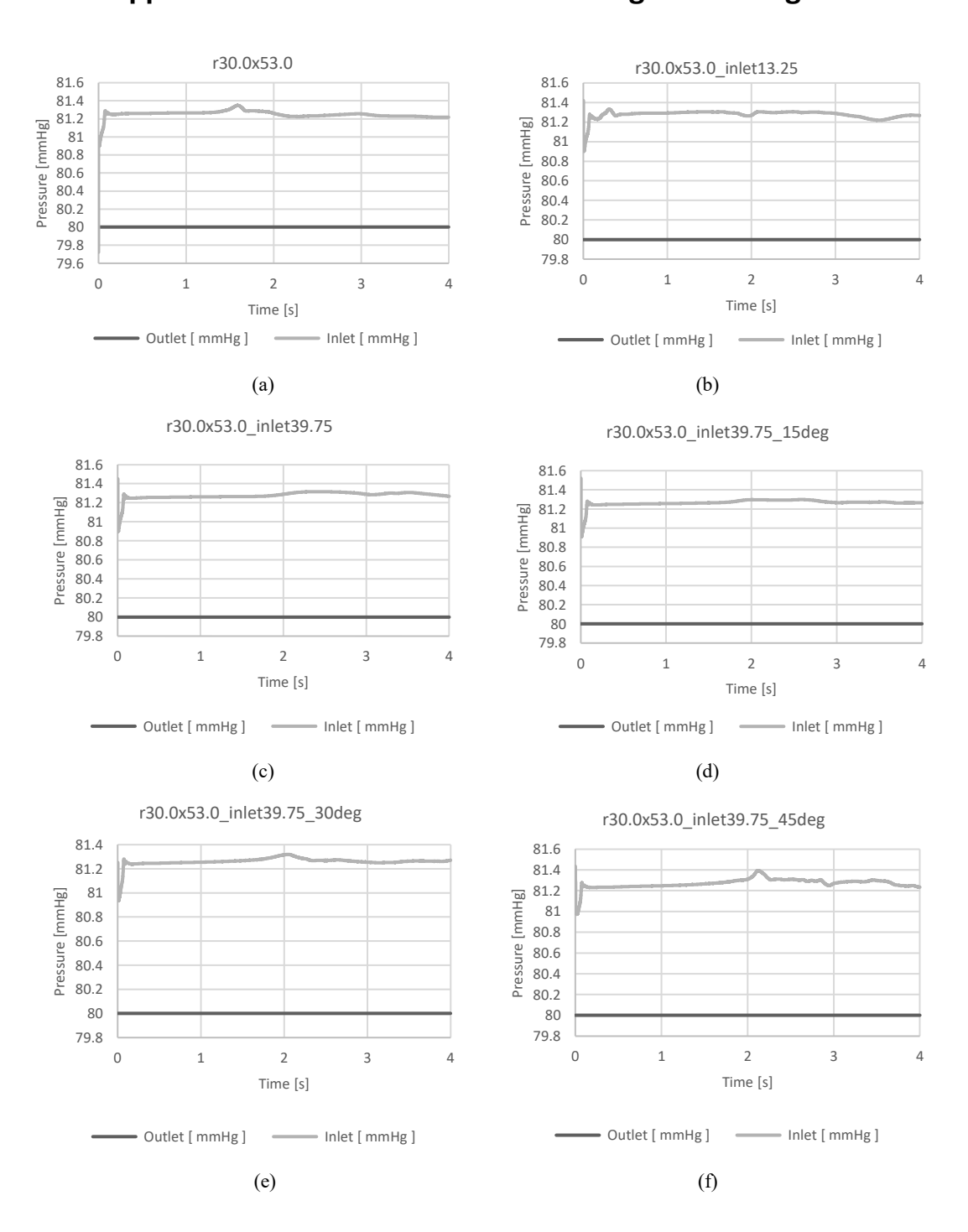


Figure 8.1 Plots of Pressure Area-weighted Average (a) r30.0x53.0 (b) r30.0x53.0_inlet13.25 (c) r30.0x53.0_inlet39.75 (d) r30.0x53.0_inlet39.75_15deg (e) r30.0x53.0_inlet39.75_30deg (f) r30.0x53.0_inlet39.75_45deg

8.3 Appendix C: Plots of Pressure Drop

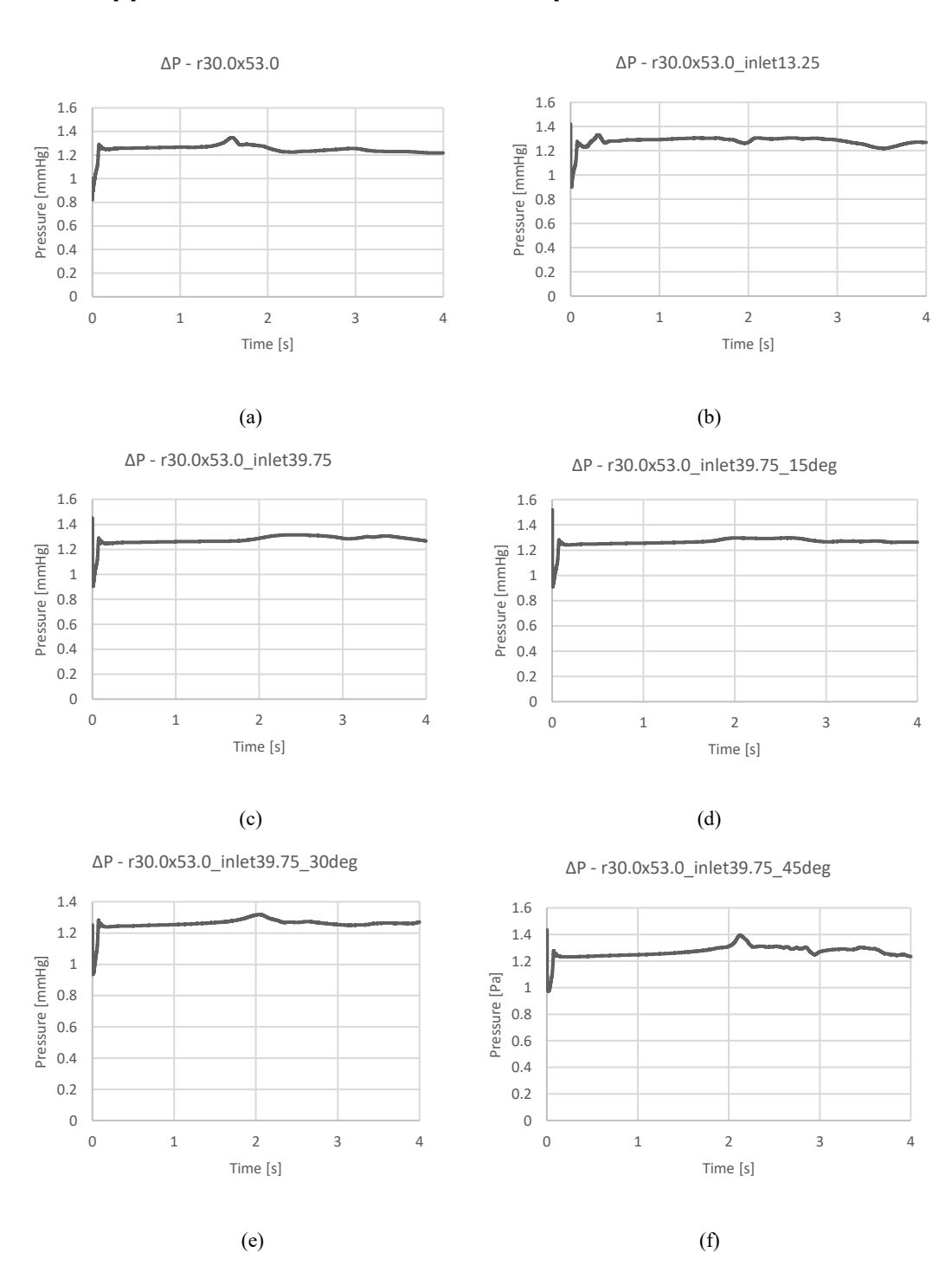


Figure 8.2 Plots of Pressure Drop Across Different Geometries (a) r30.0x53.0 (b) r30.0x53.0_inlet13.25 (c) r30.0x53.0_inlet39.75 (d) r30.0x53.0_inlet39.75_15deg (e) r30.0x53.0_inlet39.75_30deg (f) r30.0x53.0_inlet39.75 45deg

8.4 Appendix D: Velocity Magnitude Area-weighted Average Plots

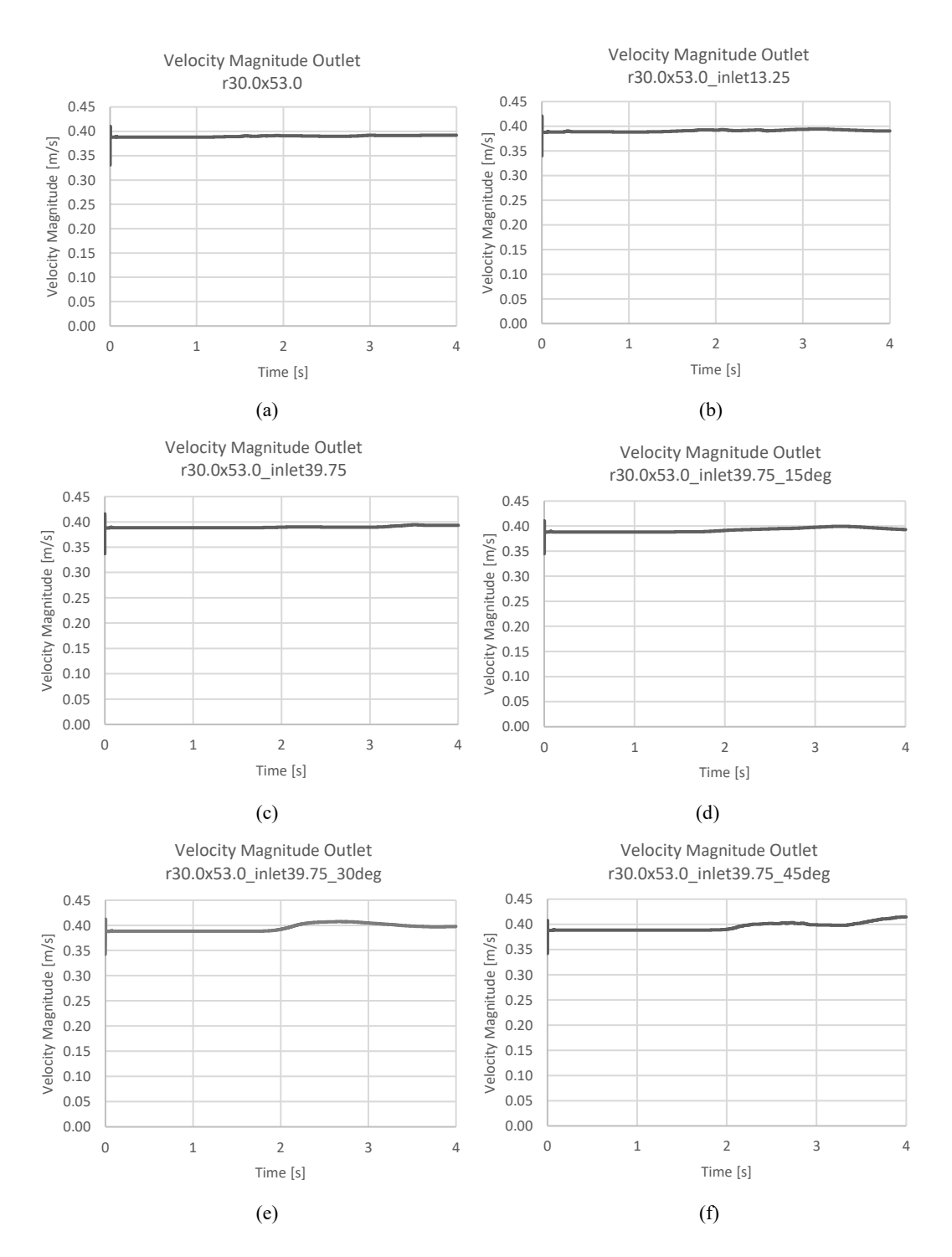


Figure 8.3 Velocity Magnitude Area-Weighted Average Plots (a) r30.0x53.0 (b) r30.0x53.0 inlet13.25 (c) r30.0x53.0 inlet39.75 (d) r30.0x53.0 inlet39.75 15deg (e) r30.0x53.0 inlet39.75 30deg (f) r30.0x53.0 inlet39.75 45deg

8.5 Appendix E: Bubble Size vs Number of Escaped Bubbles over Time

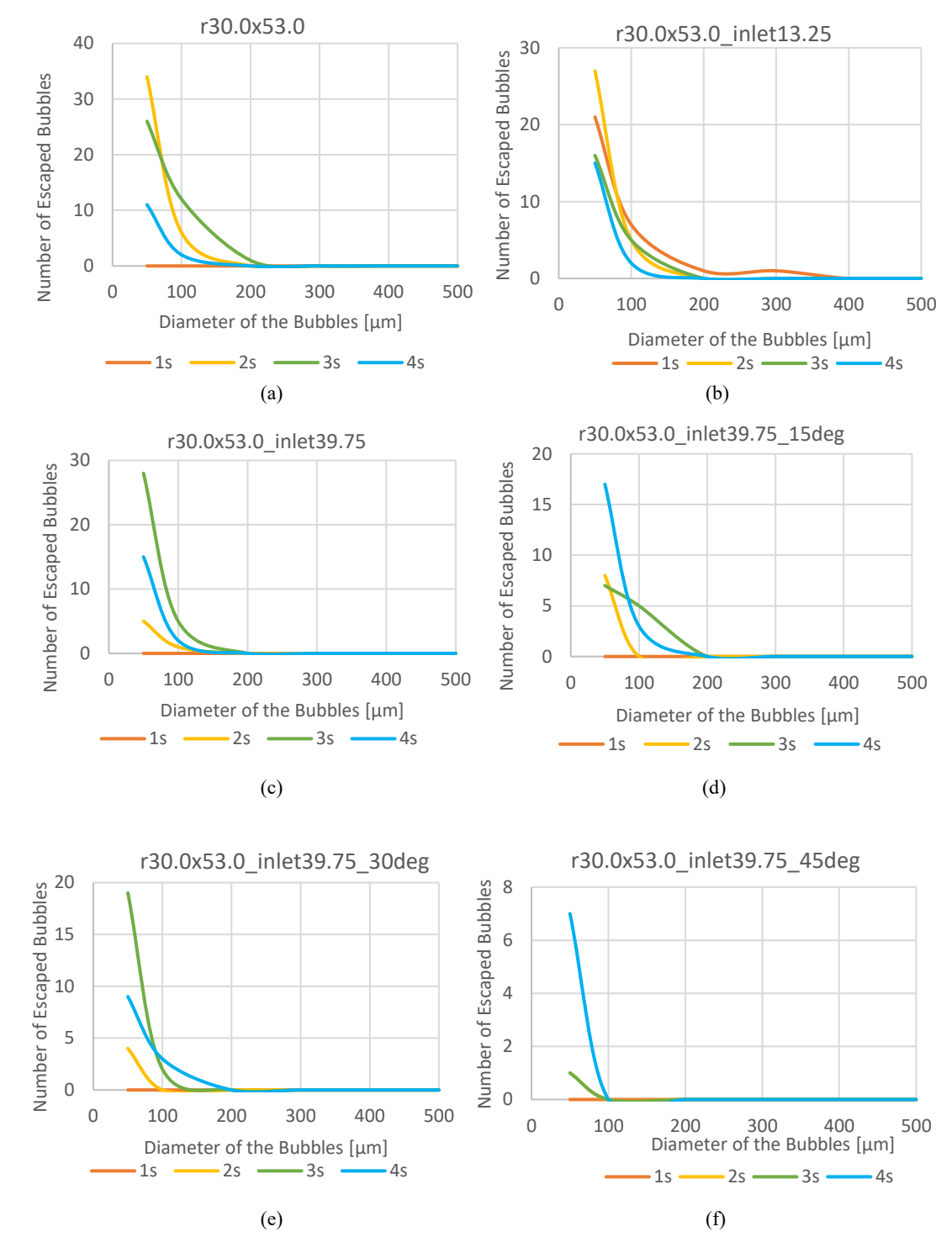


Figure 8.4 Correlation of Bubble' Size with the Number of Escaped Bubbles over Time (a) r30.0x53.0 (b) r30.0x53.0_inlet33.25 (c) r30.0x53.0_inlet39.75 (d) r30.0x53.0_inlet39.75_15deg (e) r30.0x53.0_inlet39.75_30deg (f) r30.0x53.0_inlet39.75_45deg